Universidad de Oviedo

PROGRAMA DE DOCTORADO

INGENIERÍA DE LOS RECURSOS NATURALES

Mejora de la fiabilidad estructural de las conexiones de los diques flotantes modulares: Un estudio exhaustivo sobre modelización numérica hidrodinámica, análisis de cargas extremas y evaluación de la fatiga

Alejandro J. Cebada Relea

Tesis Doctoral, 2024

Universidad de Oviedo

DOCTORATE PROGRAMME

NATURAL RESOURCES ENGINEERING

Enhancing structural reliability of modular floating breakwaters connections: A comprehensive study on hydrodynamic numerical modelling, extreme load analysis, and fatigue assessment.

Alejandro J. Cebada Relea

PhD Thesis, 2024

Para mis personas más importantes,
gracias por haber sido parte…

Universidad de Oviedo

RESUMEN DEL CONTENIDO DE TESIS DOCTORAL

1.- Título de la Tesis	
Español/Otro Idioma: Mejora de la fiabilidad estructural de las conexiones de los diques flotantes modulares: Un estudio exhaustivo sobre modelización numérica hidrodinámica, análisis de cargas extremas y evaluación de la fatiga	Inglés: Enhancing structural reliability of modular floating breakwaters connections: A comprehensive study on hydrodynamic numerical modelling, extreme load analysis, and fatigue assessment.

2.- Autor	
Nombre: Alejandro Jesús Cebada Relea	
Programa de Doctorado: Programa de Doctorado en Ingeniería de los Recursos Naturales	
Órgano responsable: Centro Internacional de Postgrado	

RESUMEN (en español)

Los diques flotantes modulares representan una solución alternativa para dar abrigo a las embarcaciones de un puerto, gracias a que son más económicas y generan un menor impacto ambiental que las tradicionales estructuras de protección que se asientan sobre el fondo marino. Sin embargo, su integridad estructural y la de las embarcaciones abrigadas puede verse comprometida si la estructura de protección no está adecuadamente diseñada, especialmente sus componentes más débiles: las conexiones entre módulos. En este sentido, los oleajes moderados y la exposición a cargas cíclicas durante la vida útil de la estructura generan dos modos de fallo principales; la rotura de la conexión debido a cargas extremas que agotan la sección útil de la conexión y la rotura de la conexión debido a la fatiga del material. Por tanto, se ha llevado a cabo una investigación exhaustiva para comprender y abordar estos desafíos.

Inicialmente se ha elaborado un modelo hidrodinámico de un conjunto de 5 pontones flotantes interconectados y fondeados al lecho marino. El modelo numérico ha sido calibrado a través de ensayos experimentales previos, permitiendo así una estimación precisa de las fuerzas que las conexiones han de soportar. Se ha demostrado que la rigidez de las conexiones juega un papel crucial en el comportamiento dinámico global de la estructura, especialmente en condiciones de oleaje oblicuo. Además, se ha demostrado que considerar oleajes irregulares es fundamental para una evaluación precisa del desempeño estructural, ya que la simulación de la estructura frente a oleajes regulares puede subestimar significativamente las fuerzas en las conexiones.

La determinación de las cargas extremas es fundamental para garantizar la supervivencia de la estructura en condiciones climáticas adversas. Para afrontar el cálculo de las fuerzas extremas inducidas por el oleaje en las conexiones se ha simulado la estructura frente a diversos oleajes oblicuos moderados. La combinación de métodos numéricos y estadísticos ha permitido estimar con precisión las fuerzas de diseño para estados de mar de 3 horas, proporcionando pautas para el dimensionamiento adecuado de las conexiones.

La fatiga de las conexiones representa un desafío crítico para la integridad estructural a largo plazo. Mediante simulaciones hidrodinámicas frente a oleajes operacionales, se ha analizado exhaustivamente las series temporales de tensiones axiales en cada conexión. Se ha desarrollado una metodología precisa para evaluar el daño por fatiga, considerando la dirección del oleaje y la ubicación de las conexiones en la estructura. Estos avances no solo mejoran la comprensión del comportamiento estructural, sino que también ofrecen pautas para mitigar el riesgo de daños por fatiga y garantizar la fiabilidad a largo plazo de los diques flotantes modulares.

En resumen, estos avances ingenieriles en materia de diques flotantes modulares han proporcionado una comprensión más profunda de los desafíos y soluciones en el diseño y operación de estas singulares estructuras. Esta tesis contribuye a mejorar la fiabilidad y el rendimiento de los diques flotantes en una variedad de condiciones marinas, allanando el camino hacia un desarrollo más sostenible de la infraestructura costera.

Universidad de Oviedo

RESUMEN (en inglés)

Floating modular breakwaters represent an alternative solution to shelter vessels in a port, as they are more cost-effective and have a lower environmental impact than traditional bottom-fixed structures. However, their structural integrity, as well as that of the sheltered vessels, may be compromised if the structure is not adequately designed, especially its weakest components: the connections between modules. On these grounds, moderate waves and exposure to cyclical loads during the structure life generate two main failure modes: connection failure due to extreme loads depleting the useful section of the connection, and connection failure due to material fatigue. Therefore, comprehensive research has been conducted to understand and address these challenges.

Initially, a hydrodynamic model of an array of 5 interconnected floating pontoons moored to the seabed was developed. The numerical model was calibrated through previous experimental tests, allowing for a precise estimation of the forces that connections must withstand. It has been demonstrated that the stiffness of the connections plays a crucial role in the overall dynamic behaviour of the structure, especially under oblique wave conditions. Furthermore, it has been shown that considering irregular waves is essential for an accurate assessment of structural performance, as simulation under regular waves can significantly underestimate the forces on the connections.

Determining extreme loads is essential to ensure the survival of the structure under adverse wave conditions. To address the calculation of wave-induced extreme forces on the connections, the structure was simulated against various moderate oblique waves. The combination of numerical and statistical methods has allowed for a precise estimation of design forces for 3-hour sea states, providing guidelines for the proper design of connections.

Connection fatigue poses a critical challenge to long-term structural integrity. Through hydrodynamic simulations under operational waves, the time series of axial stresses on each connection has been thoroughly analysed. A precise methodology has been developed to assess fatigue damage, considering wave direction and connection placement in the array. These advances not only enhance understanding of structural behaviour but also provide guidelines to mitigate the risk of fatigue damage and ensure the long-term reliability of floating modular breakwaters.

In summary, these engineering advances in floating modular breakwaters have provided a deeper understanding of the challenges and solutions in the design and operation of these singular structures. This thesis contributes to improving the reliability and performance of floating breakwaters in a variety of marine conditions, paving the way for more sustainable coastal infrastructure development.

SR. PRESIDENTE DE LA COMISIÓN ACADÉMICA DEL PROGRAMA DE DOCTORADO EN INGENIERÍA DE LOS RECURSOS NATURALES

ÍNDICE

Hoy vuelvo a estar aquí, delante de mi ordenador para escribir estas últimas líneas, terminando una de las etapas más importantes de mi vida. Si esto me lo hubiesen dicho hace años…probablemente no les hubiese creído. Y es que esto no ha sido precisamente un camino de rosas, pero gracias al grupo de personas que he tenido a mi alrededor el camino ha sido mucho más llano. Por eso, necesito daros las gracias.

Gracias a mis directores, a Mario y a Manolo. Gracias de todo corazón por todo el conocimiento que me habéis dado, todos los consejos que me habéis brindado y, por supuesto, por vuestra infinita paciencia. Sin duda, si no es por vuestra inestimable ayuda esta tesis no hubiese visto la luz.

Gracias a mis compañeros de batalla, a los portosboys, Fer y Claus, y a los minions, Luis y César. Gracias por todos los momentos vividos, las aventuras nacionales e internacionales, las discusiones reveladoras, los buenos y los malos momentos. Gracias por haber estado todo este tiempo aquí.

Gracias a mi familia, a mis padres, a mi hermana, a mi sobrino. Gracias por levantarme cuando he caído. Gracias por creer en mí. Sois una de mis mayores fuentes de inspiración y el espejo en el que quiero mirarme. Me siento increíblemente orgulloso de vosotros.

Pero, sobre todo, gracias a "ella", Zulema. Hoy estoy aquí sentado escribiendo esto gracias a ti. Eres mi apoyo más importante, el pilar maestro de mi vida y el motivo por el que me levanto cada mañana. Has sido, eres y serás la mujer de mi vida. Esta tesis lleva tu sello y el de nuestra pequeña compañera. Gracias por haberme hecho posible llegar aquí.

1. Introducción

1.1. Estado del Arte

1.1.1. Protección Costera y Obras de Abrigo

La actividad marítima constituye una de las piedras angulares en la historia y el desarrollo del ser humano. Ésta, abarca una amplia gama de actividades realizadas sobre cualquier masa de agua navegable, como lagos o ríos y especialmente importante en mares y océanos. Desde tiempos antiguos, las civilizaciones han dependido del mar para el comercio, la exploración, la pesca y la defensa, estableciendo una conexión vital entre las diferentes culturas y regiones geográficas.

Actualmente las actividades marítimas continúan desempeñando un papel crucial en la economía global, ya sea a través del transporte de mercancías por rutas marítimas estratégicas, como impulsor del turismo costero o proporcionando recursos naturales fundamentales como la pesca o los minerales. El transporte internacional de mercancías por vía marítima acapara el mayor volumen transportado en España (OTLE, 2023). Esto se debe a la capacidad que tiene este medio de transporte para mover grandes cantidades a largas distancias con un coste económico bajo, a pesar de no ser el medio de transporte más rápido.

Las operaciones en la línea de costa relacionadas con la actividad marítima no pueden realizarse en condiciones de seguridad si no se dispone de agua en relativa calma. En este sentido, se requiere de una infraestructura que facilite el embarque, desembarque, carga, descarga, almacenamiento y manipulación de mercancías y pasajeros entre los medios de transporte terrestre y marítimo. Estas funciones se llevan a cabo en los puertos que, además de proporcionar abrigo contra el oleaje, desempeñan un papel vital en el comercio internacional, el transporte de mercancías y la integración económica global. Esto los convierte en puntos clave para el desarrollo socioeconómico y la actividad marítima en las regiones costeras.

Los puertos históricos que se conservan hoy en día son testigos vivos del pasado marítimo y comercial de diversas regiones en el mundo. Lugares como el Puerto de Venecia en Italia; el Puerto de Ámsterdam en los Países Bajos, símbolo de la Edad de Oro neerlandesa; y el Puerto de Hamburgo en Alemania, uno de los más antiguos de Europa, son ejemplos notables (Figura 1). Estos puertos no solo representan la herencia marítima de sus respectivas ciudades, sino que también continúan desempeñando un papel relevante en la vida moderna.

La ubicación de la infraestructura portuaria es un aspecto de gran importancia. Idealmente, se prefiere que el emplazamiento sea sobre superficies naturalmente resguardadas y abrigadas de la acción directa del oleaje, como bahías o estuarios. Sin embargo, esto no siempre es posible y se requiere de la construcción de estructuras de defensa o diques, que ofrecen una barrera física artificial contra la acción del oleaje. Un ejemplo se encuentra en el puerto del Musel (Figura 2), emplazado al abrigo de los oleajes de componente noroeste por el Cabo de Peñas, pero que a su vez también se encuentra abrigado por un dique vertical.

1.1.2.Tipos de Diques

Los diques son estructuras de protección contra el oleaje. Estos representan una pieza fundamental dentro de la infraestructura portuaria, especialmente en aquellas zonas donde la protección natural es limitada o inexistente. Su función principal radica en mantener las aguas interiores del puerto en un estado de relativa calma, impidiendo que la fuerza del oleaje penetre en el área portuaria y mitigando su impacto. Al canalizar y disipar esta energía de manera controlada, los diques contribuyen significativamente a mantener un entorno seguro y operativo para la actividad marítima dentro del puerto (Goda, 2000).

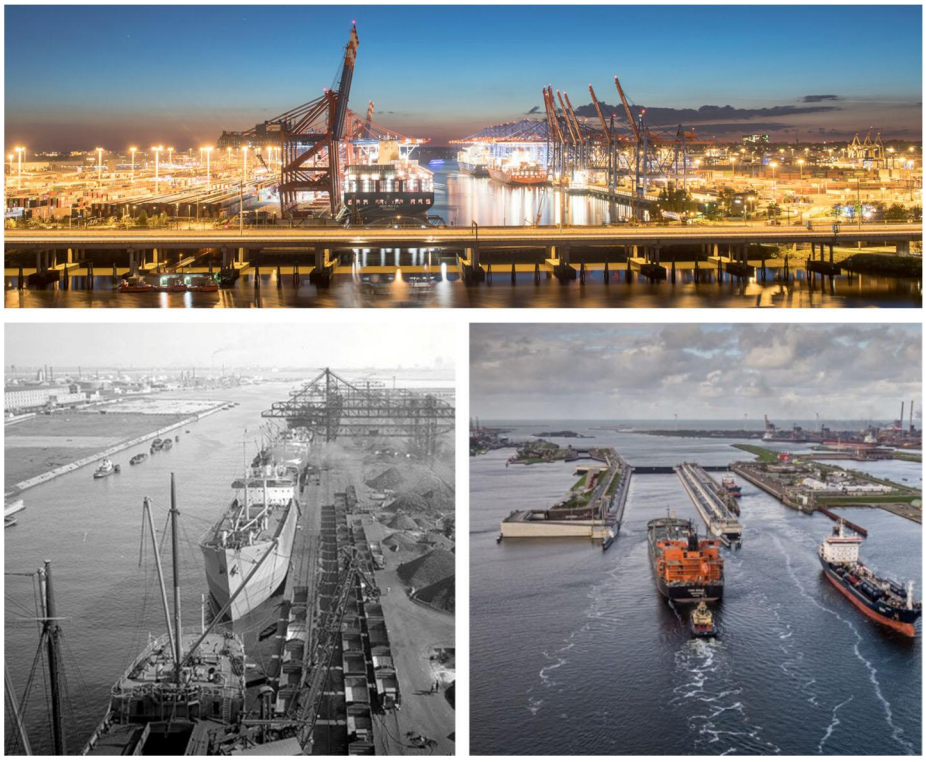

Figura 1. Puerto de Hamburgo (Hamburg Port Authority, accedido en 2.13.24) (panel superior), puerto de Venecia en el año 1917 (North Adriatic Sea Port Authority, accedido en 2.13.24) (panel inferior izquierdo) y puerto de Amsterdam (Port of Amsterdam, accedido en 2.13.24) (panel inferior derecho).

Existen múltiples diseños de diques y múltiples maneras de clasificarlos (Takahashi, 2002). La forma más genérica – y la que se ha realizado aquí –es diferenciar entre diques fijos y diques flotantes.

1.1.2.1 Diques fijos

Las estructuras de protección fijas son aquellas que tradicionalmente se han construido para proteger las aguas de un puerto. Estas se emplean para disipar o reflejar oleajes muy energéticos. Se trata pues de estructuras longitudinales de grandes dimensiones que se encuentran cimentadas sobre el lecho marino y se oponen al paso de las olas (Na'im et al., 2018). Las tipologías más comunes que se pueden encontrar dentro de los diques fijos se muestran en la Figura 3, a saber: los diques talud, los diques verticales, una tercera variante resultado de la combinación de las dos primeras (dique mixto = talud + vertical) y una cuarta tipología de dique vertical hundido. Dentro de esta cuarta tipología también se puede encontrar el talud hundido.

Figura 2. Fotografía panorámica del puerto del Musel (Gijón, Principado de Asturias). El dique vertical se situa arriba a la izquierda.

Los diques en talud son grandes acumulaciones de elementos sueltos, ya sean rocas o bloques de hormigón. Este tipo de estructura trabaja principalmente disipando la energía a través de la rotura del oleaje incidente (Puertos del Estado, 2009). Su construcción resulta muy atractiva en aguas poco profundas (con una profundidad inferior a 10 metros), sobre todo cuando los materiales necesarios para construir el dique están disponibles cerca del lugar de emplazamiento. Sin embargo, a medida que aumenta la profundidad, los costes de construcción aumentan considerablemente.

Los diques verticales se componen de una estructura monolítica, generalmente bloques, mampostería o cajones prefabricados, que actúan como una pantalla que refleja completamente el oleaje incidente. Son apropiados para aguas de profundidad media, entre 10 y 24 m (Takahashi, 2002), ya que resulta más económico utilizar este tipo de dique en lugar del talud. En contrapartida a la anterior tipología, en ésta se requiere que la capacidad portante del lecho marino sea adecuada y suficiente, de manera que asegure una base estable donde cimentar los bloques o mampuestos prefabricados, debido a que son elementos relativamente pesados. Esta tipología también se puede aplicar en su variante de pantalla hundida (última tipología mostrada en Figura 3) cuando solo se necesita atenuar el oleaje. Esto conlleva un ahorro económico al emplear menos material en la estructura monolítica y también reduce el impacto visual.

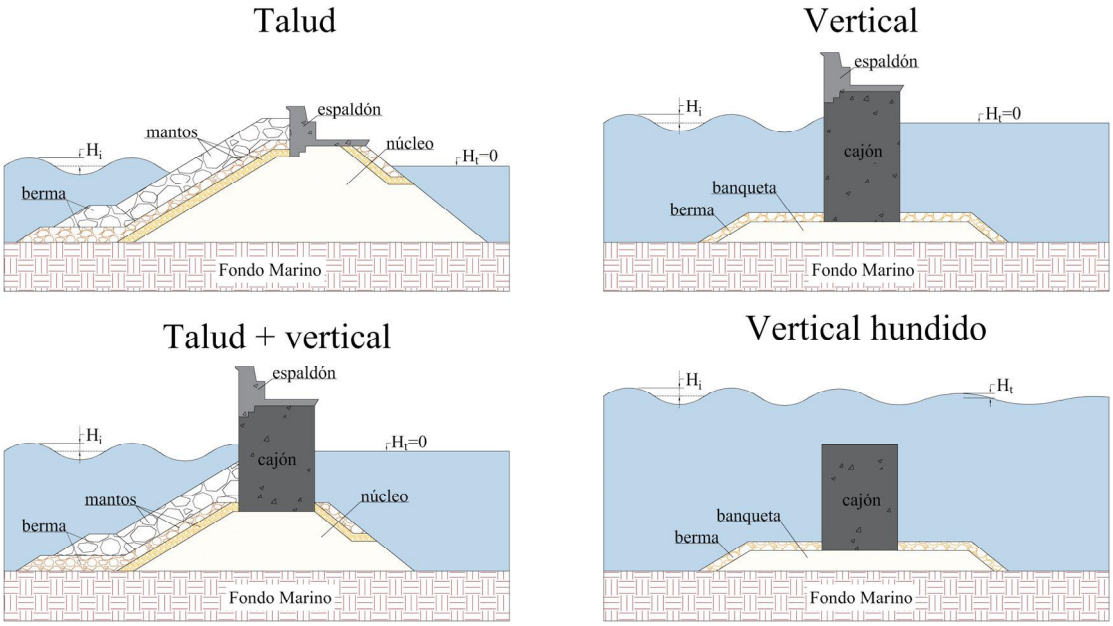

Figura 3: Tipos de diques fijos.

El tercer tipo resulta de una composición del dique vertical combinado con una berma inferior en talud. Este tipo de dique trabaja de igual forma que el dique vertical y es aplicable en aguas más profundas. Sin embargo, también requiere que las capacidades mecánicas del lecho sean adecuadas para la construcción de una base estable (Fousert, 2007).

1.1.2.2 Diques flotantes

Alternativamente a las estructuras de protección de configuración fija, existen otras maneras de conseguir que las aguas interiores del puerto se mantengan en relativa calma. Estas se engloban dentro de la categoría de diques flotantes y, habitualmente, su aplicabilidad está condicionada a las características medioambientales del emplazamiento. Este tipo de estructuras propone una solución de estructura modular flotante, amarrada al fondo marino, que trabaja reflejando o atenuando parcialmente el oleaje incidente. De esta forma, la altura de ola dentro de las aguas interiores del puerto (sotamar) es compatible con la actividad portuaria en condiciones de seguridad (Chakrabarti, 1994). En la mayoría de los casos, este tipo de diques resulta ineficiente debido a la alta resistencia estructural requerida por los elementos que conectan las estructuras modulares, o por las solicitaciones en el sistema de fondeo. Sin embargo, en aguas profundas o en zonas naturalmente abrigadas ofrecen una solución alternativa económicamente atractiva, además de reducir considerablemente el impacto medioambiental (Hales, 1981).

La Figura 4 muestra algunas de las tipologías más destacadas de diques flotantes (McCartney, 1985). Entre ellas se encuentran el cajón, el pontón, el marco en Y, la alfombra, las boyas atadas y la tipología de platos horizontales.

Los diques de tipo cajón, o en inglés *box*, son estructuras flotantes con una geometría rectangular o prismática. La configuración de cajón ofrece una gran estabilidad y resistencia frente a la acción del oleaje. Se construyen principalmente con módulos de hormigón armado y se conectan mediante conexiones flexibles postesadas para actuar como una unidad que trabaja como un todo uno. Las secciones transversales tienen longitudes máximas de 8 m de ancho, con calados no superiores a 1.5 m (Elchahal et al., 2009). La tipología cajón es una de las más eficientes para atenuar una gran variedad de condiciones de oleaje incidente (Dong et al., 2008). Por ello, existen numerosos ejemplos que han sido construidos en áreas costeras, incluso con condiciones de oleaje moderadas. Entre ellos se pueden encontrar el dique flotante de Holy Loch en Escocia o el más aún conocido cajón flotante del Muelle Hercule en Mónaco.

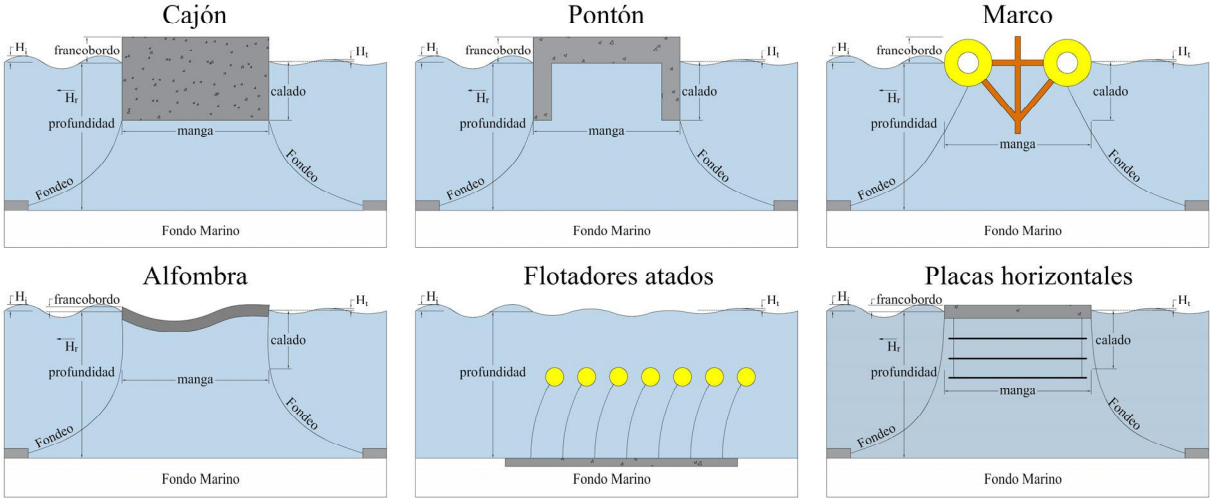

Figura 4. Tipos de diques flotantes.

Los pontones flotantes, inspirados en los populares diseños de barcos pontones, generalmente consisten en dos o más flotadores longitudinales que están rígidamente conectados a un tablero en la parte superior. Esta disposición aumenta la estabilidad y la inercia del sistema respecto a la tipología cajón − sin agregar peso adicional – mejorando la efectividad de reflejar oleaje moderado y ondas largas (Williams and Abul-Azm, 1997). Al igual que los diques flotantes tipo cajón, los pontones atenúan las olas principalmente por reflexión parcial (Ofuya, 1968). Además, el espacio entre los dos flotadores permite la disipación de la energía turbulenta. Algunos ejemplos de esta tipología se encuentran en la costa norte española, como por el ejemplo el pontón flotante de la bahía de Santoña (Cantabria), el pontón de San Juan de la Arena o el dique pontón flotante de Figueras (ambos en el Principado de Asturias), emplazado en la Ría del Eo (Figura 5).

Figura 5. Pontones flotantes en los puertos deportivos de Figueras (Principado de Asturias), Santoña (Cantabria) y San Juan de la Arena (Principado de Asturias). Paneles izquierda, centro y derecha respectivamente.

La tipología marco (Figura 4) combina pontones con estructuras de celosía para crear una barrera flotante que disipa la energía del oleaje tanto por reflexión como por turbulencia. Estas estructuras aprovechan la rigidez de los marcos para proporcionar protección contra las olas, de hecho, los diseños modernos recurren a pontones de hormigón o acero por su resistencia y durabilidad. Un ejemplo de esta tipología se encuentra operativa en el dique flotante construido en el Puerto de Brownsville Marina en Washington (Dai et al., 2018), que incorpora vallas de madera porosa instaladas en los lados de los pontones de hormigón para reducir la transmisión del oleaje hacia aguas interiores.

Los diques flotantes tipo alfombra son una solución innovadora que emplea materiales reciclados, como neumáticos usados, para mitigar la acción del oleaje. El concepto surgió en 1963 con el Wave-Maze de Stitt y Noble (Stitt and Nobel, 1963), que utilizaba neumáticos de camión flotando sobre la superficie del agua. Desde entonces, se han desarrollado numerosas configuraciones, como por ejemplo el diseño modular de Goodyear y el Wave-Guard (Candle, 1974). Estas estructuras disipan la energía del oleaje a través de la fricción y la perturbación de las partículas del agua. Una ventaja que ofrecen estos sistemas es que reducen la carga sobre los fondeos, ofreciendo una solución sostenible para la protección costera y portuaria. Sin embargo, estos diseños presentan deficiencias notables con oleaje de periodo largo, por lo que se requiere una investigación más profunda para mejorar su eficacia y reducir el espacio marino necesario.

Los atenuadores de tipo flotador atado (*tethered type*) son un subgrupo particular de los diques flotantes. El dispositivo de atenuación del oleaje comprende varios flotadores atados al lecho marino o a lastres de hormigón enterrado, que se mueven como péndulos invertidos bajo las olas. A diferencia de los otros tipos de diques discutidos anteriormente que, principalmente utilizan su inercia para disipar las olas por reflexión y/o fricción, los flotadores atados atenúan el oleaje

a través de la resistencia generada por el movimiento del flotador debido al gradiente de presión de las olas (Hales, 1981). Además de los flotadores esféricos, se pueden utilizar tanques cilíndricos apilados o neumáticos y también diferentes diseños modulares de lastre. Dado que las líneas de fondeo son componentes importantes en este sistema, se debe prestar especial atención al diseñarlas y tener en cuenta posibles cargas de impacto que puedan comprometer el sistema.

El último subgrupo de dique flotante presentado es el de placas horizontales. En esta tipología, la rigidez y el tamaño de la placa son dos factores clave que afectan al rendimiento de la estructura. Uno de los primeros diseños fue desarrollado por Dong et al. (2008), donde se propone un tablero rígido superior flotante con varias filas de redes de polietileno debajo. Con esta configuración, el tablero suprime el movimiento vertical de las partículas de la ola mientras que las redes horizontales perturban su órbita.

Alternativamente a estos diseños de estructura de protección flotante, en los últimos años han surgido nuevos conceptos que amplían su funcionalidad (ver Figura 6). La principal línea de investigación desarrollada en este ámbito se ha focalizado en encontrar las sinergias de estas estructuras con los dispositivos de conversión de la energía del oleaje (Zhang and Ning, 2019a; Zhao et al., 2019), aunque también se han desarrollado prototipos destinados a ejercer también como barrera artificial contra el viento (C. M. Wang et al., 2020) o destinados a uso de suelo urbano en alta mar (Wang et al., 2019). Otra potencial aplicación de estas estructuras en alta mar se puede encontrar en los primeros conceptos de aeropuertos flotantes (Zhang et al., 2020).

Figura 6. Nuevas aplicaciones de los diques flotantes. El panel izquierdo muestra un concepto de dique flotante parabólico con conversores de energía del oleaje (Zhang and Ning, 2019b) y el panel derecho un diseño conceptual de un aeropuerto flotante (Zhang et al., 2020).

1.1.2.3 Ventajas y desventajas

La aplicabilidad de cada tipo de dique depende de varios factores, principalmente de: la profundidad del agua, la disponibilidad de material cerca del lugar de emplazamiento y las condiciones locales del fondo marino. La limitación más importante a la hora de seleccionar una tipología u otra casi siempre se reduce al aspecto económico. La Figura 7 muestra cómo varían los costes de las diferentes tipologías comentadas respecto a la profundidad del agua. Un aspecto interesante que puede extraerse de esta figura es que los costes de construcción de los diques flotantes apenas varían con la profundidad, a diferencia de las estructuras de configuración fija en las que el coste económico se dispara exponencialmente a medida que la profundidad aumenta. Si además se tienen en cuenta otros aspectos como los costes de mantenimiento, las condiciones de oleaje o las condiciones medioambientales en el lugar de emplazamiento, las soluciones flotantes también pueden ofrecer una alternativa sostenible para profundidades más bajas.

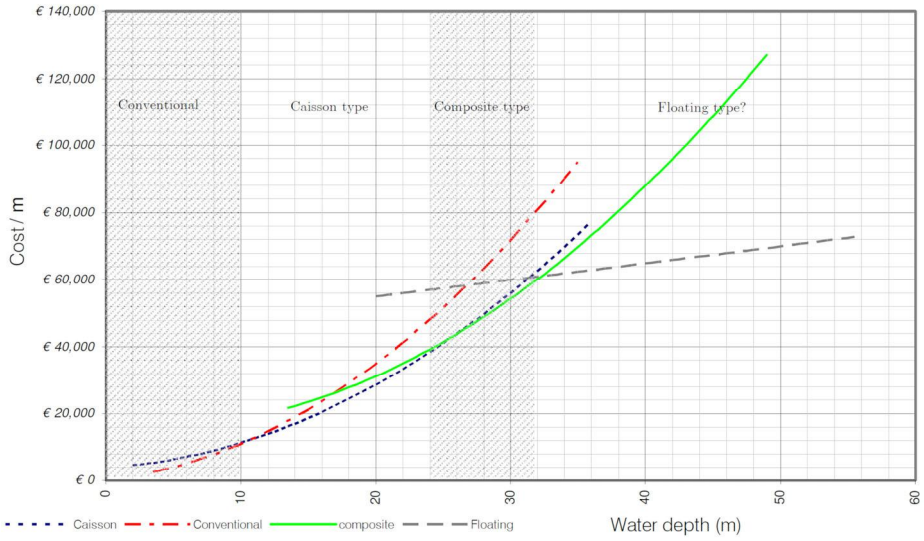

Figura 7. Coste de construcción por metro lineal de diferentes tipologías de diques frente a la profundidad (Fousert, 2007).

En resumen, las ventajas y desventajas que presenta un dique flotante en comparación con un dique o rompeolas de configuración fija se resumen brevemente a continuación (McCartney, 1985). Las ventajas asociadas son:

- Económico en profundidades mayores: resultan más atractivos en términos económicos en aguas profundas.
- Transportabilidad: permiten cambiar fácilmente la disposición de un puerto. Pueden ser reorganizados en nuevos diseños con poco esfuerzo, gracias a la modularización de la estructura.
- Solución en cimentaciones deficientes: pueden ser la única opción en lugares donde el fondo marino no soporte diques cimentados sobre él.
- Adaptabilidad a las mareas: son estructuras que apenas se ven afectadas por la variación del nivel del mar.
- Interferencia mínima con transporte de sedimentos y circulación de agua.
- Retirables y remolcables: se pueden retirar y remolcar fácilmente a áreas protegidas si se necesitan reparar.
- Apto para áreas de fondeo o amarre: son adecuados en lugares que requieren fondeo o amarre para embarcaciones.
- Estética: causan una intrusión mínima en el horizonte, especialmente en áreas con grandes variaciones de marea.
- Interferencia mínima con la circulación del agua y migración de peces.
- Polivalencia: facilitan el amarre, sirven como pasarela o área de estacionamiento (e.g. el cajón flotante del Muelle Hercule en Mónaco).

Por contrapartida, las desventajas son:

- Menor protección contra las olas: proporcionan menos protección en comparación con los diques fijos.
- Sensibilidad a la resonancia: son sensibles a frecuencias de onda cercanas a su frecuencia natural.
- Problemas dinámicos: la respuesta dinámica a las olas puede causar fatiga y fuerzas de amarre excesivas en los elementos de conexión y en los fondeos.

- Costes de mantenimiento moderados: los costes de mantenimiento pueden aumentar si la solicitación estructural es alta.

1.1.3. Tipos de Conexión entre Módulos Flotantes

En el diseño de diques flotantes usualmente se utiliza el coeficiente de transmisión como principal parámetro de diseño. Sin embargo, las conexiones entre módulos desempeñan un papel fundamental. Estos elementos son sin lugar a duda su talón de Aquiles y, si estos fallan, se produce una reacción en cadena en la que las embarcaciones son puestas en serio peligro (Richey and others, 1982). Por tanto, una tarea crucial es desarrollar soluciones de conexión duraderas y rentables para conectar los módulos flotantes. Los sistemas de conexión entre módulos adyacentes pueden diferenciarse básicamente en sistemas rígidos o flexibles (Wang and Nguyen, 2023). Éste es un aspecto diferenciador clave, ya que el comportamiento hidrodinámico de la estructura está influenciado por la rigidez de las conexiones (Ferreras et al., 2014; Loukogeorgaki et al., 2014).

Las conexiones rígidas se realizan comúnmente a través de pernos de unión, soldadura o utilizando conectores de esquina y laterales (Figura 8) (Wang and Wang, 2015). Siempre que la conexión trabaje adecuadamente, el movimiento relativo entre dos pontones queda completamente restringido en los 6 grados de libertad, por lo que no es posible que dos módulos adyacentes colisionen entre sí. La conexión rígida también elimina cualquier espacio entre módulos adyacentes, impidiendo así la transmisión del oleaje a través de ellos. No obstante, a medida que aumenta la longitud del dique flotante el momento de flexión también se incrementa considerablemente. Esto hace que la solicitación de las conexiones esté muy por encima de su resistencia nominal.

Las conexiones flexibles o semirrígidas consisten en una serie de tendones/cables de acero, cadenas, o pernos/tablestacas de goma que conectan los módulos (ver Figura 8). La conexión mediante cadenas prácticamente está en desuso y la conexión mediante pernos de goma no es adecuada para oleajes moderados. La conexión mediante cables de acero suele ser la solución más empleada por su mayor resistencia y facilidad de reemplazo. Generalmente, la conexión se compone por varios cables de acero trenzado que atraviesan un cilindro de neopreno. Los cables resisten los esfuerzos de tracción que induce el oleaje y se pretensan con el fin de mantener los módulos flotantes unidos rígidamente. Los neoprenos resisten las fuerzas de compresión y mantienen una separación fija entre los módulos, con el fin de evitar colisiones.

1.1.4. Interacción Estructura-Oleaje

Cuando una ola golpea a un dique flotante se desencadenan varios procesos, estos se representan gráficamente en la Figura 4, por ejemplo, en la tipología pontón. Inicialmente, la ola con altura H_i incide sobre el dique flotante con una cantidad de energía E_i. Una parte de esta energía se refleja como una ola de altura H_r y, otra parte se transmite hacia sotamar como una ola de altura H_t. El flujo debajo de la estructura flotante experimenta fricción en los contornos sumergidos de la estructura, por lo que parte de la energía incidente E_i se disipa y se convierte en turbulencia (Tsinker, 1995). La altura de la ola transmitida H_t se origina a partir tres fenómenos: la energía transmitida bajo el dique que no puede ser disipada por la estructura, el *run-up* o sobrepaso de parte de la ola por encima de la estructura y el oleaje radiado provocado por el movimiento de la estructura. Dependiendo del tipo de sistema de fondeo, el dique tiene cierta libertad de movimiento en los 6 grados de libertad. Por cada movimiento en cada grado de libertad, se genera una onda que se irradia lejos del mismo, conocida como onda radiada.

La respuesta hidrodinámica de una estructura flotante en condiciones reales de oleaje no puede determinarse de forma analítica. Para poder estimar cómo se comportará ésta frente a diferentes cargas ejercidas por el oleaje, generalmente se emplean dos formas de proceder: los ensayos físicos y la modelización numérica.

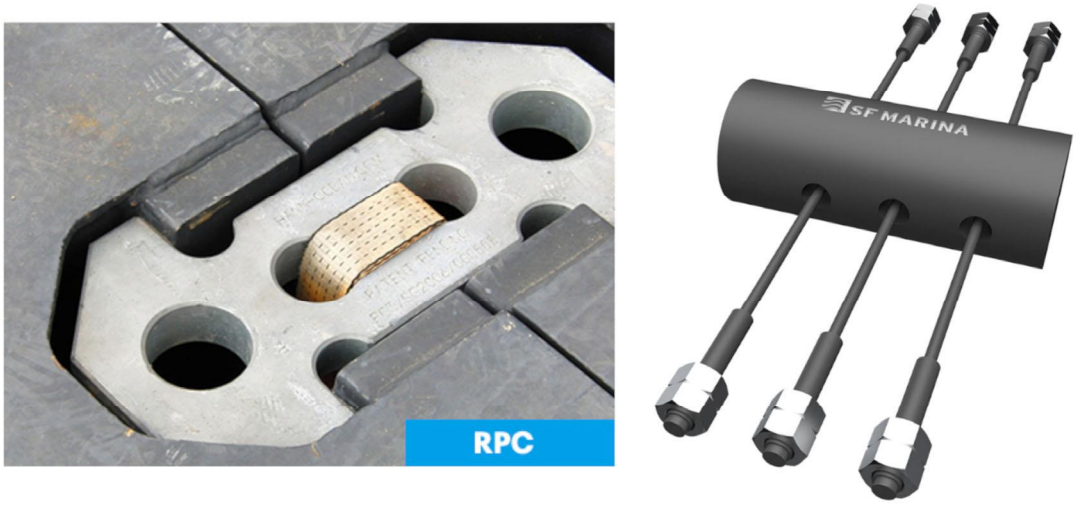

Figura 8. Sistema de conexión rígida en esquina desarrollado por la empresa Hann-Ocean (Hann-Ocean, accedido en 2.26.24) y sistema de conexión flexible desarrollado por SF-Marina (SF-Marina, accedido en 2.26.24).

Los ensayos físicos o tests experimentales de una estructura flotante, se llevan a cabo en tanques de olas o en canales hidrodinámicos. El experimento consiste en reproducir diferentes condiciones de oleaje o estados de mar sobre un modelo a escala de la estructura, en un entorno controlado. Sobre él se pueden adquirir medidas cuantitativas de la respuesta a través de sensores para capturar el movimiento del modelo a escala. También es posible conocer la altura de la ola en diferentes zonas del tanque mediante la colocación de sondas resistivas, o medir la deformación de cualquier componente a través de galgas extensométricas entre otros. Durante el desarrollo de esta tesis doctoral, el autor tuvo la oportunidad de colaborar en los test realizados sobre el dispositivo Heliosea (López et al., 2024) en el tanque de olas de la Faculdade de Engenharia da Universidade do Porto. Se trata de un dispositivo de panel solar fotovoltaico flotante (ver Figura 9) con un sistema de fondeo que trabaja continuamente a tracción (*Tension Leg Platform*). Más información sobre los ensayos realizados puede encontrarse en (Claus et al., 2024).

La experimentación en los tanques de olas es la forma más aproximada de estimar el comportamiento de una estructura flotante. Sin embargo, también es notablemente la más costosa. Por este motivo, los ensayos físicos solo se emplean para verificar, validar o calibrar estructuras previamente diseñadas a través de la modelización numérica.

Un modelo numérico es una herramienta matemática que permite representar un proceso físico real de forma aproximada. Dependiendo de la manga de la estructura y de la altura y la longitud de onda de la ola incidente, la estructura se modeliza hidrodinámicamente teniendo en cuenta unas fuerzas u otras (Chakrabarti, 1994). En la Figura 10 (panel izquierdo) se muestra un ábaco para considerar el régimen de fuerzas en el cálculo. En estructuras esbeltas, dónde la dimensión característica es mucho menor que la longitud de onda de la ola incidente, predominan las fuerzas inerciales y las fuerzas de arrastre. Las estructuras que cumplen este requisito pueden ser simplificadas y su cálculo se realiza a través de la teoría desarrollada por Morison et al. (1950). Sin embargo, cuando la dimensión de la manga es comparable o superior a la longitud de onda (como en el caso de un dique flotante), predominan las fuerzas de difracción.

Para acometer el cálculo teniendo en cuenta estas fuerzas, se emplea la teoría de difracción-radiación. Esta teoría se basa en la idea de que las ondas incidentes se difractan alrededor del cuerpo flotante generando un campo de presiones sobre su superficie, mientras que el propio cuerpo irradia o genera olas adicionales debido a su movimiento mientras flota.

Figura 9. Concepto de Heliosea (panel izquierdo) y ensayos físicos realizados sobre el modelo a escala 1:30 (Claus et al., 2024).

La oblicuidad del oleaje es un parámetro con gran influencia sobre las fuerzas en las conexiones de un dique flotante (Ferreras et al., 2014), por lo tanto, se requieren modelos numéricos en 3 dimensiones. Los principales métodos 3D que permiten estimar la respuesta de un dique flotante frente a la acción de oleaje son los métodos basados en la teoría del potencial como el BEM, *Boundary Element Method*) (Williams et al., 2000), los modelos CFD (*Computational Fluid Dynamics*) que aplican las ecuaciones de *Navier-Stokes* (Ji et al., 2018) o los modelos SPH (*Smooth Particle Hydrodynamics*), basados en métodos lagrangianos sin malla (Liu and Wang, 2020).

El método BEM una técnica numérica ampliamente utilizada en la modelización de problemas de flujo de fluidos en la ingeniería. Este método se basa en la representación de un problema en términos de la frontera del dominio, evitando la necesidad de discretizar todo el dominio (Aliabadi and Wen, 1984). Al discretizar únicamente los contornos y aplicar aproximaciones para las variables de interés, como el potencial de velocidad en el caso de la hidrodinámica, el BEM ofrece una alternativa eficiente a los métodos de volumen finito, diferencias finitas o elementos finitos. La esencia de este método radica en la formulación de las ecuaciones del problema en términos de integrales de fuerzas sobre el contorno de la estructura, lo que reduce significativamente el tamaño del problema y lo hace adecuado para grandes dominios de simulación y configuraciones complejas con múltiples estructuras flotantes interactuantes, líneas de fondeo y conexiones. Un ejemplo de este tipo de modelos ha sido publicado por el autor Cebada-Relea et al. (2022). En él, se simula la interacción de un dique flotante de tipo pontón con oleaje regular e irregular utilizando ANSYS Aqwa (ANSYS, 2016) (ver Figura 10).

1.1.5.Modos de Fallo de la Conexión

Una vez determinado el sistema de fuerzas actuante sobre la estructura, ya sea a través de ensayos físicos o modelización numérica (o una combinación de ambos), se procede a diseñar o verificar los componentes críticos de la estructura. En el caso de los diques flotantes modulares, las conexiones entre módulos representan los puntos críticos donde la estructura puede romperse inicialmente (Richey et al., 1982). Por consiguiente, el análisis de las fuerzas en los conectores de los módulos es de suma importancia para un diseño integrado y sostenible. En este sentido, se deben analizar dos modos de fallo mecánico fundamentales: la respuesta frente a oleajes extremos, y la respuesta frente a cargas cíclicas durante largos periodos de tiempo o, fatiga del material.

1.1.5.1 Análisis estadístico de fuerzas extremas

Una vez que se consiguen las series temporales de fuerzas inducidas por el oleaje en cada conexión del dique, comienza su análisis estadístico de valores extremos. El análisis del valor extremo de un estado de mar requiere una serie temporal lo suficientemente larga junto con una tasa de muestreo adecuada y, cuando se trata de modelos numéricos, se deben realizar múltiples repeticiones (DNV GL, 2017). La segunda publicación del autor Cebada-Relea et al. (2023) elabora una metodología para estimar la carga máxima inducida por el oleaje que pueden soportar las conexiones de un dique flotante. Para ello, se simulan diferentes estados de mar moderados y se analizan las series de fuerzas en las conexiones, utilizando diferentes criterios de selección de valores extremos y ajustando diferentes distribuciones de probabilidad.

El enfoque más simple es encontrar el valor máximo para cada simulación en el dominio del tiempo y seleccionar la carga de diseño a partir de valores estadísticos como la media, el máximo más probable (MPM, Most Probable Maximum) o un percentil dado. Sin embargo, este enfoque puede ser inviable para el diseño de un dique flotante por dos razones principales. En primer lugar, la duración del estado de mar debe ser de 20 min a 6 h para garantizar la estacionariedad del proceso, aunque se asume típicamente una duración de 3 h para procedimientos de diseño estandarizados (DNV GL, 2017). Si solo se considerara un pico de cada repetición, se necesitaría una gran cantidad de repeticiones para obtener estadísticas precisas. En segundo lugar, la repetición de simulaciones de 3 h requiere tiempos de ejecución demasiado largos, que aumentan considerablemente el coste computacional. En este sentido, se han propuesto algunos enfoques alternativos para analizar cargas extremas. Por ejemplo, Agarwal et al. (2015) utilizaron más de un pico por repetición para ajustar los valores a una distribución de probabilidad y estimar así eventos extremos. Una vez que se obtiene el histograma de picos de fuerza es necesario ajustar una función de distribución de probabilidad adecuada, como pueden ser Weibull, Rayleigh o Pareto entre otras, para modelar la ocurrencia de eventos extremos con precisión. Este ajuste permite calcular la probabilidad acumulada de superación de ciertos umbrales de carga y, por consiguiente, estimar la carga de diseño requerida en la conexión del dique flotante.

Este enfoque proporciona una metodología robusta para evaluar la capacidad de resistencia de las conexiones frente a condiciones de carga extremas, considerando una gama más amplia de datos y evitando las limitaciones asociadas con la selección de un único valor máximo por simulación. Además, al utilizar distribuciones de probabilidad para modelar los picos de fuerza, se puede obtener una estimación más precisa de la probabilidad de ocurrencia de eventos extremos, lo que resulta fundamental para el diseño seguro y eficiente de estructuras marítimas.

1.1.5.2 Daño por fatiga en las conexiones

La fatiga se define como un proceso de alteración estructural permanente, progresivo y localizado, que se produce en ciertos puntos de las estructuras sometidas a carga dinámicas. Este proceso conduce al fallo o agotamiento de la estructura, aunque las tensiones máximas alcanzadas sean inferiores al límite elástico del material. La caracterización a fatiga de un material puede hacerse a través de diferentes modelos de daño, las curvas S-N, las curvas ε-N o los modelos de crecimiento de grieta. Las curvas S-N (Wöhler, 1870), desarrolladas por el ingeniero alemán August Whöler, son las más ampliamente utilizadas y éstas relacionan los rangos de tensión con el número de ciclos a los que la estructura, o sus elementos, están expuestos. El método habitual para obtenerlas implica aplicar una carga senoidal controlada sobre una probeta hasta que se produce su rotura. Para evaluar la dispersión en el daño por fatiga se realizan ensayos a diferentes niveles de tensión, para caracterizar completamente las curvas S-N, con múltiples pruebas para cada nivel (DNVGL-OS-E301, 2018).

El análisis de fatiga es crucial en la evaluación de la integridad estructural de cualquier sistema sujeto a cargas dinámicas a lo largo del tiempo. Tradicionalmente, para cargas de amplitud variable como las generadas por el oleaje, se emplea el algoritmo de conteo de ciclos Rainflow (Matsuichi and Endo, 1968), combinado con modelos de daño como la regla de Palmgren-Miner (Miner, 2021; Palmgren, 1924). Sin embargo, este enfoque, aunque útil, puede resultar computacionalmente costoso a medida que aumenta la longitud de la serie temporal y puede sobreestimar la capacidad del material ya que simplifica en exceso su comportamiento (Muñiz-Calvente et al., 2022).

Para abordar estas limitaciones, han surgido enfoques alternativos basados en el dominio de la frecuencia. En contraste con el análisis en el dominio del tiempo, estos métodos descomponen la respuesta de tensión en sus componentes espectrales, lo que ofrece una comprensión más detallada de su comportamiento dinámico. Dependiendo de la naturaleza del proceso, se han desarrollado varios métodos espectrales de fatiga (Zorman et al., 2023). Este enfoque, además de ser más rápido, puede utilizarse para identificar frecuencias resonantes y modos de vibración, que pueden conducir a la rotura de la conexión del dique flotante por fatiga (Larsen and Irvine, 2015).

Existen varios ejemplos de estudios que profundizan en el análisis de fatiga de estructuras flotantes. Algunos se centran en el daño por fatiga soportado por uniones soldadas estructurales (Mourão et al., 2020). Otros estudios tratan sobre el daño por fatiga en las líneas de fondeo (Xu and Soares, 2021). Sus hallazgos subrayan la eficacia de los métodos espectrales en la predicción del daño por fatiga. La tercera publicación del autor (Cebada-Relea et al., 2024) trata sobre el análisis a fatiga de las conexiones del pontón flotante mostrado en la Figura 10. En ella se detalla el proceso de análisis de fatiga utilizando diferentes enfoques y se propone una metodología de cálculo para reducir el coste computacional del proceso de cálculo de daño de por fatiga.

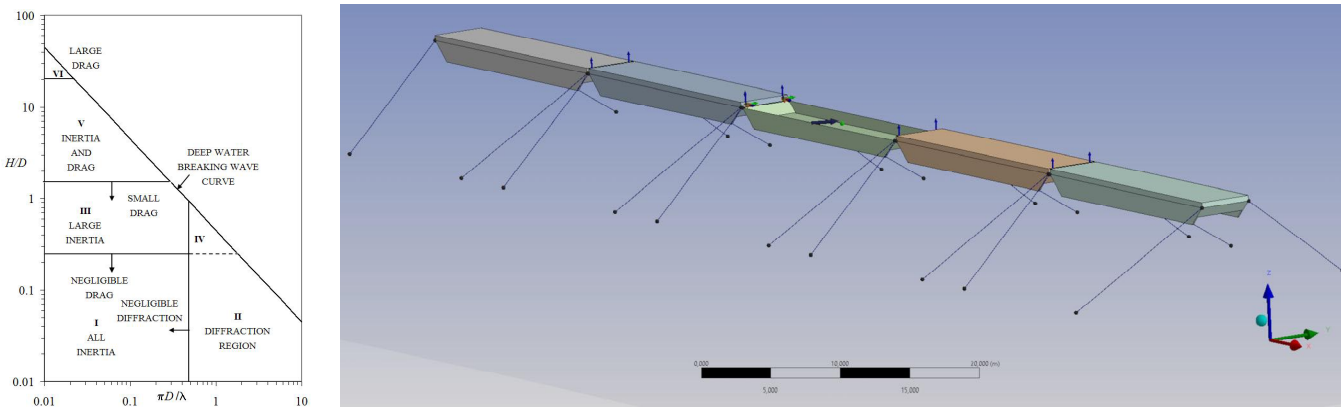

Figura 10. Régimen de fuerzas a considerar en la modelización hidrodinámica (Chakrabarti, 1994), *H* y *λ* son la altura y longitud de onda respectivamente y *D* es la dimensión característica (panel izquierdo). Modelo BEM de dique flotante pontón elaborado en Aqwa v2021R1 (panel derecho).

1.2. Motivación y Objetivos

A pesar de que los diques flotantes son estructuras que generalmente operan de forma satisfactoria, a lo largo de la historia se han sucedido múltiples casos de fallos estructurales en los que se ha detectado un patrón común: las conexiones son el elemento que falla primero. Esta tesis doctoral surge de la profunda reflexión sobre la problemática inherente al comportamiento de las conexiones inter-modulares, así como su capacidad para hacer frente a condiciones adversas y su durabilidad.

Un ejemplo de esto se ha podido observar en el pontón flotante de Figueras, emplazado en la ría del Eo (Principado de Asturias, España). Esta estructura ha sufrido repetidos colapsos debido a las condiciones climáticas adversas y al daño por fatiga que reciben sus conexiones a lo largo del tiempo, poniendo en riesgo a las embarcaciones a las que da abrigo. El resultado de un mal dimensionamiento de la conexión produce la rotura de los cables de acero trenzados que mantienen a los módulos unidos, como se aprecia en la Figura 11.

Este hecho observado, unido a la falta de bibliografía consistente en el dimensionamiento de los elementos de conexión en estructuras flotantes, han motivado el establecimiento de una metodología de diseño eficiente. Este enfoque busca aplicarse no solo a diques flotantes, sino también a otras estructuras marinas modulares.

Figura 11. Dique flotante de Figueras (panel izquierdo), detalle de conexión funcionando correctamente (panel superior derecho) y detalle de rotura tras temporal (panel inferior derecho).

Por lo tanto, el objetivo principal de esta tesis doctoral consiste en desarrollar buenas prácticas que aborden una mejora en el diseño eficiente, duradero y sostenible de las conexiones de un dique flotante, y que también puedan ser extrapolables a otras estructuras modulares flotantes. Los objetivos secundarios derivados del estudio son:

- Utilizar herramientas numéricas de cálculo en 3D para modelar la interacción oleaje-estructura y estimar la carga inducida en las conexiones.
- Validar el comportamiento de la estructura flotante a través de la calibración del modelo numérico con ensayos experimentales previos, con objeto de estimar las fuerzas inducidas de forma precisa.

- Analizar de manera exhaustiva cómo afectan los parámetros del estado de mar, tales como la duración, la altura significante, el periodo de pico y el ángulo de incidencia, a las fuerzas inducidas en las conexiones.
- Investigar una metodología para estimar las cargas extremas en las conexiones. Explorar la aplicabilidad de diferentes enfoques que permitan determinar la fuerza de diseño en cada conexión.
- Investigar el daño por fatiga de las conexiones del dique flotante bajo diferentes condiciones de oleaje, utilizando y comparando distintos enfoques.
- Explorar la viabilidad y el rendimiento de metodologías alternativas para reducir el número de simulaciones necesarias y optimizar los recursos computacionales.

1.3. Estructura del documento

La presente tesis doctoral se ha estructurado siguiendo el orden descrito a continuación. En primer lugar, se ha procedido a realizar una introducción a la temática abordada. En este primer capítulo se explican cuestiones como la necesidad de las obras de protección contra el oleaje, las tipologías más comunes de diques fijos y flotantes. También se han descrito los tipos de conexión entre diques flotantes, así como una breve explicación de la interacción de la ola con el dique pontón, las formas de estimar la respuesta hidrodinámica de la estructura y sus conexiones y los modos de fallo que se han investigado. Finalmente se describe la motivación y los objetivos de esta tesis doctoral.

El segundo capítulo (2. Modelización numérica en el dominio del tiempo de las fuerzas de conexión en un pontón modular flotante bajo oleaje oblicuo regular e irregular muestra la primera publicación científica, en la que se aborda el proceso de modelización y calibración del modelo numérico hidrodinámico del dique flotante. Adicionalmente también se examina la respuesta de la estructura frente a oleajes regulares e irregulares.

En el capítulo 3. Análisis a corto plazo de las fuerzas inducidas por el oleaje en las conexiones de un dique flotante presenta la segunda publicación llevada a cabo. En ella se detalla el proceso de cálculo para la obtención de la fuerza axial máxima inducida por el oleaje.

En el cuarto capítulo 4. Evaluación del riesgo de daños por fatiga en las conexiones de los pontones flotantes se muestra la tercera publicación realizada. En ella se aborda el cálculo del daño por fatiga que soportan las conexiones y además se propone una metodología más eficiente utilizando las funciones de transferencia de tensión. Cada uno de los artículos científicos contiene un breve resumen, una descripción de la contribución del autor a la publicación y un informe del factor de impacto de la revista científica. Asimismo, cada publicación también contiene sus propias referencias.

La discusión de las publicaciones se lleva a cabo en el capítulo 5. Discusión general y las conclusiones alcanzadas en la tesis doctoral se detallan en el capítulo 6. Conclusiones. Finalmente, las referencias correspondientes a la introducción y la discusión general se encuentran en el capítulo 7. Referencias.

2. MODELIZACIÓN NUMÉRICA EN EL DOMINIO DEL TIEMPO DE LAS FUERZAS DE CONEXIÓN EN UN PONTÓN MODULAR FLOTANTE BAJO OLEAJE OBLICUO REGULAR E IRREGULAR

2.1. Resumen

La primera publicación científica se titula *Time-domain numerical modelling of the connector forces in a modular pontoon floating breakwater under regular and irregular oblique waves*. El estudio se realizó sobre un conjunto de cinco pontones interconectados y fondeados al lecho marino a través de fondeos elásticos, sometido a cargas de oleaje oblicuo regular e irregular. Se adopta modelo numérico basado en el método BEM. Después, se calcula la respuesta en el dominio del tiempo del dique flotante, entre las que se incluyen las fuerzas no lineales que ejercen los fondeos y las conexiones entre módulos. La respuesta de la estructura bajo oleaje regular se compara con los resultados de ensayos experimentales previos. Para calibrar el modelo se utilizaron los parámetros de rigidez en la conexión y el coeficiente de arrastre en las aletas del pontón. Finalmente, se compara la respuesta frente a condiciones de oleaje regular e irregular. Los resultados revelan que la rigidez controla el comportamiento de la estructura y que la simulación de oleaje regular subestima las fuerzas en la conexión.

2.2. Contribución

La contribución del autor a esta publicación ha sido notable. Ha trabajado en diferentes ámbitos como la conceptualización del problema, así como la elaboración del modelo numérico y el análisis de resultados. También ha participado en la escritura del borrador inicial, así como en las tareas de edición, visualización y revisión.

2.3. Informe de factor de impacto

A.J. Cebada-Relea, M. López, M. Aenlle. "*Time-domain numerical modelling of the connector forces in a modular pontoon floating breakwater under regular and irregular oblique waves*". Ocean Engineering 243 (2022): Elsevier ISSN: 0029-8018. DOI: 10.1016/j.oceaneng.2021.110263.

Tipo de producción: Artículo científico
Posición de firma: 1

Nº total de autores: 3
Fuente de impacto: WOS (JCR)
Índice de impacto: 3.795

Tipo de soporte: Revista
Grado de contribución: Autor/a o coautor/a de artículo en revista con comité evaluador de admisión externo
Autor de correspondencia: No
Categoría: *Journal*
Revista dentro del 25%: Si

Ocean Engineering 243 (2022) 110263

Contents lists available at ScienceDirect

Ocean Engineering

journal homepage: www.elsevier.com/locate/oceaneng

Time-domain numerical modelling of the connector forces in a modular pontoon floating breakwater under regular and irregular oblique waves

A.J. Cebada-Relea, M. López *, M. Aenlle

DyMAST Research Group and Department of Construction and Manufacturing Engineering, University of Oviedo, Polytechnic School of Mieres, C/ Gonzalo Gutiérrez Quirós s/n 33600, Mieres, Asturias, Spain

ARTICLE INFO

Keywords:
Floating structures
Fluid-structure interaction
Model validation
Potential flow theory
Aqwa

ABSTRACT

Floating breakwaters are an interesting alternative to bottom-fixed structures due to their lower cost and environmental impact. Nonetheless, structural failures in the module connections are frequent. Accurate analysis of the hydrodynamic response is therefore crucial to their structural design. This article reports on numerical modelling of the forces on the module connectors in a modular pontoon breakwater. The study case was an array of five pontoons with elastic mooring lines under regular and irregular oblique waves. A 3D Boundary Element Method (BEM) solver was applied to find the velocity potentials and to characterize the frequency-domain response. The time-domain response of the floating breakwater is calculated along with the forces in the elastic mooring lines and module joints. Nonlinear hydrodynamic effects were reproduced by calculating the Froude-Krylov and hydrostatic forces over the instantaneous wetted surface at each time step. The response of the modular array under regular waves was then compared with previous experiments. After calibrating connector stiffness, the numerical and experimental results were in good agreement. Finally, the floating structure's response to regular and irregular waves was compared. The results revealed that simulation of only regular waves underestimates maximum connection forces by one order of magnitude.

1. Introduction

Breakwaters attenuate waves in harbour areas providing safe harbourage and minimizing port operation downtimes Lopez et al., 2015. The foundations of these massive constructions are commonly laid on the seabed at the expense of high environmental impact. Alternatively, several typologies of floating breakwaters have been proposed as a low-cost and environmentally-friendly solution (McCartney, 1985). Among the different configurations of floating breakwaters, the most common types are the box, pontoon, Y-frame, mat, tethered and horizontal plates (Fig. 1). This study focused on pontoon floating breakwaters, which consist of several concrete modules moored to the seabed and connected to each other by flexible connectors.

An example of this typology is the modular floating breakwater in the Port of Figueras in the Eo River estuary in northern Spain (Fig. 2). The local port authorities have reported frequent structural failures in this breakwater after extreme wind waves, starting with the module connectors breaking. This causes the unrestrained modules to undergo very strong relative movement, resulting in collisions between adjacent modules and reduction in the wave dissipation efficiency of the breakwater. It may be inferred from this observation that the pontoon design installed at the Port of Figueras is unable to withstand the local wave conditions due to excessive module connector forces (Cebada and López, 2020).

Similar structural damage, in which the connections appear to be the Achille's heel in their design, has been reported in other floating breakwaters worldwide (Martinelli et al., 2008). Analysis of the module connector forces is therefore of paramount importance for an integrated and sustainable design. The floating breakwater response and internal forces in the connectors can be studied with physical and/or numerical models.

The hydrodynamic response of these structures, and particularly, their wave transmission coefficients (e.g. Cheng et al., 2020; Dong et al., 2008; Ruol et al., 2013), are commonly tested with physical models in wave tanks. However, research on the structural response of floating breakwaters is scarce. Apart from wave transmission, Martinelli et al. (2008) studied the loads in moorings and connectors of different floating breakwater layouts. Peña et al. (2011) carried out physical model tests on a pontoon similar to that of the Port of Figueras under regular waves, and analysed the mechanical loads on the mooring lines and the module

* Corresponding author.
E-mail address: mario.lopez@uniovi.es (M. López).

https://doi.org/10.1016/j.oceaneng.2021.110263
Received 23 July 2021; Received in revised form 22 October 2021; Accepted 26 November 2021
Available online 18 December 2021

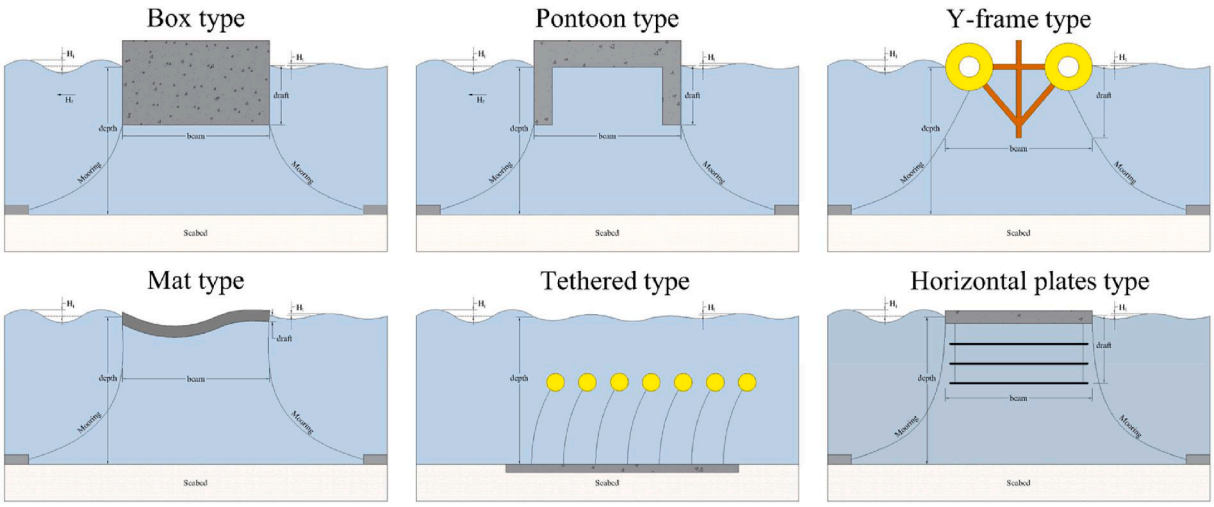

Fig. 1. Main types of floating breakwaters.

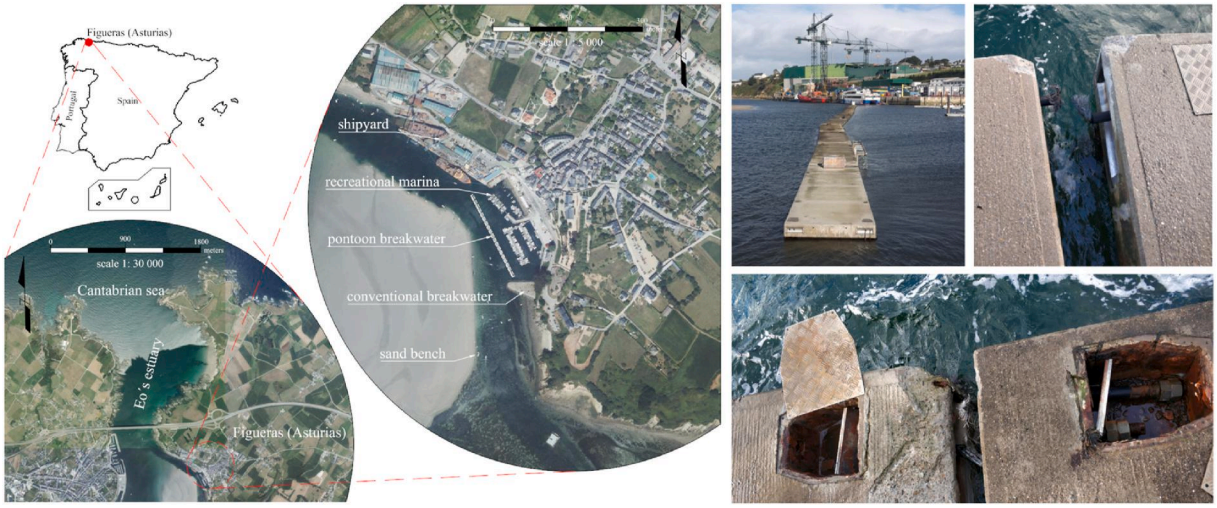

Fig. 2. Floating breakwater at the Port of Figueras (Spain): location (left) and pictures of the structure after connector breakage (right).

connectors. Ferreras et al. (2014) also studied the effect of the mooring typology and the module layout on the structural behaviour of modular pontoons under regular waves, and applied the results to the design of a breakwater similar to the one at the Port of Figueras. More recently, image processing algorithms have been applied to study the hydroelastic and structural responses of a modular pontoon under the action of perpendicular and oblique regular waves (Loukogeorgaki et al., 2017). The structural response of other types of floating breakwater, such as the box subtype, have also been studied experimentally (Loukogeorgaki et al., 2014).

Several different approaches to numerical modelling analysis have been applied to wave-structure interaction of floating breakwaters during the last few decades. 2D modelling is the most widely used methodology, but it cannot reproduce the wave obliquity responsible for severe loads on module connections (Martinelli et al., 2008). Traditional 2D linear methods include the finite element method (FEM) (Elchahal et al., 2009; Sannasiraj et al., 2001), the element-free Galerkin method (Lee and Cho, 2003), and the boundary element method (BEM) (Williams et al., 2000). Other novel techniques applied to pontoon-type floating breakwaters are the Navier-Stokes solvers, which include two well-differentiated groups: the finite volume method, based on structured Eulerian meshes, and the volume of fluid technique for tracking the liquid-gas interface (Ji et al., 2018), and smoothed-particle hydrodynamics based on Lagrangian mesh-free methods (Liu and Wang, 2020). Both solvers include nonlinear hydrodynamic effects in the wave-structure interaction solution, but at a high computational cost.

3D models based on potential flow theory have therefore been proposed to evaluate complex layouts with mooring lines and connection elements. Abul-Azm and Gesraha (2000) studied the hydrodynamic properties of a long rigid pontoon floating in oblique waves with only three rigid-body degrees of freedom (DoF) in the frequency domain. 3D hydrodynamic linear models have been used to assess the performance of hinged floating breakwaters under the action of normal regular waves (Loukogeorgaki and Angelides, 2005), as well as for several different wave headings (e.g. Diamantoulaki and Angelides, 2010; Teng et al., 2014). Cable-moored hinged floating breakwaters were analysed by coupling the hydrodynamic formulation of the floating body with static and dynamic analysis of the mooring lines (Diamantoulaki and Angelides, 2011). This approach was applied to the performance of a pontoon-type floating structure under the effects of regular waves with particular focus on mooring line tension and the hydroelastic structural response (Loukogeorgaki et al., 2015). A similar approach was applied to solve the forces on the connectors in an array of box-type floating breakwaters under irregular waves (Ćatipović et al., 2019).

In addition to these frequency-domain models, time-domain solvers

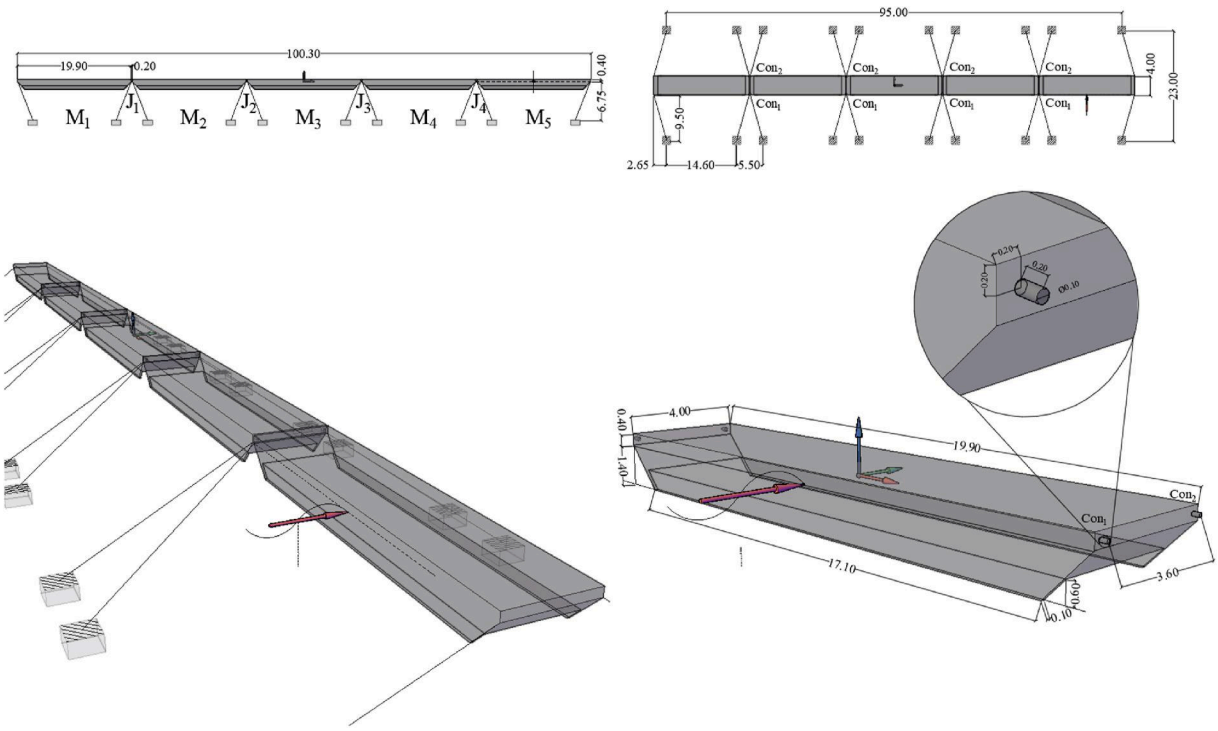

Fig. 3. Main floating breakwater elements and dimensions (in [m]). *M* denotes the module number, *J* is the joint number and *Con* is the connection number. Based on Peña et al. (2011).

Table 1
Geometrical and mechanical properties of the modular pontoon.

Property	Axis	Value
Length (m)	*X*	19.90
Beam (m)	*Y*	4.00
Height (m)	*Z*	1.80
Draft (m)	Z	0.40
Depth (m)	*Z*	6.75
Displacement (t)	–	40.00
Centre of gravity (m)	*X*	0
	Y	0
	Z	−0.21
Centre of buoyancy (m)	*X*	0
	Y	0
	Z	−0.42
Inertia (t·m^2)	*X*	60.94
	Y	1253.82
	Z	1303.98
Radius of gyration (m)	*X*	1.23
	Y	5.60
	Z	5.70

based on potential flow theory have also been applied. Chen et al. (2012) applied a 2-D model to analyse the transmission coefficient, motion response, and mooring forces of a pontoon-plate floating breakwater under regular waves. Later, the 3D motion response performance of a single moored pontoon and the forces in the mooring system were analysed under regular waves with different wave headings Chen et al., 2017. Nonetheless, there are no time-domain simulations of floating pontoon arrays under more realistic wave conditions in the literature.

This study dealt with 3D numerical modelling in the time domain of a modular pontoon breakwater studied experimentally by Peña et al. (2011). The objective was to accurately estimate the forces in the connectors, a critical element in the design of these structures. The forces in the elastic mooring lines and the module connectors were considered along with the instantaneous Froude-Krylov and hydrostatic forces beneath the incident wave surface to include nonlinear effects. First, the array was simulated under oblique regular waves to calibrate connector stiffness and possible hydrodynamic drag in the fins. Then and as a novelty, more realistic irregular wave conditions were simulated and the results compared with those under regular waves. For this purpose, a set of random realizations under irregular waves were carried out to obtain statistics on the maximum instantaneous forces in the connections.

The remainder of the paper is structured as follows. Section 2 describes the numerical modelling approach applied, including the pontoon geometry, frequency and time-domain analyses, and calibration of the numerical model. The results are presented and discussed in Section 3. Finally, conclusions are drawn in Section 4.

2. Materials and methods

In this study, we analysed the dynamic response of a pontoon-type modular floating breakwater on waves to estimate the module connector forces, a key point in its structural design. The studied breakwater, previously analysed by Peña et al. (2011), was an array of five floating pontoons interconnected with hinged joints and moored to the seabed with elastic lines at a water depth of $d = 6.75$ m. The detailed geometrical properties of the array are summarized in Fig. 3 and Table 1.

The approach was implemented in Aqwa (ANSYS, 2016), a numerical simulation environment that has been applied successfully to the study of other floating marines structures, such as platform-riser coupling systems (Wang and Liu, 2018) and complex structures such as the Mid Water Arch (Hill et al., 2014), or wave energy converters (López et al., 2017). Moreover, it has already been applied to a floating pontoon module under regular waves (Chen et al., 2017).

2.1. Frequency domain analysis

The floating module response in the frequency domain was characterized using Aqwa Line, a 3D BEM code that applies potential flow theory assuming an ideal fluid, and irrotational flow. The breakwater modules are assumed to be rigid bodies with little oscillation, and in this case, with zero forward speed. Under these assumptions, and a Cartesian

Fig. 4. The individual floating module panel models for the frequency domain analysy (upper panel) and for the time domain analysis (lower panel).

reference system $\mathbf{X} = (X,Y,Z)$, the motion of the fluid around the modules is defined by the velocity potential:

$$\varphi(\mathbf{X},t) \;=\; \mathrm{Re}\left[\varphi(\mathbf{X})e^{-iwt}\right] \tag{1}$$

where: t is the time, ω is the angular frequency, Re denotes "the real part of" and φ is the velocity potential expressed as a function of the spatial coordinates. This potential is commonly distributed in three different terms: incident potential (φ_I), diffracted potential (φ_d) and potential radiated by the m structure due to its own motion at the jth degree of freedom (DoF). Assuming six DoFs and M interacting structures, these velocity potentials are related as follows:

$$\varphi e^{-i\omega t} = \left[\varphi_I + \varphi_d + \sum_{m=1}^{M}\sum_{j=1}^{6}\varphi_{rm}x_{jm}\right]e^{-i\omega t} \tag{2}$$

where x_j represents the motion of the floating body around the jth DoF. The velocity potential of the fluid was estimated by applying the BEM, which transforms the partial derivative problem formulated into integrable surfaces. The forces in the analysis were applied using the pulsating Green function for finite water depth (Green, 2008), satisfying the following conditions:

- On the free surface ($Z = 0$)

$$-\omega^2\varphi + g\frac{\partial\varphi}{\partial Z} = 0 \tag{3}$$

where g is the gravitational acceleration.

- The surfaces of the pontoon modules are impermeable, so the velocity of the particles in contact with them is equal to the velocity of the body

$$\partial\varphi / \partial n = \mathbf{u}\cdot\mathbf{n} \tag{4}$$

where $\partial/\partial n$ represents variation in the direction normal to the module surface and $\mathbf{n}$ is the unitary vector normal to the body surface.

- The velocity potential on the seabed ($Z = d$) is equal to zero

$$\frac{\partial\varphi}{\partial Z} = 0 \tag{5}$$

- The radiation condition, where fluid perturbation is dissipated at long distances from the floating module

$$\lim_{R\to\infty}(\varphi) = 0 \tag{6}$$

for $R = (X^2 + Y^2)^{0.5}$.

For frequency domain analysis of the wave response of a single module in the array, its wetted surface (S_0) was meshed into 12,000 0.35 ± 0.10-m plane quadrilateral diffracting panels (Fig. 4). A second mesh of 3000 0.50 ± 0.10-m diffracting panels was used to reduce the computational cost of time-domain simulation of the complete pontoon array, which would require solving the frequency-dependent hydrodynamic coefficients first and then meshing the full geometry (explained in Section 2.2).

Once the potentials had been determined, the dynamics of a free-floating module subjected to wave action was modelled as a mass-spring mechanical system. Motion response in the frequency domain is governed by:

$$\left[-\omega^2(\mathbf{M}+\mathbf{A}) - i\omega\mathbf{B} + \mathbf{C}\right]\cdot\boldsymbol{\chi} = \mathbf{f}(\omega) \tag{7}$$

where: $\mathbf{M}$ is the structural matrix; $\mathbf{A}$ is the added mass matrix, which accounts for the effect of acceleration induced by the floating body on the nearest fluid particles; $\mathbf{B}$ is the linear damping matrix, which accounts for the wave radiation phenomenon of oscillating floating bodies; $\mathbf{C}$ is the hydrostatic stiffness matrix; $\boldsymbol{\chi}$ is the motion amplitude of the floating module in each DoF; and $\mathbf{f}(\omega)$ is the vector of unitary forces and moments (frequency dependent) acting on the mean wetted surface (S_0).

Matrices $\mathbf{A}$ and $\mathbf{B}$ are frequency-dependent hydrodynamic coefficients, which depend on the geometry of the body and water depth as given by:

$$\mathbf{A} = \frac{\rho}{\omega}\int_{S_0}\mathrm{Im}[\varphi_r]\mathbf{n}dS, \text{ and} \tag{8}$$

$$\mathbf{B} = -\rho\int_{S_0}\mathrm{Re}[\varphi_r]\mathbf{n}_j dS \tag{9}$$

respectively, where: Im denotes "the imaginary part of", Re denotes "the real part of", and ρ is the seawater density. If the pontoon module is considered a floating body with zero forward speed and no current, then $\mathbf{A}$ and $\mathbf{B}$ are symmetric (Faltinsen, 1993). Due to the symmetric geometry of the pontoon around the vertical planes (XZ and YZ) the terms outside the main diagonals (related to these planes) of both matrices are null, so that

$$\mathbf{A} = \begin{pmatrix} A_{11} & 0 & 0 & 0 & A_{15} & 0 \\ 0 & A_{22} & 0 & A_{24} & 0 & 0 \\ 0 & 0 & A_{33} & 0 & 0 & 0 \\ 0 & A_{42} & 0 & A_{44} & 0 & 0 \\ A_{51} & 0 & 0 & 0 & A_{55} & 0 \\ 0 & 0 & 0 & 0 & 0 & A_{66} \end{pmatrix} \tag{10}$$

$$\mathbf{B} = \begin{pmatrix} B_{11} & 0 & 0 & 0 & B_{15} & 0 \\ 0 & B_{22} & 0 & B_{24} & 0 & 0 \\ 0 & 0 & B_{33} & 0 & 0 & 0 \\ 0 & B_{42} & 0 & B_{44} & 0 & 0 \\ B_{51} & 0 & 0 & 0 & B_{55} & 0 \\ 0 & 0 & 0 & 0 & 0 & B_{66} \end{pmatrix} \tag{11}$$

The linear hydrostatic stiffness matrix $\mathbf{C}$ is given by the geometry of the floating pontoon (CoG position and wetted surface) and the density of the fluid. Since the CoG is above the centre of buoyancy (CoB) and both are aligned on the vertical axis, then $\mathbf{C} = \mathbf{C}^{\mathrm{T}}$. Additionally, due to the symmetry of the pontoon with respect to both vertical planes, all $\mathbf{C}$ components are null except for those in the main diagonal associated with vertical motion (Faltinsen, 1993). For a single pontoon this is

$$\mathbf{C} = \begin{pmatrix} 0 & 0 & 0 & 0 & 0 & 0 \\ 0 & 0 & 0 & 0 & 0 & 0 \\ 0 & 0 & 0.80 & 0 & 0 & 0 \\ 0 & 0 & 0 & 0.94 & 0 & 0 \\ 0 & 0 & 0 & 0 & 26.28 & 0 \\ 0 & 0 & 0 & 0 & 0 & 0 \end{pmatrix} \tag{12}$$

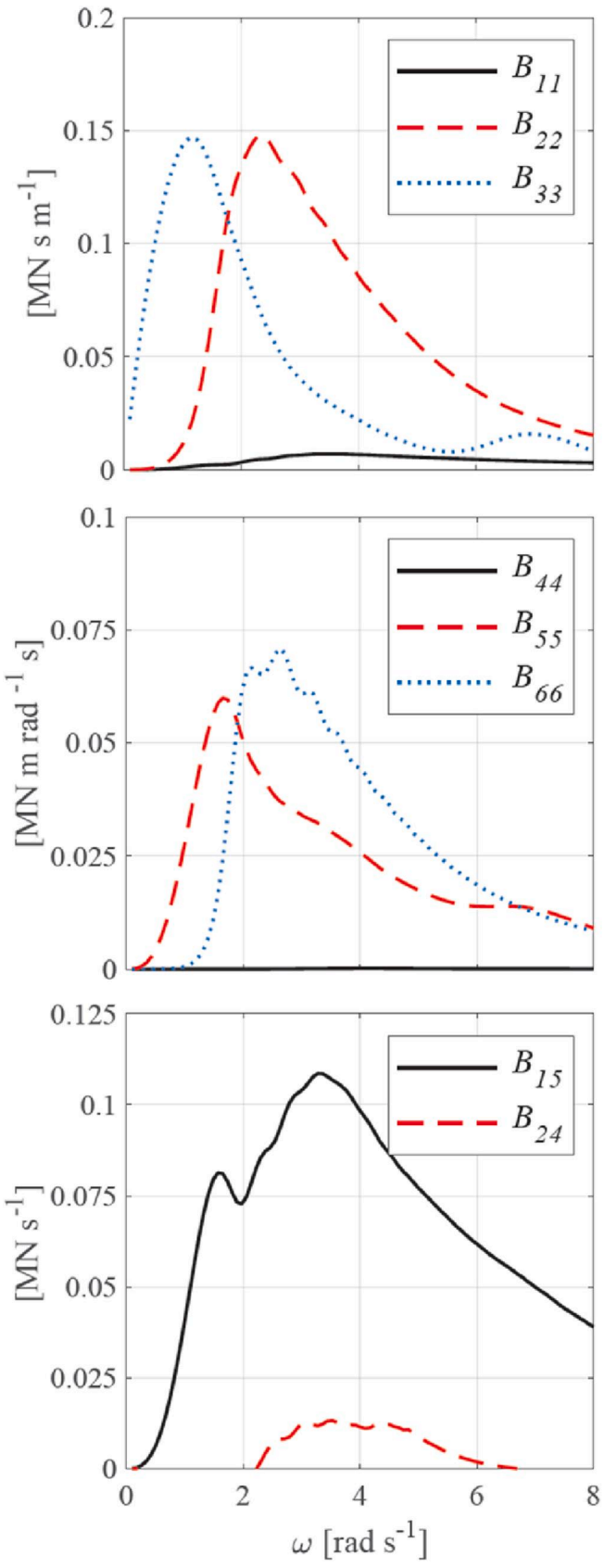

Fig. 7. Components of the hydrodynamic damping matrix (**B**) of a free-floating module: diagonal elements (upper and intermediate panel) and off-diagonal elements (lower panel).

with m_0 the zeroth spectral moment (*i.e.*, the area under the spectral curve); and $\omega_p = 2\pi T_p^{-1}$ is the spectral peak frequency, with T_p the peak wave period. More information regarding the derivation of the Pierson-Moskowitz spectrum can be found in (Pierson and Moskowitz, 1964).

Eq. (26) was used to simulate six irregular wave sea states with equivalent wave energy to the six regular wave conditions analysed by Peña et al. (2011). The heading direction for the long crested irregular waves was also maintained from regular waves ($\Theta = 30°$). This approach allows comparison between the behaviour of the pontoon array under irregular and regular waves. Regular waves present the same wave energy as an irregular wave spectrum with equivalent root mean square wave height, which is defined as

$$H_{RMS} = \sqrt{8m_0} \tag{28}$$

Considering Eqs. (27) and (28) it results $H_s = (2 \cdot H_{RMS})^{0.5}$. Therefore, a value of $H_{RMS} = H = 0.6$ m was considered for the simulations under irregular waves, which results $H_s = 0.84$ m. As for the peak wave period, equivalent values from the regular wave simulations were used, *i.e.* $T_p = T = [2.70, 3.10, 3{,}50, 3.70, 3.85, 4.25]$ s. Fig. 5 shows the Pierson-Moskowitz spectrums for several of the sea states simulated.

Additionally, 20 random wave phase spectrums were used to carry out random realizations of each sea state and subsequently calculate statistical parameters relating to the maximums (DNV, 2018). In order to guarantee wave stationarity while minimizing the computational costs, the duration of the simulations was 2000 s. Note that although 3 h is as a standard time between registrations of sea states when measuring waves (Faltinsen, 1993), a sea state can be described as a stationary random process for time periods in the range from 20 min to 3–6 h (DNV, 2017). As for the duration of the time step, it was 0.01 s.

3. Results and discussion

This section discusses the results of numerical simulation of the floating pontoon breakwater. First, the frequency response of a single free-floating module at different wave frequencies and wave heading directions is described. Then, the time response of an array of hinged modules moored to the seabed by elastic lines to regular and irregular oblique waves is presented along with calibration of the numerical model.

3.1. Frequency domain analysis of a free-floating module

3.1.1. Hydrodynamic coefficients

The hydrodynamic coefficients of a single free-floating pontoon were calculated for a combination of 100 angular frequencies (between $\omega_{\min} = 0.10$ and $\omega_{\max} = 8.00$ rad s^{-1}) and 25 wave heading directions (at equal $\Delta\Theta = 15°$ intervals). The frequency-dependent coefficients found are described below.

The coefficients in added mass matrix **A** are shown in Fig. 6. Among the first three diagonal elements in **A,** which relate longitudinal forces to translational accelerations in the same direction, the highest value was for the vertical mode with $A_{33} = 522.80$ t at the lowest frequency. As for the coefficients corresponding to the horizontal translations, A_{22} peaked at $\omega \approx 1.40$ rad s^{-1} with 99.48 t, while A_{11} was below 5.00 t over the entire frequency range. These results are consistent with the geometry of the module, which has a lower cross-sectional area in the longitudinal than in the transverse direction (Fig. 3).

The diagonal elements of **A**, which relate moment to rotational acceleration, were highest in pitch mode, where $A_{55} = 110.00$ t m^2 rad^{-1} at $\omega = 0.67$ rad s^{-1}. Vertical rotation peaked at $\omega = 1.70$ rad s^{-1} where $A_{66} = 47.41$ t m^2 rad^{-1}, while rotation around the longitudinal axis was negligible ($A_{44} \approx 0$).

Fig. 7 shows the variations in hydrodynamic damping matrix **B** with coefficient frequency. The transverse and vertical translational mode values were highest with $B_{22} \approx B_{33} \approx 150$ kN s m^{-1} around $\omega = 2.40$ rad

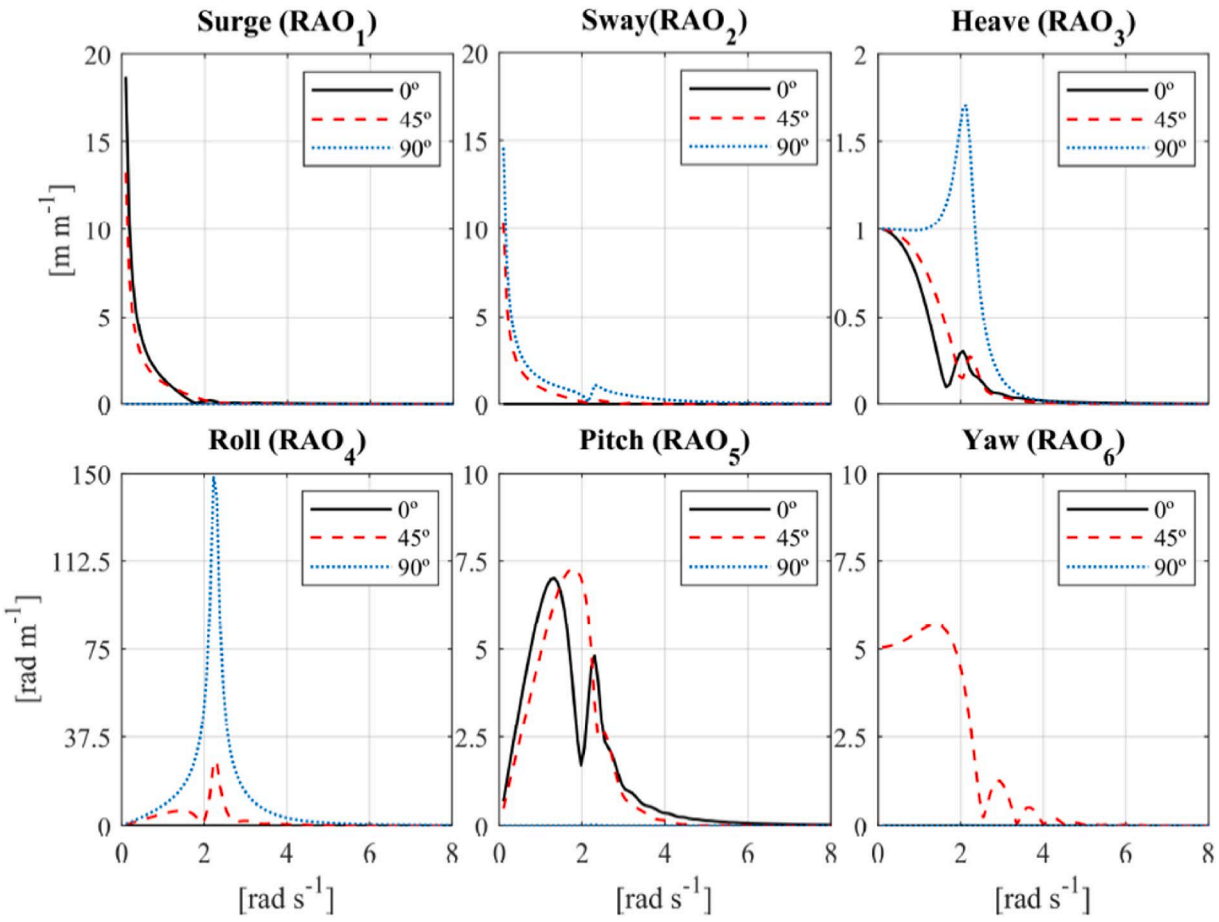

Fig. 8. Response Amplitude Operators (RAOs) without viscous damping effects as a function of the angular frequency (ω) for the 6-DoF and three wave heading directions (Θ = 0, 45 and 90°).

s^{-1} and $\omega = 1.20$ rad s^{-1}, respectively. The hydrodynamic damping for rotation around these axes peaked at about the same frequencies with $B_{55} = 600$ kN m s rad^{-1} and $B_{66} = 710$ kN m s rad^{-1}. In the longitudinal axis modes (B_{11} and B_{44}), damping was rather limited over the full range of frequencies analysed. All coefficients approached zero at low frequencies except for motion-induced damping in heave direction (B_{33}). Coefficients B_{11}, B_{22}, B_{33} and B_{24} also tend to zero at high frequencies within this interval.

As the floating module has zero forward speed and currents are absent, **A** and **B** are symmetric. Furthermore, because the body is symmetrical through both vertical planes, the only nonzero off-diagonal elements in these matrices are those with subindexes 15 and 24. A_{15} peaked at $\omega = 0.60$ rad s^{-1} with 105.20 t m, while A_{24} was lower with a maximum of 41.77 t m. The B_{15} damping coefficient peaked at around $\omega \approx 3.30$ rad s^{-1} with 110 kN m, decreasing to zero at lower frequencies. A similar pattern was found for B_{24}, which peaked at $\omega \approx 3.45$ rad m^{-1} with 10 kN m.

3.1.2. Response Amplitude Operators (RAOs)

Once a hydrodynamic database with the coefficients in **A**, **B** and **C** had been compiled, the modal response of the free-floating module was characterized with Eq. (7). Fig. 8 shows the RAOs for each DoF and three representative wave directions (Θ = 0, 45, and 90°). Note that sway, heave, and roll were only activated for normal heading waves ($\Theta = 90°$), the same applies to surge, heave and pitch for longitudinal heading waves ($\Theta = 0°$).

As expected for a free-floating body, the translational responses on the horizontal plane (surge and sway) increased with the wave period and there were no apparent resonant frequencies. Regarding vertical translations, a resonant frequency of around $\omega \approx 2.00$ rad s^{-1} was found for the $\Theta = 90°$ wave heading, which corresponds to an $RAO_3 \approx 1.75$ m m^{-1}. Apparent peaks at around the same frequency were found for the other two heading directions, but the response was attenuated to less than one in these cases. The response tended toward one at the lowest frequencies (the body oscillates with waves) and tended to zero at the highest.

The highest rotational response was found with roll and a normal heading direction, with a resonant frequency of about $\omega \approx 2.30$ rad s^{-1}. Pitch mode showed two resonant frequencies at $\omega \approx 1.30$ and 2.30 rad s^{-1} for the longitudinal wave heading direction, while in the oblique direction, single resonant frequency was around $\omega \approx 1.80$ rad s^{-1}.

3.2. Time domain analysis of an array of pontoon modules

3.2.1. Time-domain results under regular waves and numerical model calibration

Once the frequency response of a single module had been characterized, an array of five pontoon modules was simulated in the time-domain under oblique regular waves. The mooring lines and the hinged connections between modules were included in the analysis. The test conditions reproduced were: wave height of $H = 0.6$ m, six wave periods of T = [2.70, 3.10, 3,50, 3.70, 3.85, 4.25] s, and wave heading direction of $\Theta = 30°$. The six test cases were simulated for 100 s with a 0.01 s time step in 145 different combinations of C_d and K_{ry}, for a total of 870 simulations. Fig. 9 shows an example of a time series of axial forces, $N(t)$, and yaw moments, $M_z(t)$, for a simulation with $T = 3.5$ s, $C_d = 0$ and $K_{ry} = 286.50$ MN rad^{-1}.

The error surface found from the 162 NRMSE values is shown in

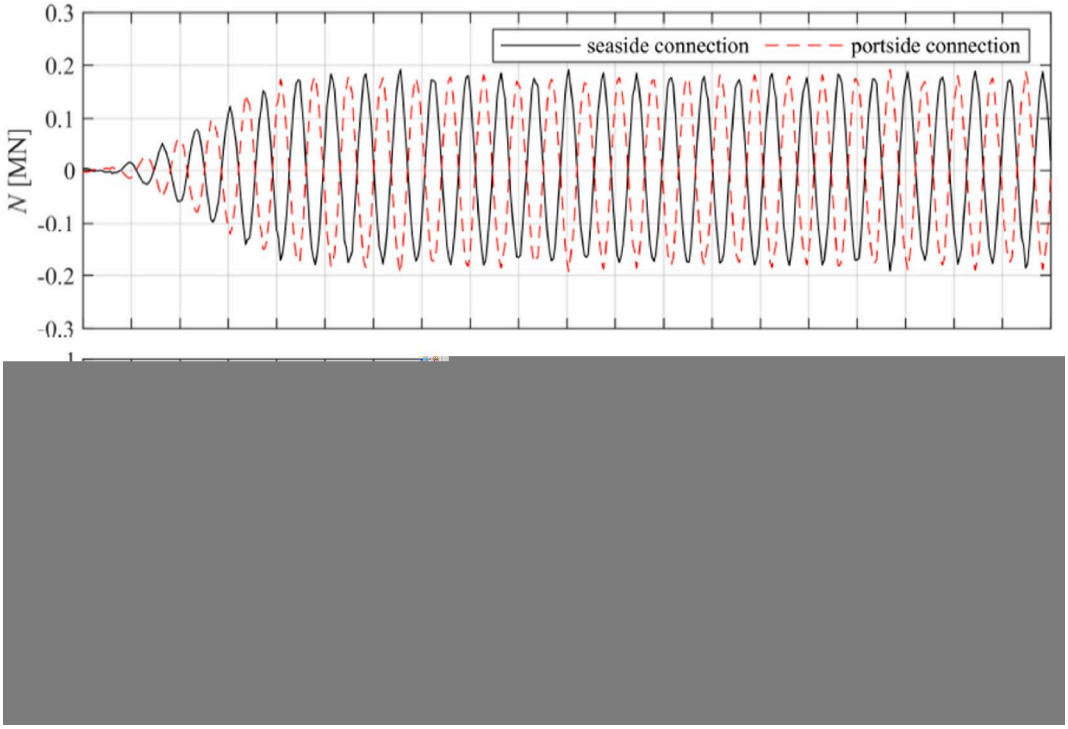

Fig. 9. Time series of axial forces (N) on the connections of joint J_2 (upper panel) and yaw moments on the same joint (M_z) (lower panel). Red circles show the amplitudes after the wave ramp period. Simulation parameters: $H = 0.6$ m, $T = 3.5$ s, $\theta = 30°$, $C_d = 0$ and $K_{ry} = 286.50$ MN rad^{-1}. (For interpretation of the references to colour in this figure legend, the reader is referred to the Web version of this article.)

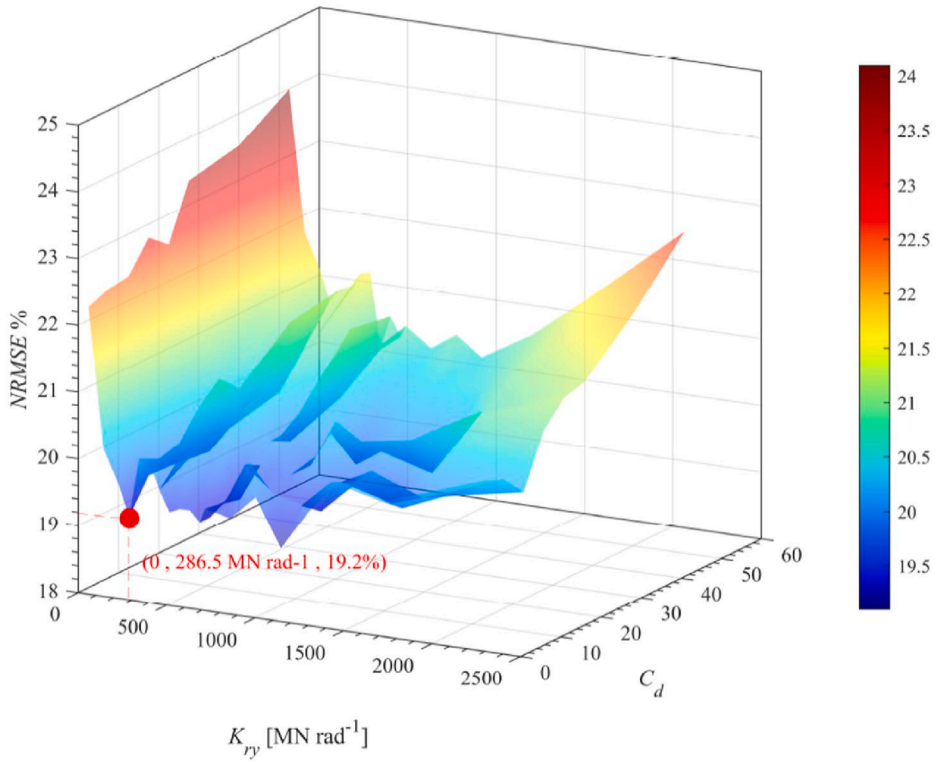

Fig. 10. Normalized Root Mean Square Error (NRMSE in [%]) between M_z obtained for regular wave conditions in the experiments by Peña et al. (2011) and in this work with numerical modelling.

Fig. 10. As observed, the simulation error estimate grew with C_d. In fact, for the same K_{ry}, the error was minimized when C_d tended to zero, which suggests that the hydrodynamic drag of the side fins is negligible. The results showed a clear pattern in the variation in NRMSE with K_{ry}. The deviation in simulations from the experimental tests increased when this parameter was extreme, reaching an NRMSE over 24%. In other words,

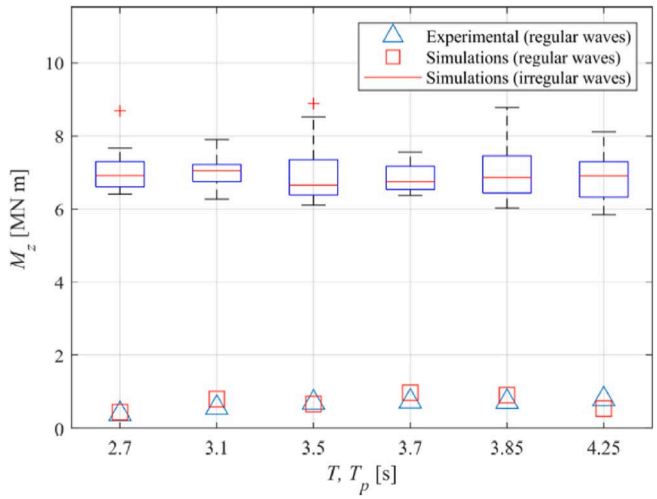

Fig. 11. Maximum M_z for different wave periods found experimentally by Peña et al. (2011) under regular waves, numerically under regular waves and numerically under irregular waves (statistics are provided in boxes: the red central marks indicate the median, the bottom and top edges indicate the 25 and 75th percentiles, the whiskers extend to the most extreme data points not considered outliers, and the outliers are plotted individually using the red '+' marker symbol. Simulation parameters: $C_d = 0$ and $K_{ry} = 286.50$ MN rad^{-1}. (For interpretation of the references to colour in this figure legend, the reader is referred to the Web version of this article.)

if the connections in the numerical model are too rigid or too flexible, it is unable to accurately reproduce the force system between the pontoon modules.

$K_{ry} = 286.50$ MN rad^{-1} and $C_d = 0$ minimized the error estimate with an NRMSE = 19%. The M_z found with the numerical model for these values was in good agreement with the results from previous experimental work (Fig. 11). The numerical model is therefore able to reproduce the behaviour of the floating breakwater and, particularly, the forces in the connection system, which is a key issue in its design.

3.2.2. *Time-domain results under irregular waves*

The time-domain numerical model calibrated in the previous section was used to simulate the behaviour of the same pontoon array, but under more realistic wave conditions. Long-crested irregular waves were reproduced with the Pierson-Moskowitz spectrum (Eq. (26)) preserving the wave energy from the six regular wave conditions in the regular wave analysis. The sea states were for single values of the significant wave height and the wave heading direction ($H_s = 0.84$ m and $\Theta = 30°$, respectively), and six different values of the wave peak period (T_p = [2.70, 3.10, 3,50, 3.70, 3.85, 4.25] s). As an example of the results, Fig. 12 shows samples of the time series of the water surface elevation, $\eta(t)$, the axial forces in the connectors, $N(t)$, and the moments around the vertical axis in a joint, $M_z(t)$, for a particular simulation.

A total of 20 random simulations of each sea state were conducted to obtain their corresponding maximum values of M_z and obtain the statistics for each sea state, which are summarized in Fig. 11. With an unique exception, the maximum moments exceeded $M_z = 6.00$ MN m for all simulations. The highest values were found for the sea state with T_p = 2.7 s, with an average maximum value of $M_z = 7.71 \pm 0.52$ MN m, while the lowest maximums corresponded to the sea state with $T_p = 3.5$ s, with an average maximum value of 6.70 ± 0.58 MN m. The latter values represent a difference in the maximum values of M_z of about 15% between both sea states. In case of regular waves, the differences between the cases with the lowest and highest moments were much lower: if for $T = 2.7$ s the maximum was $M_z = 0.45$ MN m, the maximum was $M_z = 0.98$ MN m for $T = 3.7$ s, which represents a 118% variation. These results suggest a low influence of the peak wave period in the extreme values of M_z.

On another note, the results for irregular waves showed a significant increase in the maximum moments with respect to the results for regular waves. In fact, the values obtained under irregular waves were one order of magnitude higher than those obtained under regular waves. For instance, the simulation of a regular wave with $T = 3.85$ s resulted in a maximum value of $M_z = 0.91$ MN m, while the simulations of an irregular wave sea state of equivalent wave energy and $T_p = 3.85$ s showed average maximum values of $M_z = 6.77 \pm 0.42$ MN m (Fig. 11). These results underscore the importance of including irregular wave conditions in the analysis of the forces and moments of floating pontoon breakwater connections, and discrepancies are wider for regular waves.

4. Conclusions

The performance of a modular pontoon floating breakwater with elastic mooring lines was examined in the time-domain, focusing on the forces and moments on the hinged connections between the modules, which are of paramount importance in their design. The numerical modelling approach applied found the hydrodynamic response of the floating structure in the frequency-domain with a BEM solver first, and then the time-response using the convolution integral method. The instantaneous forces on the structure were recomputed at each simulation step, including the drag forces on the module fins, and the Froude-Krylov and hydrostatic forces on the wetted surface, which reproduced nonlinear effects. The rotational stiffness of the module connections and the drag forces on the fins of the pontoon were calibrated by comparing the results from the simulations with experimental results found previously. Once the model had been calibrated, the response of the array to long-crested irregular waves was compared to monochromatic waves with equivalent energy. Several conclusions of interest can be drawn from the results.

The numerical modelling approach applied can accurately estimate the force system in the connections between the pontoons in a hinged array. In fact, the values of the moments in the joints between modules found with the time-domain numerical model are in good agreement with the results from previous experimental tests in a wave tank.

From the calibration of the numerical model, it may be inferred that the rotational stiffness of the connections strongly influences simulation results. The best fit of numerical to experimental results was given by $K_{ry} = 286.50$ MN rad^{-1} (with NRMSE = 19%). Far from this value, the model was no longer able to accurately reproduce the forces on the pontoon module connections. On the contrary, the drag forces on the fins are negligible, as the drag coefficient that minimized the error between the numerical and experimental results was zero ($C_d = 0$).

With the same wave energy, the maximum moments in the connections were always higher for irregular than for regular waves, with values one order of magnitude higher. These results highlight the need for take irregular wave theory into consideration in future design and verification of these structures.

Summarizing, the force system of an array of pontoons was solved in the time-domain with a BEM numerical model which also applies nonlinear hydrodynamic effects. As a novelty the approach, was applied to model the structure's response not only to oblique regular waves, but also to irregular waves. The calibration with the results from previous experimental work showed a good agreement, which confirms that the methodology is reliable and feasible to estimate the connection forces on these structures. Importantly, it was concluded that irregular wave conditions should be taken into consideration in future studies to avoid underestimating the forces on the connection elements between modules, a key issue in the design of this type of floating breakwater.

CRediT authorship contribution statement

A.J. Cebada-Relea: Conceptualization, Methodology, Software, Formal analysis, Investigation, Resources, Writing – original draft, Writing – review & editing, Visualization. **M. López:** Conceptualization,

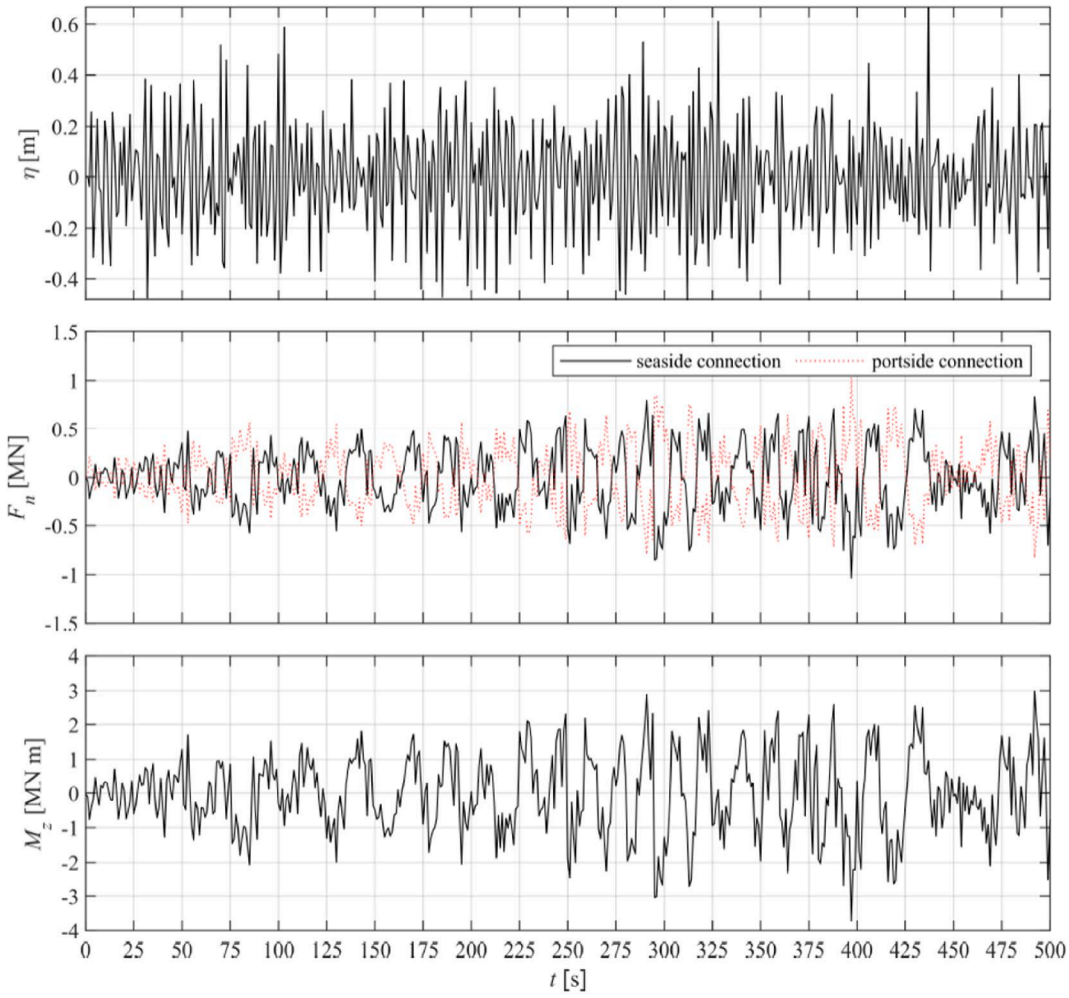

Fig. 12. Time series of water surface elevation (upper panel), axial forces in connections, $N(t)$, in joint *J2* (central panel) and yaw moment, M_z, in *J2* (lower panel) for an irregular wave with $H_s = 0.84$ m and $T_p = 3.5$ s. As an example and for the sake of clarity, only the first 500 s of the simulation are shown.

Methodology, Software, Formal analysis, Investigation, Resources, Writing – original draft, Writing – review & editing, Visualization, Supervision, Project administration, Funding acquisition. **M. Aenlle:** Conceptualization, Methodology, Investigation, Supervision, Funding acquisition.

Declaration of competing interest

The authors declare that they have no known competing financial interests or personal relationships that could have appeared to influence the work reported in this paper.

Acknowledgments

This research was partially funded by Council of Gijón through the University Institute of Industrial Technology of Asturias, grant number SV-21-GIJON-1-21 (the views and opinions expressed herein do not necessarily reflect those of the University Institute of Industrial Technology of Asturias—IUTA).

A. Cebada received financial aid from the University of Oviedo (Asturias, Spain), under the 2019 Research Aid and Promotion Plan (“*Ayudas para realización de Tesis Doctorales. Modalidad A: Contratos de Investigación en régimen de concurrencia competitiva.” [Aid for Ph.D. Dissertation Research, Unit A: Research Contracts with Competitive* Funding, Ref. PAPI-19-PF-16).

Appendix A. Supplementary data

Supplementary data to this article can be found online at https://doi.org/10.1016/j.oceaneng.2021.110263.

References

Abul-Azm, A.G., Gesraha, M.R., 2000. Approximation to the hydrodynamics of floating pontoons under oblique waves. Ocean Eng. 27 (4), 365–384.
Cebada, A., López, M., 2020. Evaluación dinámica para el posible uso de fondeos elástico-lineales en el dique flotante de Figueras (Asturias, España). In: Proc. 3rd Research, Development and Innovation Conference in Civil Engineering, pp. 68–71, 2020-October. (In Spanish).
Borgman, L.E., 1967. Random hydrodynamic forces on objects. Ann. Math. Stat. 38 (1), 37–51.
Ćatipović, I., Ćorak, M., Alujević, N., Parunov, J., 2019. Dynamic analysis of an array of connected floating breakwaters. J. Mar. Sci. Eng. 7 (9).
Chen, Z.J., Wang, Y.X., Dong, H.Y., Zheng, B.X., 2012. Time-domain hydrodynamic analysis of pontoon-plate floating breakwater. Water Sci. Eng. 5 (3), 291–303.
Chen, X., Miao, Y., Tang, X., Liu, J., 2017. Numerical and experimental analysis of a moored pontoon under regular wave in water of finite depth. Ships Offshore Struct. 12 (3), 412–423.
Cheng, L.H., Fen, C.Y., Li, Y.H., Jiang, W.Y., 2020. Experimental study on a new type floating breakwater. Proc. 7th Int. Conf. Asian Pacific Coasts, APAC 429–433, 2013, no. Apac.
Cummins, W.E., 1962. The Impulse Response Function and Ship Motions. Department of the Navy, David W. Taylor Model Basin, Hydromechanics Laboratory, Research and Development Report.
Diamantoulaki, I., Angelides, D.C., 2010. Analysis of performance of hinged floating breakwaters. Eng. Struct. 32 (8), 2407–2423.
Diamantoulaki, I., Angelides, D.C., 2011. Modeling of cable-moored floating breakwaters connected with hinges. Eng. Struct. 33 (5), 1536–1552.

DNV, G.L., 2017. DNVGL-RP-C205: environmental conditions and environmental loads. Recommended Practice. DNV GL.
DNV, G.L., 2018. DNVGL-CG-0130: Wave Loads. Recommended Practice. DNV GL.
Dong, G.H., Zheng, Y.N., Li, Y.C., Teng, B., Guan, C.T., Lin, D.F., 2008. Experiments on wave transmission coefficients of floating breakwaters. Ocean Eng. 35 (8–9), 931–938.
Elchahal, G., Lafon, P., Younes, R., 2009. Design optimization of floating breakwaters with an interdisciplinary fluid-solid structural problem. Can. J. Civ. Eng. 36 (11), 1732–1743.
Faltinsen, O., 1993. Sea Loads on Ships and Offshore Structures, vol. 1. Cambridge university press.
Ferreras, J., Peña, E., López, A., López, F., 2014. Structural performance of a floating breakwater for different mooring line typologies. J. Waterw. Port, Coast. Ocean Eng. 140 (3), 1–11.
Green, G., 2008. An essay on the application of mathematical analysis to the theories of electricity and magnetism. Proc. Camb. Phil. Soc. 7.
Hill, J., Laycock, S., Chai, S., Balash, C., Morand, H., 2014. Hydrodynamic loads and response of a Mid water Arch structure. Ocean Eng. 83, 76–86.
Ji, C., Yang, K., Cheng, Y., Yuan, Z., 2018. Numerical and experimental investigation of interactions between free-surface waves and A floating breakwater with cylindrical-dual/rectangular-single pontoon. China Ocean Eng. 32 (4), 388–399.
Lee, J., Cho, W., 2003. Hydrodynamic analysis of wave interactions with a moored floating breakwater using the element-free Galerkin method. Can. J. Civ. Eng. 30 (4), 720–733.
Liu, Z., Wang, Y., 2020. Numerical investigations and optimizations of typical submerged box-type floating breakwaters using SPH. Ocean Eng. 209, 107475.
Lopez, I., Lopez, M., Iglesias, G., 2015. Artificial neural networks applied to port operability assessment. Ocean Eng. 109, 298–308.
López, M., Taveira-Pinto, F., Rosa-Santos, P., 2017. Numerical modelling of the CECO wave energy converter. Renew. Energy 113, 202–210.
Loukogeorgaki, E., Angelides, D.C., 2005. Stiffness of mooring lines and performance of floating breakwater in three dimensions. Appl. Ocean Res. 27 (4–5), 187–208.
Loukogeorgaki, E., Yagci, O., Sedat Kabdasli, M., 2014. 3D Experimental investigation of the structural response and the effectiveness of a moored floating breakwater with flexibly connected modules. Coast. Eng. 91, 164–180.
Loukogeorgaki, E., Vasileiou, M., Rapanta, E., 2015. 3D experimental and numerical investigation of the performance of a modular floating structure. Proc. Int. Offshore Polar Eng. Conf. 1548–1555, 2015-Janua.
Loukogeorgaki, E., Lentsiou, E.N., Aksel, M., Yagci, O., 2017. Experimental investigation of the hydroelastic and the structural response of a moored pontoon-type modular floating breakwater with flexible connectors. Coast. Eng. 121, 240–254.
Martinelli, L., Ruol, P., Zanuttigh, B., 2008. Wave basin experiments on floating breakwaters with different layouts. Appl. Ocean Res. 30 (3), 199–207.
McCartney, B.L., 1985. Floating breakwater design. J. Waterw. Port, Coast. Ocean Eng. 111 (2), 304–318.
Peña, E., Ferreras, J., Sanchez-Tembleque, F., 2011. Experimental study on wave transmission coefficient, mooring lines and module connector forces with different designs of floating breakwaters. Ocean Eng. 38 (10), 1150–1160.
Pierson Jr., W.J., Moskowitz, L., 1964. A proposed spectral form for fully developed wind seas based on the similarity theory of SA Kitaigorodskii. J. Geophys. Res. 69 (24), 5181–5190.
Ruol, P., Martinelli, L., Pezzutto, P., 2013. Formula to predict transmission for π-type floating breakwaters. J. Waterw. Port, Coast. Ocean Eng. 139 (1), 1–8.
ANSYS, 2016. ANSYS Aqwa. ANSYS Ltd., Canonsburg, PA, USA.
Sannasiraj, S.A., Sundaravadivelu, R., Sundar, V., 2001. Diffraction-radiation of multiple floating structures in directional waves. Ocean Eng. 28 (2), 201–234.
Teng, B., Gou, Y., Wang, G., Cao, G., 2014. And others, "Motion response of hinged multiple floating bodies on local seabed. " in *the Twenty-Fourth International Ocean and Polar Engineering Conference*.
Wang, T., Liu, Y., 2018. Dynamic response of platform-riser coupling system with hydro-pneumatic tensioner. Ocean Eng. 166 (May), 172–181.
Williams, A.N., Lee, H.S., Huang, Z., 2000. Floating pontoon breakwaters. Ocean Eng. 27 (3), 221–240.

3. ANÁLISIS A CORTO PLAZO DE LAS FUERZAS INDUCIDAS POR EL OLEAJE EN LAS CONEXIONES DE UN DIQUE FLOTANTE

3.1. Resumen

El segundo artículo científico lleva por título *Short-term analysis of extreme wave-induced forces on the connections of a floating breakwater*. En el diseño de diques flotantes, una de las tareas más importantes debe ser la evaluación de las cargas extremas inducidas por las olas en las conexiones. Estos son los elementos más débiles de la estructura y, por tanto, se necesitan verificar contra cargas extremas para garantizar la integridad de la estructura. Este estudio proporciona pautas para estimar las fuerzas extremas inducidas por las olas en las conexiones del dique pontón flotante presentado en la publicación anterior. De igual manera, se utilizan herramientas numéricas de cálculo (BEM) para obtener la respuesta de la estructura en el dominio del tiempo. El comportamiento hidrodinámico de la estructura y las conexiones se evalúa para estados de mar moderados de corta duración, con diferentes períodos de pico de oleaje y direcciones de incidencia oblicuas. Se aplicaron dos criterios de selección de picos para obtener las distribuciones de fuerza axial a cada conexión, y se ajustaron varias funciones de densidad de probabilidad (PDF) a los datos resultantes. Finalmente, se estimaron las fuerzas extremas inducidas por el oleaje en cada conexión y estado del mar para dos niveles de excedencia diferentes.

3.2. Contribución

La contribución del autor también ha sido significativa en esta investigación. Ha participado en las tareas de simulación, investigación y análisis de resultados. También ha realizado la escritura del primer borrador de la publicación, su posterior edición y revisión.

3.3. Informe de factor de impacto

A.J. Cebada-Relea, M. López, R. Claus, M. Aenlle. "*Short-term analysis of extreme wave-induced forces on the connections of a floating breakwater*". Ocean Engineering 280 (2023): 114579. Elsevier ISSN: 0029-8018. DOI: 10.1016/j.oceaneng.2023.114579.

Tipo de producción: Artículo científico
Posición de firma: 1

Nº total de autores: 4
Fuente de impacto: WOS (JCR)
Índice de impacto: 4.372

Tipo de soporte: Revista
Grado de contribución: Autor/a o coautor/a de artículo en revista con comité evaluador de admisión externo
Autor de correspondencia: No
Categoría: *Journal*
Revista dentro del 25%: Si

Ocean Engineering 280 (2023) 114579

Contents lists available at ScienceDirect

Ocean Engineering

journal homepage: www.elsevier.com/locate/oceaneng

Short-term analysis of extreme wave-induced forces on the connections of a floating breakwater

A.J. Cebada-Relea, M. López *, R. Claus, M. Aenlle

DyMAST Research Group and Department of Construction and Manufacturing Engineering, University of Oviedo, Polytechnic School of Mieres, 33600, Mieres, Asturias, Spain

ARTICLE INFO

Handling Editor: Prof. A.I. Incecik

Keywords:
Floating breakwater
Short-term analysis
Extreme loads
Numerical modelling
Aqwa

ABSTRACT

In the design of floating breakwaters, assessment of the extreme wave-induced loads on the connections, their weakest element, is required to ensure structure survival. This case study provides guidelines for estimating the extreme wave-induced forces on the connections of a floating breakwater. A Boundary Element Method (BEM) solver was applied to obtain the time-domain response of an array of five pontoons anchored to the sea bottom with elastic mooring lines. The hydrodynamic behaviour of the structure was assessed for short-duration sea states with different wave peak periods and oblique wave directions. Two peak selection criteria were applied to obtain force distributions, and several different probability density functions (PDF) were fitted to the resulting data. The extreme wave-induced forces on every connection and sea state were estimated for two different exceedance levels during a typical 3-h sea state. Based on the results, combination of the Peaks Over Threshold (POT) method and generalized Pareto distribution results is proposed for estimating the wave-induced design forces on the connections of floating pontoon breakwaters.

1. Introduction

Floating breakwaters are considered an economical and eco-friendly alternative to their bottom-founded counterparts (Dai et al., 2018). These structures are deployed to provide shelter in low wave energy environments, such as inner harbour basins or recreational marinas (McCartney, 1985). Although floating breakwaters have been designed and constructed in a wide range of configurations and forms, they usually consist of an array of floating modules moored to the seabed by catenary chains or elastic lines (Fig. 1). This study focused on the pontoon subtype, also referred to as double-pontoon, twin-pontoon, or catamaran-type because of the typical shape of its modules.

Floating pontoon breakwater performance has been demonstrated to be satisfactory, however, the connections between the modules, which have a high failure rate (Ferreras et al., 2014), are their "Achille's Heel" (Richey, 1982). The typical connection is composed of wire ropes and rubber fenders, which are intended to withstand tensile and compression forces, respectively (Fig. 2). The failure mechanism is in the wire ropes, which are unable to withstand the wave-induced forces during extreme sea-states. Wave directionality has a noticeable impact on these forces, and critical conditions tend to occur during oblique sea states (Peña et al., 2011; Diamantoulaki and Angelides, 2010). The wave period and the position of the connection in the array also influence the maximum forces on the connections to a great extent (Diamantoulaki and Angelides, 2010; Martinelli et al., 2008). In addition to being critical structural elements, connection stiffness conditions the performance of the whole structure (Martinelli et al., 2008). Therefore, an exhaustive analysis of the wave-induced forces is required for a proper design of floating pontoon breakwaters.

The wave-induced forces on the connections can be found by numerical modelling. Several 2-D frequency-domain linear models have been applied to study the interaction of floating breakwaters and waves, mainly by finite elements (Elchahal et al., 2009), the element-free Galerkin method (Lee and Cho, 2003), and the boundary element method (BEM) (Williams et al., 2000). Nonetheless, since wave obliquity is directly related to the forces on the connectors, 3-D models are required to account for it, and have been widely applied to simulate floating breakwaters with layouts of differing complexity. Some examples include a standalone moored pontoon (Loukogeorgaki and Angelides, 2005), a free-floating breakwater consisting of hinged modules (Diamantoulaki and Angelides, 2010), and the more realistic case of a hinged cable-moored floating breakwater (Diamantoulaki and

* Corresponding author.
E-mail address: mario.lopez@uniovi.es (M. López).

https://doi.org/10.1016/j.oceaneng.2023.114579
Received 21 February 2023; Received in revised form 29 March 2023; Accepted 12 April 2023
Available online 3 May 2023

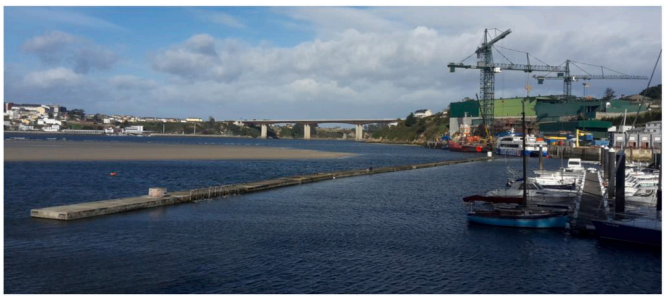

Fig. 1. Pontoon-type floating breakwater in the Port of Figueras (Asturias, Spain).

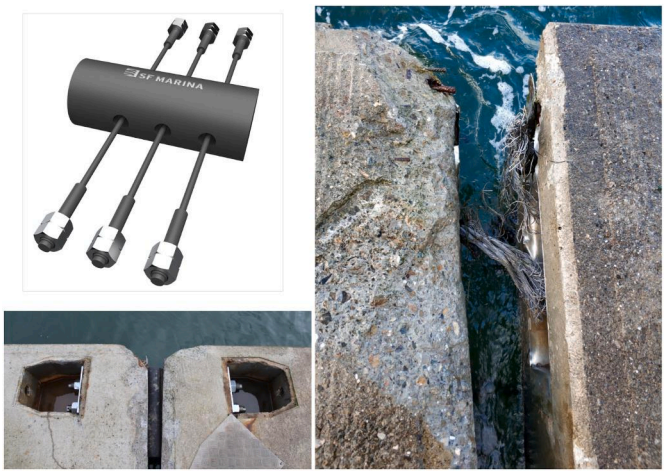

Fig. 2. Semi-rigid floating breakwater connector type (Marina) (upper left), connection installed and working properly (lower left) and broken connection after sea storms (right).

Angelides, 2011). Frequency-domain analysis relies on linearization of the hydrodynamic loads and the system response, and therefore, time-domain simulations are preferred, their higher computational cost notwithstanding (Stanisic et al., 2017). Chen et al. (2017) analysed the response of a moored floating pontoon under regular waves with a 3D model and found good agreement with experimental tests in a wave tank. Regular sea state simulation requires less computational effort than irregular sea states. However, this approach should be applied with caution, as the wave-induced forces on the connections tend to be underestimated (Cebada-Relea et al., 2022a). On this basis, 3D time-domain simulations of irregular sea states are the most appropriate approach for solving the hydrodynamics of floating pontoon breakwaters and finding the wave-induced forces on their connections.

Once the time series of wave-induced forces are found for a given sea state by numerical modelling, their statistical analysis commonly follows. Although the literature in this regard for floating breakwater connections is scarce, there are abundant examples related to the mooring lines of floating structures. For example, Dunja et al. (Stanisic et al., 2018) analysed the peak events on the mooring system of a vessel model subjected to a tropical cyclone environment. The short-term extreme response of a semi-submersible design was also analysed by Sheng et al. (Xu and yanGuedes Soares, 2019). In this study, a hybrid mooring configuration was found using the average conditional exceedance rate method, the global maxima method and the Peaks Over Threshold (POT) method to assess the extreme forces on these elements. Furthermore, previous studies on a scaled point absorber wave energy converter with hybrid mooring have found that generalized Pareto and gamma distributions are suitable for fitting a mooring system peak (Xu et al., 2020; Xu and Guedes Soares, 2021). Other recent studies have also included estimation of the extreme response in complex environments, including station-keeping trials in ice (e.g. (Zhao et al., 2021; Sinsabvarodom et al., 2021)).

Extreme value analysis of a given sea state usually requires a long enough time series and an adequate sampling rate, and especially, multiple simulations or repetitions (Agarwal et al., 2015). The simplest approach is to find the maximum value for each time-domain simulation and select the design load from such statistical quantities as the mean, the most probable maximum (MPM) or a given percentile. However, this approach may be unfeasible for the design of floating pontoon breakwaters, which require time-consuming 3D simulations in the time domain of irregular sea states, for two major reasons. First, sea state duration must be 20 min to 6 h to ensure process stationarity, although a 3-h duration is typically assumed for standardized design procedures (DNV GL, 2017). If only a single peak from each repetition were considered, too many repetitions would be required to obtain accurate statistics (Stanisic et al., 2017, 2018; Zhao et al., 2021). Second, repetition of 3-h simulations requires execution times that are too long. Therefore, some alternative approaches have been proposed for analysing marine structures other than floating breakwaters. For example, Agarwal et al. (2015) used more than one peak per repetition to fit the values to a probability distribution and estimate extreme events. Stanisic et al. (2018) applied the opposite method and estimated the design loads of vessel mooring lines from a single long time simulation.

This study proposed and applied a complete methodology for estimating short-term design forces on the connections of floating pontoon breakwaters from short simulations. The time series of wave-induced forces on the connections of a floating breakwater in this case study were found with a 3D BEM numerical model. A total of nine irregular sea states with different wave peak periods and wave heading angles were analysed. Two peak selection criteria were applied, and different probability density functions were used to fit each dataset. Then, the wave-induced forces for different exceedance probabilities in a typical 3-h sea state were found with the two fits. Some guidelines based on analysis and discussion of the results are provided for the design of floating breakwaters.

The remainder of the paper is structured as follows. Section 2 describes the pontoon array and its main properties, the numerical model scheme, and the short-term statistics applied to fit the results from the simulations and estimate the 3-h extreme forces on the connections. The results are presented and discussed in Section 3, and conclusions are drawn in Section 4.

2. Material and methods

2.1. Case-study breakwater

The breakwater studied consisted of an array of five floating pontoons interconnected with hinged joints and anchored to the seabed with elastic mooring lines at a depth of $d = 6.75$ m. The geometry of the pontoon, its mooring arrangement and its mechanical properties were based on the experimental work of Peña et al. (2011) (Fig. 3).

2.2. Numerical model

The ANSYS Aqwa code was used to simulate the hydrodynamic behaviour of the breakwater. This tool has previously been applied to design a wide variety of marine structures, including: vessels (Rajesh Reguram et al., 2016), wave energy converters (Ramos et al., 2018) and offshore fish cages (Chu et al., 2022). Moreover, Aqwa has already been applied successfully to floating pontoon arrays in regular waves (Chen et al., 2017; Samaei et al., 2016), and more recently, in irregular waves (Cebada Relea et al., 2022; Cebada-Relea et al., 2022b). The numerical modelling scheme and the simulated sea states are described below.

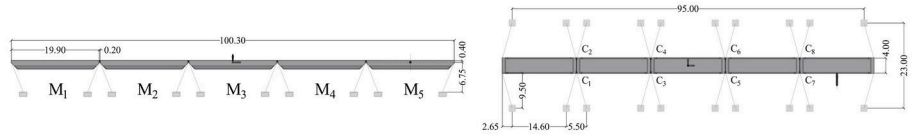

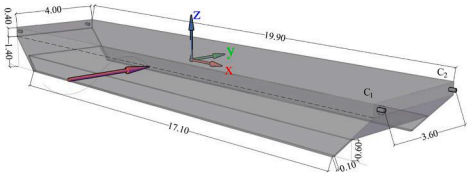

Property	Axis	Value
Displacement (t)	—	40.00
Centre of gravity (m)	X	0
	Y	0
	Z	-0.21
Centre of buoyancy (m)	X	0
	Y	0
	Z	-0.42
Inertia (t·m²)	X	60.94
	Y	1253.82
	Z	1303.98
Radius of gyration (m)	X	1.23
	Y	5.60
	Z	5.70

Fig. 3. Main floating breakwater elements and dimensions [m]. M_m (with m = 1,2, …,5) is the module reference, and C_n (with n = 1,2, …,8) is the connection reference. Based on (Peña et al., 2011).

2.2.1. Numerical modelling scheme

Time-domain simulations in both regular and irregular waves were performed with Aqwa Naut (ANSYS, 2016). The forces on the array were recomputed using a two-stage predictor-corrector algorithm to estimate the positions, velocities, and accelerations of the modules at each time step. The variation in the instantaneous wetted surface of the modules was also included to account for nonlinear hydrodynamic effects. Fig. 4 shows the meshed geometry of a module, featuring the panels above and below the mean water level. A total of 16,000 (0.30 ± 0.1-m) quadrilateral panels were used to mesh the complete array geometry. The results of the mesh convergence analysis are presented under Results.

The motion equation in the time domain is:

$$\mathbf{M}\cdot\ddot{\mathbf{x}}(t) = \mathbf{f}_h(t) + \mathbf{f}_I(t) + \mathbf{f}_d(t) + \mathbf{f}_r(t) + \mathbf{f}_c(t) + \mathbf{f}_m(t) \tag{1}$$

where $\mathbf{x}(t)$ is the displacement from the hydrostatic equilibrium position and $\mathbf{M}$ is the mass matrix of a floating pontoon. This accounts for the hydrostatic $\mathbf{f}_h(t)$, incident wave or Froude-Krylov $\mathbf{f}_I(t)$, diffraction $\mathbf{f}_d(t)$, radiation $\mathbf{f}_r(t)$, connection $\mathbf{f}_c(t)$ and mooring $\mathbf{f}_m(t)$ forces.

The nonlinear hydrostatic force $\mathbf{f}_h(t)$ is calculated as the balance between gravitational forces $\mathbf{f}_g(t)$ and the upward buoyant force. The hydrostatic force, considering the pontoon's instantaneous wetted surface $S(t)$, is given by the following equation:

$$\mathbf{f}_h(t) = \mathbf{f}_g(t) + \rho g \int_{S(t)} p_{st}(t)\mathbf{n}dS \tag{2}$$

where $p_{st}(t)$ is the instantaneous static pressure, ρ is the sea water density, g is the gravity acceleration and $\mathbf{n}$ is the unitary normal vector.

Incident wave forces $\mathbf{f}_I(t)$ are also dependant on the instantaneous wetted surface and are estimated for each time step as

$$\mathbf{f}_I(t) = \int_{S_i} p_{dyn}(t)\ \mathbf{n}dS, \tag{3}$$

where the Wheeler stretching method (Elchahal et al., 2009) is applied to determine the dynamic body pressure $p_{dyn}(t)$.

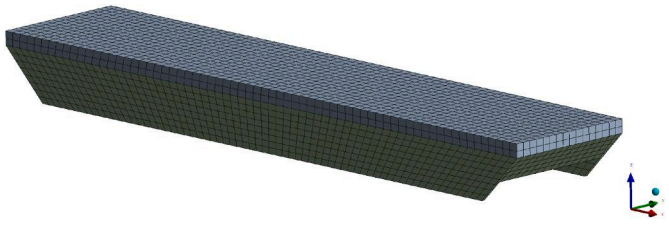

Fig. 4. Meshed geometry of a floating pontoon unit. Green panels are below the mean wetted surface and and grey above.

Diffraction forces, including contributions from all the diffracting panels (those contained in the mean wetted surface, S_0) are computed as:

$$\mathbf{f}_d(t) = -\int_{S_0} p_d(t)\ \mathbf{n}dS \tag{4}$$

where p_d is the diffraction pressure, which is dependent on angular frequency (ω) and can be defined as follows:

$$p_d(t) = i\omega\rho\varphi_d e^{-i\omega t}. \tag{5}$$

The "memory effect" is captured by the radiation force term $\mathbf{f}_r(t)$ (Cummins, 1962):

$$\mathbf{f}_r(t) = -\mathbf{A}_\infty\ddot{\mathbf{x}}(t) - \int_0^t \mathbf{H}(t-\tau)\cdot\ddot{\mathbf{x}}(\tau)d\tau, \tag{6}$$

where $\mathbf{A}_\infty$ is the added mass for an infinite frequency, and $\mathbf{H}$ is the impulse-response function:

$$\mathbf{H}(t) = \frac{2}{\pi}\int_0^\infty \mathbf{B}(\omega)\frac{sin(\omega t)}{\omega}d\omega = \frac{2}{\pi}\int_0^\infty [\mathbf{A}(\omega) - \mathbf{A}_\infty]cos(\omega t)\ d\omega \tag{7}$$

$\mathbf{A}$ is the added mass, and $\mathbf{B}$ is the potential damping. These hydrodynamic coefficients were adopted from a previous frequency domain analysis based on potential flow theory (Cebada-Relea et al., 2022a).

$\mathbf{f}_m(t)$ accounts for the forces on the mooring lines (linear-elastic cables):

$$\mathbf{f}_m(t) = \begin{cases} 0 & \text{if } L(t) \le L_0 \\ K_m(L(t) - L_0) & \text{if } L(t) > L_0 \end{cases}, \tag{8}$$

where $L(t)$ is the instantaneous cable length, L_0 is the starting cable length, and K_m = 30 kN/m is the mooring line stiffness assuming 30% line pretension (Peña et al., 2011).

$\mathbf{f}_c(t)$ accounts for the forces in connection elements C_n (Fig. 3). The longitudinal component is hereinafter referred to as T. At both ends of each connection, there is a hinged joint that transfers forces and restores moments between modules:

$$\mathbf{M} = -\begin{bmatrix} K_{rx} & 0 & 0 \\ 0 & K_{ry} & 0 \\ 0 & 0 & K_{rz} \end{bmatrix}[0, \mathbf{G}^\mathbf{T}]\left[\mathbf{U_p} - \mathbf{U_c}\right], \tag{9}$$

where K_{rx}, K_{ry} and K_{rz} are the rotational stiffness around the principal axes, $\mathbf{G}^\mathbf{T}$, is the unitary change-of-basis matrix from the local joint axes to the main axes, and $\mathbf{U_p}$ and $\mathbf{U_c}$ are the translation and rotation matrices of the pontoon and connectors, respectively. Note that because of the geometrical arrangement (two connections between each pair of modules), the relative translations are restrained and only relative rotation around the Y axis is possible. Joint stiffness, K_{ry}, and the viscous

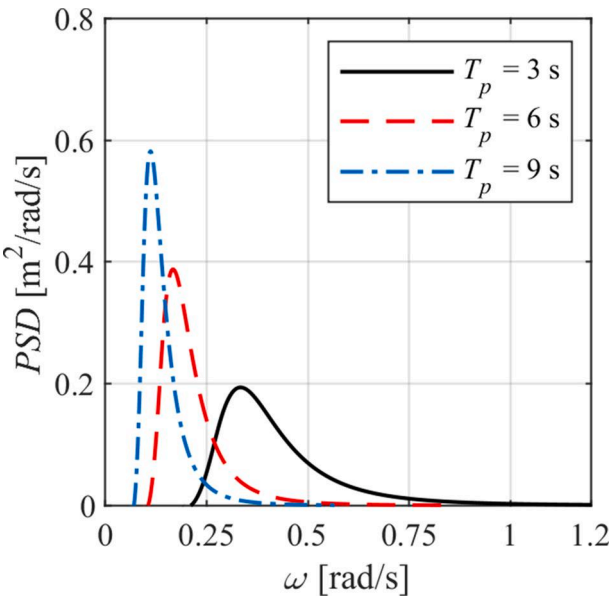

Fig. 5. Pierson-Moskowitz PSD used for the irregular sea state simulations.

damping of the pontoon fins were calibrated by Cebada et al. (Cebada-Relea et al., 2022a) based on experimental results found by Peña et al. (2011).

2.2.2. Irregular sea states and repetitions

A total of nine long-crested irregular sea states, corresponding to a combination of three wave headings of $\theta = 22.5$, 45.0 and 67.5°, where $\theta = 90.0°$ is a wave perpendicular to the breakwater alignment, and three wave spectral peak periods of $T_p = 3$, 6 and 9 s were included. All sea states had the same significant wave height of $H_s = 0.85$ m. In a compromise between accuracy and computation time, the duration of the simulations was set to 2000 s and the time step to 0.01 s.

The Pierson-Moskowitz power spectral density (PSD) (Fig. 5) was used for modelling irregular waves,

$$PSD(\omega) = \frac{4\pi^3}{\omega^5}\frac{H_s^2}{\left(1.408 \cdot T_p\right)^4} e^{\left(\frac{16\pi^3}{\omega\left(1.408 \cdot T_p\right)^4}\right)}. \tag{10}$$

The wave amplitude of each harmonic constituent was found from the PSD for each sea-state, and the wave phases were pseudo-randomly assigned by means of predefined seeds. To capture inherent wave randomness, 20 repetitions of each sea-state were performed with different seeds (DNV GL, 2018) (Fig. 6).

2.3. Short-term extreme value analysis

Twenty repetitions were performed with different random seeds (as described in Section 2.2.2 above). The wave-induced force distributions found from the short-duration time series were then used to develop 3-h force distributions, and finally, to estimate the corresponding design value.

2.3.1. Force peak selection

One of the major issues in exploration of a short-term extreme distribution is the definition and selection of peaks, which are assumed to be random and statistically independent of each other. The zero-up crossing and the Peaks Over Threshold (POT) methods were used for peak selection (Fig. 7). The former defines a peak as the maximum load between two successive zero-up crossings in the time series. The POT method defines a peak as the maximum load within a time window (to ensure independence of the peaks) that is above a given threshold. Although there are no well-established rules for the selection of this threshold, it is usually within the 50th to 95th percentiles of all peak values (Zhao et al., 2021).

2.3.2. Probability distribution models

Since no studies on short-term distribution of the forces on the connections of floating breakwaters are available, the data retrieved form the simulations were fitted using different probability density functions (PDFs). The maximum likelihood method was used to adjust the parameters of each function. Goodness of fit was achieved by means of the normalized root mean square error (NRMSE). The PDFs considered are presented below.

- Weibull PDF,

$$f(x|a_{WB}, b_{WB}) = \frac{b_{WB}}{a_{WB}}\left(\frac{x}{a_{WB}}\right)^{b-1} e^{-\left(\frac{x}{a_{WB}}\right)^{b_{WB}}} \tag{11}$$

where a_{WB} is the scale parameter and b_{WB} the shape parameter.

- Rayleigh PDF,

$$f\left(x\middle|b_{Ray}\right) = \frac{x}{{b_{Ray}}^2} e^{\left(\frac{-x^2}{2{b_{Ray}}^2}\right)} \tag{12}$$

where b_{Ray} is the shape parameter.

- Gamma PDF,

$$f(x|a_{GM}, b_{GM}) = \frac{1}{{b_{GM}}^{a_{GM}}\Gamma(a_{GM})} x^{a_{GM}-1} e^{\frac{-x}{b_{GM}}} \tag{13}$$

where a_{GM} is the shape parameter, b_{GM}, the scale parameter, and Γ the gamma function.

- Generalized Pareto PDF,

$$f(x|k_{GP}, \sigma_{GP}, u_{GP}) = \left(\frac{1}{\sigma_{GP}}\right)\left(1 + k_{GP}\frac{(x-u_{GP})}{\sigma_{GP}}\right)^{-1-\frac{1}{k_{GP}}} \tag{14}$$

where k_{GP} is the shape parameter, σ_{GP}, the scale parameter, and μ_{GP}, the threshold.

- Generalized Extreme Value PDF,

$$f(x|k_{GEV}, \sigma_{GEV}, \mu_{GEV}) = \left(\frac{1}{\sigma_{GEV}}\right) e^{\left(-\left(1+k_{GEV}\frac{(x-\mu_{GEV})}{\sigma_{GEV}}\right)^{-\frac{1}{k_{GEV}}}\right)} \ldots\ldots \left(1 + k_{GEV}\frac{(x-\mu_{GEV})}{\sigma_{GEV}}\right)^{-1-\frac{1}{k_{GEV}}} \tag{15}$$

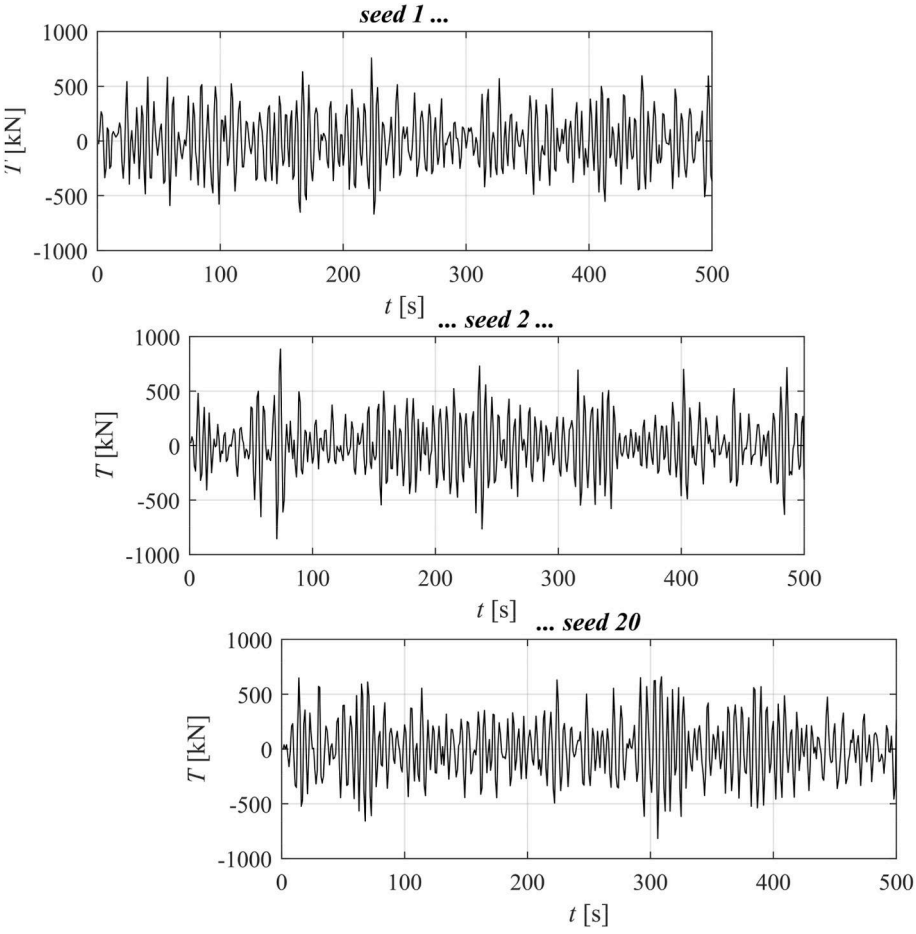

Fig. 6. Time series of wave-induced forces for sea-state 6 found with different seeds.

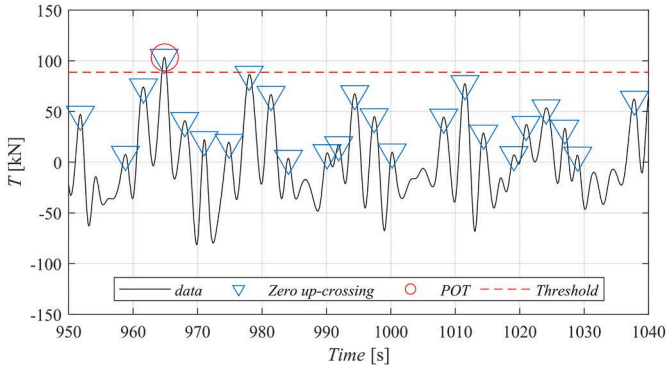

Fig. 7. Example of peak selection with the zero-up crossing and Peakd Over Threshold (POT) methods. The time series is for sea-state 5 ($H_s = 0.85$ m, $T_p =$ 6s and $\theta = 45°$) and Connection C_3.

where k_{GEV} is the shape parameter, σ_{GEV} the scale parameter and μ_{GEV} is the location parameter.

- Half-Normal PDF,

$$f(x|\sigma_{HN},\mu_{HN}) = \sqrt{\frac{2}{\pi}}\frac{1}{\sigma_{HN}}e^{-\frac{1}{2}\left(\frac{x-\mu_{HN}}{\sigma_{HN}}\right)^2} \tag{16}$$

where σ_{HN} is the shape parameter and μ_{HN} is the location parameter.

- Loglogistic PDF,

$$f(x|\sigma_{LG},\mu_{LG}) = \frac{1}{\sigma_{LG}}\frac{1}{x}\frac{e^z}{(1+e^z)^2}, \tag{17}$$

for

$$z = \frac{\log(x)-\mu_{LG}}{\sigma_{LG}}, \tag{18}$$

where σ_{LG} is the scale parameter and μ_{HN} is the location parameter.

2.3.3. 3-H extreme value analysis

The exceedance probability of a given wave-induced force in a 3-h sea-state was found as one minus the cumulative density function (CDF):

$$F_{3h}(x) = 1 - \int_0^{\infty} f(x)^{n_{3h}}dx, \tag{19}$$

where $f(x)$ is the PDF fitted to the peak data found from the short-duration time series, and n_{3h} is the expected number of peaks in a 3-h sea state. The latter parameter was simply obtained as

$$n_{3h} = 5.4n, \tag{20}$$

where n is the average number of peaks in a short-duration time series, which depends on the peak selection criterion and the ratio of 3-h to the duration of the simulations analysed.

In the Most Probable Maximum approach (MPM), the modal value (or mode) of the datasets, which has a 63% probability of exceedance, is usually considered the design value (Stanisic et al., 2017; Xu and yan-Guedes Soares, 2019; Cheng and Kuang, 2016). Other approaches

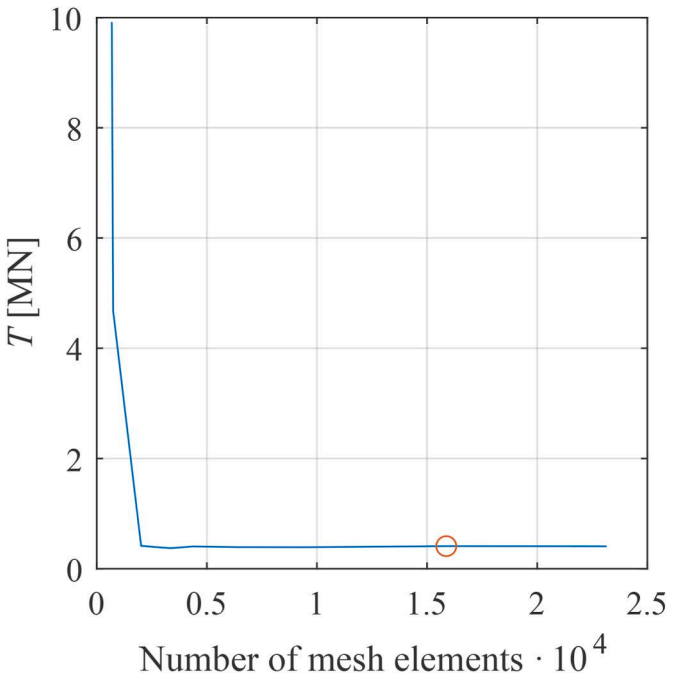

Fig. 8. Results of mesh convergence analysis. The red circle marks the number of elements selected.

consider the 90th percentile of upper values, i.e. 10% probability of exceedance (Stanisic et al., 2017). Accordingly, two of the design force values in each 3-h sea state were found by solving Eq. (19) for $F_{3h} = 0.63$ and 0.10, $T_{0.63}$ and $T_{0.10}$, respectively.

3. Results and discussion

This section explores the wave-induced forces in the floating pontoon breakwater. The simulation results for irregular oblique sea states are presented in terms of the peak wave-induced forces on the connections between modules, which were fitted to well-established probability models. Two different peak selection approaches were applied and compared: zero-up crossing and Peaks Over Threshold (POT). Finally, the design forces for the 3-h sea states are estimated and discussed.

3.1. Mesh convergence analysis

Prior to any analysis, a mesh sensibility analysis was carried out to ensure the independence of the results of the mesh. As an example, Fig. 8 plots the values of the maximum wave-induced force (T) on Connection C_3, found after simulating Sea State 3 ($T_p = 3$ s, $H_s = 0.85$ m, and $\theta = 67.5°$) with different numbers of mesh elements. As shown, mesh independence is ensured for the element size and number of elements (0.30 ± 0.1 m and 16,000, respectively, as in Section 2.2.1) considered.

3.2. Wave-induced force peaks

The behaviour of the floating breakwater in irregular oblique waves was simulated with the numerical modelling approach described in Section 2.2.1. The sea states were defined after combining $T_p = 3$, 6 and 9 s and $\theta = 22.5$, 45.0 and 67.5° in a common significant wave height of $H_s = 0.85$ m, and modelled with the Pierson-Moskowitz spectrum according to Eq. (10) (Fig. 5). Each sea state was simulated 20 times with different spectral wave phases (seeds) to capture wave randomness. The time series of wave-induced forces were retrieved for each simulation and for each connection in the array. To guarantee statistical independence, only force peaks in the time series were considered in the following probability analysis. The zero-up crossing and POT methods were used for peak selection. The results of these two methods are presented and discussed below.

3.2.1. Peaks selected with the zero-up crossing method

First, the wave-induced force peaks were selected with the zero-up crossing method. From 4,000 to 12,000 peaks were identified for each sea state in all 20 repetitions (Table 1). Wave conditions, and in particular, the peak period (T_p) and the wave heading angle (θ), significantly influenced the forces on the connection. For example, the mean force on connection C_3 varied from $\overline{T} = 79.7$ (Sea State 1, $T_p = 3$ s and $\theta = 22.5°$) to $\overline{T} = 1260.5$ kN (Sea State 9, $T_p = 9$ s and $\theta = 67.5°$). It is apparent that the forces on the connections increase both with increasing T_p and θ in the range of sea states included in this study.

All the sea states showed a clear unimodal right-skewed distribution of wave-induced forces (Fig. 9). The relative standard deviation from the mean (RSD) is very similar for all the sea states (Table 1), revealing a common pattern, as the distribution spread is independent of wave conditions. Similar results were found for all the breakwater connections.

As expected, the range of force peaks varied depending on the position of the connection in the array. An example of force distributions on connections C_1 (between the two first pontoons) and C_3 (between two intermediate pontoons) is shown in Fig. 10. The force peak distribution is narrower for C_1 than for C_3, where force values are higher than for the other. This result reveals that the intermediate connections (C_3, C_4, C_5 and C_6 in Fig. 3) can withstand higher wave-induced forces than the terminal connections (C_1, C_2, C_7 and C_8 in Fig. 3).

3.2.2. Peaks selected using the Peaks Over Threshold (POT) method

The wave-induced force peaks were selected with the Peaks Over Threshold (POT) method considering the 75th percentile of the force peaks found with the zero-up crossing method in the section above as the threshold. This threshold minimizes the Normalized Root Mean Square Error (NRMSE) of fit to the force distributions, as shown in Fig. 11. The peak period of the corresponding sea state was used as the time window

Table 1
Statistiscs of force peaks on connection C_3 found with the zero-up crossing method and Peaks Over Threshold (POT) method. Average force ($\overline{T}$) ± standard deviation, relative standard deviation (RSD) and total number of peaks are included for each sea state.

Sea state			Zero-up crossing			Peaks Over Threshold (POT)		
No.	T_p [s]	θ [°]	$\overline{T}$ [kN]	RSD [%]	No. peaks	$\overline{T}$ [kN]	RSD [%]	No. peaks
1	3	22.5	79.7 ± 47.1	59	10768	106.9 ± 31.0	29	2692
2	3	45.0	117.2 ± 69.3	59	11009	158.2 ± 45.1	29	2752
3	3	67.5	246.0 ± 145.5	59	11503	323.9 ± 99.4	31	2876
4	6	22.5	99.6 ± 58.9	59	7790	143.2 ± 33.1	23	1729
5	6	45.0	233.6 ± 138.2	59	7580	318.5 ± 88.0	28	1760
6	6	67.5	525.5 ± 310.8	59	8205	727.0 ± 191.4	26	1966
7	9	22.5	105.7 ± 62.4	59	6627	150.6 ± 35.8	24	1229
8	9	45.0	273.3 ± 161.4	59	5952	379.4 ± 98.3	25	1296
9	9	67.5	1260.5 ± 739.4	59	9748	1619.4 ± 520.8	32	1481

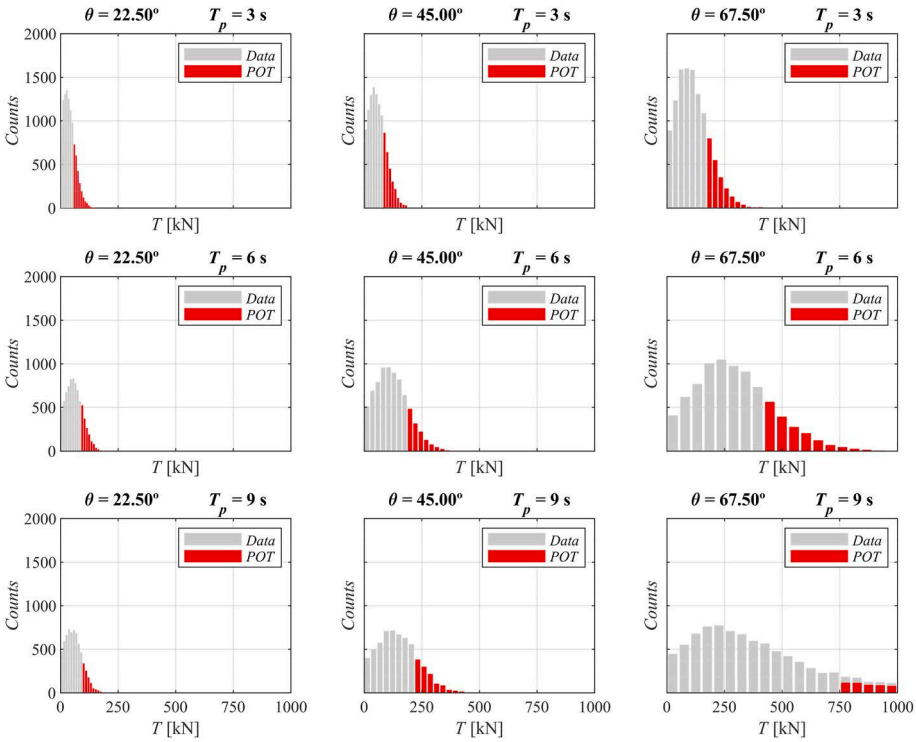

Fig. 9. Histograms of force peaks (T) on Connection C_3 found with the zero-up crossing (grey) and Peaks Over Threshold (POT) (red) methods for each sea state.

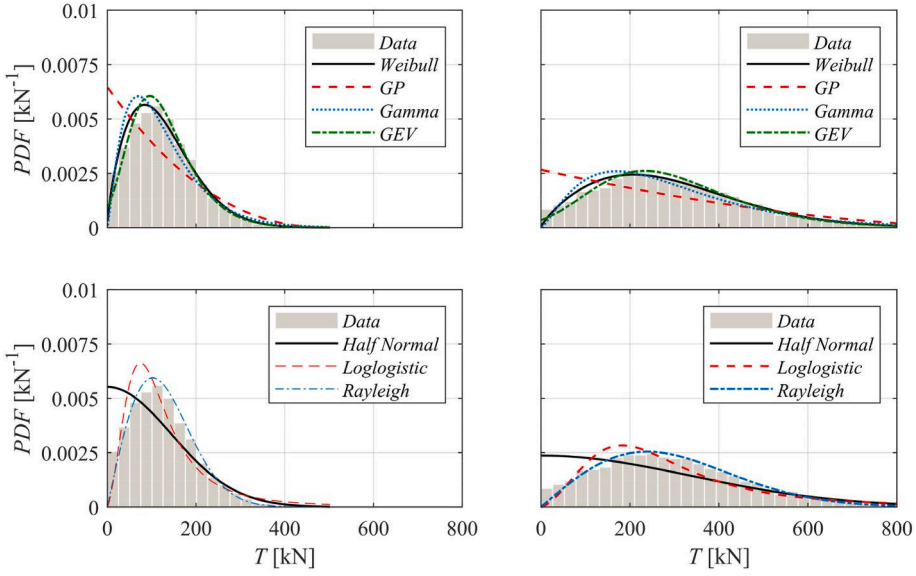

Fig. 10. Histograms of force peaks selected with the zero-up crossing method and fit to probability density functions (PDFs) for Connections C_1 (left) and C_3 (right) at Sea State 6 ($T_p = 6.0$ s and $\theta = 67.5°$).

to ensure that consecutive peak values were independent of each other.

Depending on the sea state, the number of peaks selected with the POT method varied from 1,000 to 3,000, corresponding to an average of 50–150 peaks per simulation (Table 1). Although, as expected, the size of the dataset was significantly smaller than with the zero-up crossing method, it was still large enough for statistical analysis and data fit (Fig. 11).

The POT analysis showed the values of the wave-induced forces (Table 1), confirming the influence of wave conditions and the position of the connection in the array. As expected for an extreme value distribution, the shape of the histograms had a single tail (Fig. 9). Regarding the spread, the POT method results had a lower standard deviation than those found with the zero-up crossing method. Nonetheless, there were wide differences depending on the sea state. For example, distributions corresponding to connection C_3 ranged from RSD = 23% (Sea State 4, $T_p = 6$ s and $\theta = 22.5°$) to 32% (Sea State 9, $T_p = 9$ s and $\theta = 67.5°$) with the POT method, while RSD is nearly constant at around 59% with the zero-up crossing method.

3.3. Peak data fit to PDF

The peak force datasets found with the zero-up crossing method and

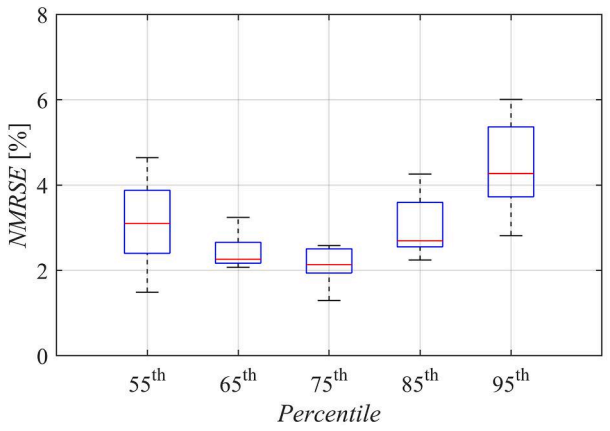

Fig. 11. Normalized Mean Square Error (NRMSE) after fitting the force peaks selected with the POT method to a Pareto PDF as a function of the threshold (expressed as the percentile of force peaks found with the zero-up crossing method). The results are for Sea State 3.

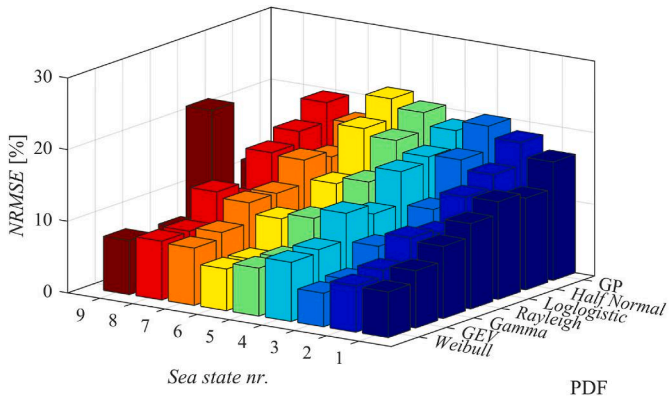

Fig. 12. Average NMRSE between the force peak data obtained with the zero-up crossing method and PDF models at the sea states considered.

the Peaks Over Threshold (POT) method were fitted to the probability density functions (PDFs) defined in Eq. (11) to Eq. (17). The goodness of fit of each PDF to each dataset is presented and discussed below.

3.3.1. Fit of peaks selected with the zero-up crossing method

Fig. 10 shows an example of fit to the force distributions found with different PDFs. Apparently, the Weibull, Rayleigh, gamma and generalized extreme value functions are all suitable for fitting the data with the zero-up crossing method, while the half-normal, loglogistic and generalized Pareto functions are not.

The goodness of fit of each PDF is shown in terms of the NRMSE in Fig. 12. The best fit was usually found with the Weibull distribution with an average NRMSE of about 5%. This PDF fits all the sea states except Sea State 9 the best. The Gamma and Generalized Extreme Value PDFs also had a low NRMSE. The average NRMSE increased to above 15% for the half-normal and the generalized Pareto functions, proving them unsuitable for this fit. Based on this analysis, the Weibull model was selected to fit the force peak data selected with the zero-up crossing method.

Table 2 shows the average parameters of the Weibull distribution (Eq. (11)) for the terminal and intermediate connections. The scale parameter (a_{Wb}) increases with the angle of incidence and the peak period. In addition, its value is higher for intermediate connections, which agrees with the higher wave-induced forces that these connections are subjected to. The average shape parameter (b_{Wb}) varies from 1.1 to 1.8, regardless of the position of the connection or the sea state considered, in accordance with the common pattern previously detected in the distributions.

Table 2
Weibull distribution parameters (average ± standard deviation) found for terminal (C_1, C_2, C_7 and C_8) and intermediate (C_3, C_4, C_5 and C_6) connections.

Sea state			Terminal		Intermediate	
No.	T_p [s]	θ [°]	$\bar{a}_{Wb}$	$\bar{b}_{Wb}$	$\bar{a}_{Wb}$	$\bar{b}_{Wb}$
1	3	22.5	26.11 ± 4.9	1.6 ± 0.1	45.1 ± 2.3	1.5 ± 0.1
2	3	45.0	46.85 ± 5.3	1.7 ± 0.1	68.4 ± 3.2	1.6 ± 0.1
3	3	67.5	96.82 ± 7.2	1.8 ± 0.1	133.3 ± 7.8	1.7 ± 0.1
4	6	22.5	42.52 ± 4.6	1.7 ± 0.1	66.6 ± 2.7	1.6 ± 0.1
5	6	45.0	82.22 ± 5.8	1.8 ± 0.1	135.9 ± 2.4	1.7 ± 0.1
6	6	67.5	143.53 ± 3.8	1.8 ± 0.1	332.5 ± 2.7	1.8 ± 0.1
7	9	22.5	36.64 ± 4.8	1.6 ± 0.1	69.1 ± 3.2	1.6 ± 0.1
8	9	45.0	77.43 ± 4.4	1.7 ± 0.1	161.9 ± 3.8	1.6 ± 0.1
9	9	67.5	289.77 ± 8.9	1.1 ± 0.1	538.5 ± 5.2	1.2 ± 0.1

3.3.2. Fit of peaks selected with the Peaks Over Threshold (POT) method

The fittings of the force distributions found with the POT for a terminal connection (C_1) and an intermediate connection (C_3) are presented in Fig. 13. The goodness of fit of the PDFs is compared in terms of the NRMSE in Fig. 14. In this case the best fit was found with the Generalized Pareto distribution, with an NRMSE of 2–3% for most of the sea-states and connections. The half normal and generalized extreme value distributions also provided a fair fit, while the Weibull, loglogistic, Rayleigh, and Gamma functions are clearly unsuitable for fitting the extreme force peak distribution found using the POT method. As the Generalized Pareto distribution performed better than any other function considered at all sea-states and for all the connections, it was selected for the subsequent extreme value analysis of the wave-induced forces on the connections.

The statistics of the Generalized Pareto function parameters (Eq. (14)) for the terminal (C_1, C_2, C_7, C_8) and intermediate connections (C_3, C_4, C_5 and C_6) at the different sea-states are shown in Table 3. The threshold U_{GP} and scale σ_{GP} parameters increased with wave peak period and wave heading angle. Since central connections are subjected to stronger forces, U_{GP} and σ_{GP} were also higher. Shape parameter values varied in a range of $-0.1 > \bar{k}_{GP} > -0.2$, however, it was close to zero at Sea State 9.

Of the two peak selection methods, the overall best fit was found when the Generalized Pareto distribution was fitted to data selected using the POT method. This approach is therefore recommended for fitting the wave-induced forces on the connections of the floating pontoon breakwater.

3.3.3. Design force for a 3-h sea state

In the sections above, the data from short-duration simulations (2000 s) were used to find the peak force distributions on the connections and fit them to the PDFs. Based on previous findings, two approaches were used to estimate the exceedance probability of a given wave-induced force during a 3-h sea state.

- Approach A: Applies the zero-up crossing method for peak selection, and fits the data to the Weibull PDF.
- Approach B: Applies the POT method for peak selection, and fits the data to the Generalized Pareto PDF.

The probability of exceedance of a given force on C_3 during a 3-h-long sea state (F_{3h}) after applying both approaches is shown at all the sea states in Fig. 15. In general, the exceedance distributions found with Approach B are skewed more to the right than those found with Approach A. It therefore follows that Approach A may underestimate the wave-induced forces on the connections.

The design loads at two different levels of exceedance probability

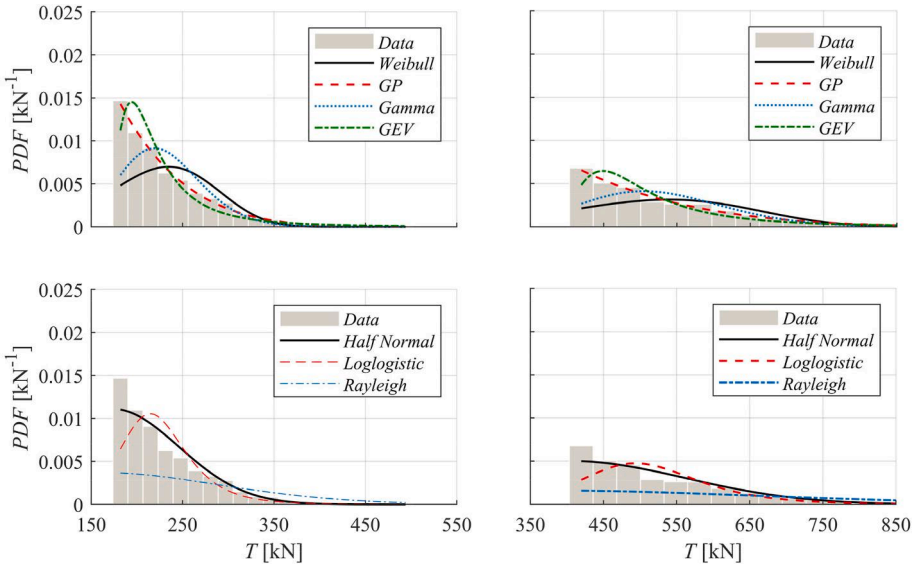

Fig. 13. Histograms of force peaks selected with the Peaks Over Threshold (POT) method and fit to Probability Density Functions (PDFs) for Connections C_1 (left) and C_3 (right) at sea-state 6 ($T_p = 6.0$ s and $\theta = 67.5°$).

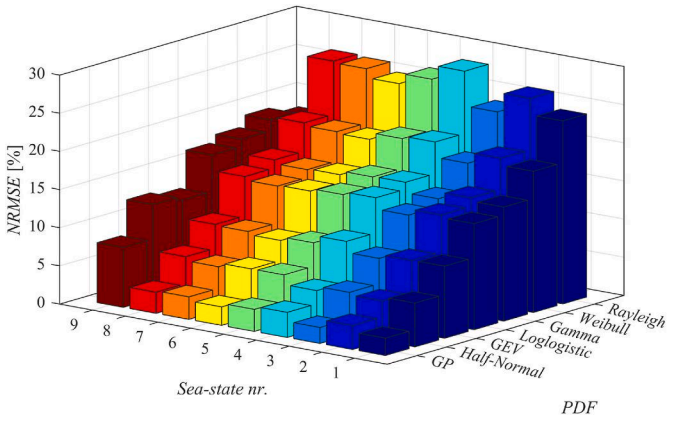

Fig. 14. Average NMRSE between the force peak data found with the Peaks Over Threshold (POT) method and different PDF models at the sea states considered.

($T_{0.63}$ and $T_{0.10}$, as defined in Section 2.3.3) are summarized in Table 4 for both approaches. Since the intermediate connections of the array were expected to withstand higher forces, those results have been selected for discussion. As described above, wave-induced forces increased with the wave peak period and heading angle.

As shown in Fig. 15, Approach B resulted in a higher design force than Approach A ($T_{0.63}$ increased from 74% to 200% and $T_{0.10}$ increased from 17 to 105%, depending on the sea state). The one exception to this pattern is conflictive Sea State 9 above. In this case, Approach A yielded a slightly higher value for $T_{0.63}$ and a much higher value for $T_{0.10}$. The poor fits to this sea state with both approaches may be the reason for this result.

With Approach B, the maximum design forces were expected for Sea State 9 ($T_p = 9$ s and $\theta = 67.5°$), with $T_{0.63} = 879.3$ kN and $T_{0.10} = 917.2$ kN, and the minimums were expected for Sea State 1 ($T_p = 3$ s and $\theta = 22.5°$), with $T_{0.63} = 79.0$ kN and $T_{0.10} = 89.8$ kN. As observed, there was a significant difference in the wave-induced forces at these two sea states. A similar trend was found for the results with Approach A, confirming the influence of the wave parameters on the design connection forces.

Applying Approach A resulted in much wider differences in $T_{0.63}$ and $T_{0.10}$ (64–71%, Table 4) than with Approach B (less than 12%). It may therefore be inferred that the approach selected for finding the probability of exceedance, i.e. the peak selection criterion and the PDF applied for fitting the peaks, has a stronger influence on the design value of the wave-induced forces on the connections than the selection of one probability of exceedance or another.

4. Conclusions

The literature lacks well-stablished recommendations and standards for the design of floating pontoon breakwaters, and in particular, the connections between modules. This article therefore proposed and developed a methodology for defining the wave-induced forces on the connections. For this purpose, an array of five floating pontoons

Table 3
Generalized Pareto distribution parameters (average ± standard deviation) found for terminal (C_1, C_2, C_7 and C_8) and intermediate (C_3, C_4, C_5 and C_6) connections.

Sea state No.	Terminal			Intermediate		
	$\overline{U}_{GP}$	$\overline{k}_{GP} \times 10^{-3}$	$\overline{\sigma}_{GP}$	$\overline{U}_{GP}$	$\overline{k}_{GP} \times 10^{-3}$	$\overline{\sigma}_{GP}$
1	32.3 ± 5.8	−159.0 ± 21.9	12.3 ± 2.0	57.2 ± 2.7	−171.9 ± 8.4	23.4 ± 1.0
2	57.3 ± 6.4	−173.2 ± 31.7	21,3 ± 2.3	86.2 ± 4.0	−178.6 ± 18.7	32.7 ± 1.2
3	116.4 ± 8.4	−142.7 ± 18.8	42,8 ± 3.9	162.9 ± 7.7	−148.7 ± 25.0	60.4 ± 1.6
4	54.2 ± 5.4	−182.3 ± 30.2	18,4 ± 2.1	88.1 ± 3.1	−200.2 ± 24.6	28.7 ± 1.7
5	102.3 ± 6.9	−148.7 ± 31.1	33,8 ± 1.8	172.0 ± 2.5	−173.7 ± 23.8	57.2 ± 1.4
6	179.0 ± 5.1	−138.9 ± 20.7	58,6 ± 2.7	406.8 ± 3.0	−158.6 ± 17.0	134.2 ± 5.1
7	49.8 ± 6.1	−140.6 ± 16.8	15,2 ± 2.4	96.9 ± 5.1	−159.9 ± 45.6	30.1 ± 1.7
8	103.3 ± 4.1	−149.7 ± 15.7	30,6 ± 1.3	210.9 ± 2.8	−153.1 ± 17.7	66.2 ± 2.7
9	387.1 ± 20.1	27.5 ± 18.9	461,7 ± 38.8	727.4 ± 8.5	−340.2 ± 31.0	864.1 ± 43.7

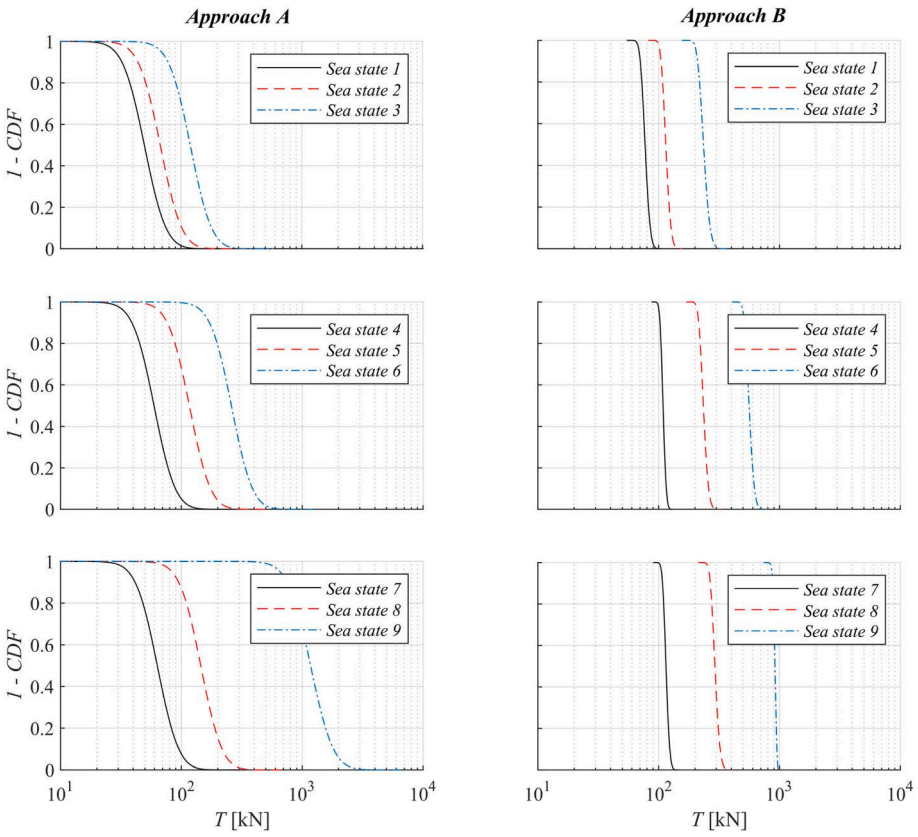

Fig. 15. Probability of exceedance of a given force (T) in a 3-h sea state (F_{3h}) found with Approach A (zero-up crossing method and Weibul distribution, left) and with Approach B (POT method and generalized Pareto Distribution, right) on Connection C_3.

Table 4
Average design wave-induced force on Connections C_3, C_4, C_5 and C_6 for two exceedance probabilities.

Sea state			Approach B (Zero-up crossing and Weibull distribution)		Approach A (POT and Generalized Pareto distribution)	
No.	T_p [s]	θ [°]	$\overline{T}_{0.63}$ [kN]	$\overline{T}_{0.10}$ [kN]	$\overline{T}_{0.63}$ [kN]	$\overline{T}_{0.10}$ [kN]
1	3	22.5	45.5	76.7	79.0	89.8
2	3	45.0	62.3	104.8	115.5	129.7
3	3	67.5	107.2	179.7	229.1	264.0
4	6	22.5	53.4	89.3	110.4	120.8
5	6	45.0	104.70	174.8	225.0	251.1
6	6	67.5	233.41	388.4	543.8	613.8
7	9	22.5	56.8	95.3	128.4	145.1
8	9	45.0	130.1	217.4	281.0	317.3
9	9	67.5	1048.0	1817.6	879.3	917.2

interconnected by hinged joints and anchored to the seabed with elastic mooring lines was analysed. The hydrodynamics and wave-structure interactions were solved by a time-domain numerical model for nine sea states with different wave peak periods and oblique wave directions. The time series found from the short-duration simulations (2000 s) were used to calculate the forces associated with different exceedance levels during a typical 3-h sea state, which could be considered design wave-induced forces.

Two peak selection methods, zero-up crossing and POT, were applied and compared. The best functions for fitting the peak dataset were the Weibull and the Pareto, respectively. For the POT method, the 75th percentile of the force peaks found with the Zero-up Crossing method was considered the threshold, as in general, it provided the best fits.

The analysis confirmed that not only the wave parameters, but also the position of the connection in the floating breakwater is critical to wave-induced forces, as suggested in previous publications. At the sea states considered, the wave-induced forces on the connections increased with peak wave period and obliquity, and intermediate connections withstood much higher forces than terminal connections.

Two approaches were applied and compared for extreme value analysis of the wave-induced forces on the connections.

- Approach A, which applied the zero-up crossing method for the selection of peaks and data fit to the Weibull PDF.
- Approach B, which applied the POT method for peak selection and fit the data to the Generalized Pareto PDF.

Approach A resulted in poorer fit to the force datasets and lower wave-induced force design values. Therefore, as Approach A may underestimate extreme force values, Approach B is recommended for defining the design wave-induced forces on the connections of floating pontoon breakwaters.

Moreover, the differences in design force values found with the two methods were greater than the differences found when using one probability of exceedance or another (63rd and 90th percentiles). Therefore, the application of appropriate peak selection methods in combination with a PDF was found to be paramount.

Summarizing, this article provides guidelines for designing floating breakwaters, including a complete methodology for estimating the extreme wave-induced forces on the connections, the keystone in the design of these structures. Future research should focus on fatigue damage to these elements, which may compromise the lifetime of the entire structure.

CRediT authorship contribution statement

A.J. Cebada-Relea: Conceptualization, Methodology, Software, Formal analysis, Investigation, Resources, Writing – original draft, Writing – review & editing, Visualization. **M. López:** Conceptualization, Methodology, Software, Formal analysis, Investigation, Resources, Writing – original draft, Writing – review & editing, Visualization, Supervision, Project administration, Funding acquisition. **R. Claus:** Conceptualization, Formal analysis, Writing – original draft, Writing – review & editing. **M. Aenlle:** Conceptualization, Methodology, Investigation, Supervision, Funding acquisition.

Declaration of competing interest

The authors declare that they have no known competing financial interests or personal relationships that could have appeared to influence the work reported in this paper.

Data availability

Data will be made available on request.

Acknowledgments

A. Cebada received financial aid from the University of Oviedo (Asturias, Spain) under the 2021 Research Aid and Promotion Plan ("*Ayudas para realización de Tesis Doctorales. Modalidad A: Contratos de Investigación en régimen de concurrencia competitiva.*" [Grant for PhD Students, Unit A: Research Contracts with Competitive Funding], Ref. PAPI-21-PF-31).

References

Agarwal, P., Walker, W., Bhalla, K., 2015. Estimation of Most Probable Maximum from Short-Duration or Undersampled Time-Series Data, pp. 1–8. https://doi.org/10.1115/omae2015-41701.

ANSYS, 2016. ANSYS Aqwa. ANSYS Ltd., Canonsburg, PA, USA.

Cebada Relea, A.J., López Gallego, M., Claus Gómez, R., Soto Pérez, F., 2022. Numerical Investigation of Floating Breakwaters Using Time Domain Boundary Element Method. In: Proc. of the 39th IAHR World Congress (Granada, 2022), p. 4383. https://doi.org/10.3850/IAHR-39WC252171192022379.

Cebada-Relea, A.J., López, M., Aenlle, M., 2022a. Time-domain numerical modelling of the connector forces in a modular pontoon floating breakwater under regular and irregular oblique waves. Ocean Eng. 243, 110263 https://doi.org/10.1016/j.oceaneng.2021.110263.

Cebada-Relea, A., López, M., Soto, F., Claus, R., 2022b. Diques flotantes portuarios: análisis las conexiones y sinergias con la energía undimotriz. Revista española de la Fractura 3, 199–204.

Chen, X., Miao, Y., Tang, X., Liu, J., 2017. Numerical and experimental analysis of a moored pontoon under regular wave in water of finite depth. Ships Offshore Struct. 12, 412–423. https://doi.org/10.1080/17445302.2016.1172831.

Cheng, Z., Kuang, J., 2016. Extreme response predictions for deepwater mooring system. In: Offshore Technol Conf Asia 2016, OTC-26423-MS. https://doi.org/10.4043/26423-ms.

Chu, Y.I., Wang, C.M., Zhang, H., 2022. A frequency domain approach for analyzing motion responses of integrated offshore fish cage and wind turbine under wind and wave actions. Aquacult. Eng. 97, 102241 https://doi.org/10.1016/j.aquaeng.2022.102241.

Cummins, W.E., 1962. The Impulse Response Function and Ship Motions, vol. 57. DTIC Document. https://doi.org/10.1179/2056711115Y.00000000001.

Dai, J., Wang, C.M., Utsunomiya, T., Duan, W., 2018. Review of recent research and developments on floating breakwaters. Ocean Eng. 158, 132–151. https://doi.org/10.1016/j.oceaneng.2018.03.083.

Diamantoulaki, I., Angelides, D.C., 2010. Analysis of performance of hinged floating breakwaters. Eng. Struct. 32, 2407–2423. https://doi.org/10.1016/j.engstruct.2010.04.015.

Diamantoulaki, I., Angelides, D.C., 2011. Modeling of cable-moored floating breakwaters connected with hinges. Eng. Struct. 33, 1536–1552. https://doi.org/10.1016/j.engstruct.2011.01.024.

DNV GL, 2017. DNVGL-RP-C205: environmental conditions and environmental loads.

DNV GL, 2018. DNVGL-CG-0130: Wave Loads.

Elchahal, G., Lafon, P., Younes, R., 2009. Design optimization of floating breakwaters with an interdisciplinary fluid-solid structural problem. Can. J. Civ. Eng. 36, 1732–1743. https://doi.org/10.1139/L09-095.

Ferreras, J., Peña, E., López, A., López, F., 2014. Structural performance of a floating breakwater for different mooring line typologies. J. Waterw. Port, Coast. Ocean Eng. 140, 1–11. https://doi.org/10.1061/(ASCE)WW.1943-5460.0000240.

Lee, J., Cho, W., 2003. Hydrodynamic analysis of wave interactions with a moored floating breakwater using the element-free Galerkin method. Can. J. Civ. Eng. 30, 720–733. https://doi.org/10.1139/l03-020.

Loukogeorgaki, E., Angelides, D.C., 2005. Stiffness of mooring lines and performance of floating breakwater in three dimensions. Appl. Ocean Res. 27, 187–208. https://doi.org/10.1016/j.apor.2005.12.002.

S.F. Marina (n.d).

Martinelli, L., Ruol, P., Zanuttigh, B., 2008. Wave basin experiments on floating breakwaters with different layouts. Appl. Ocean Res. 30, 199–207. https://doi.org/10.1016/j.apor.2008.09.002.

McCartney, B.L., 1985. Floating breakwater design. J. Waterw. Port, Coast. Ocean Eng. 111, 304–318. https://doi.org/10.1061/(asce)0733-950x(1985)111:2(304).

Peña, E., Ferreras, J., Sanchez-Tembleque, F., 2011. Experimental study on wave transmission coefficient, mooring lines and module connector forces with different designs of floating breakwaters. Ocean Eng. 38, 1150–1160. https://doi.org/10.1016/j.oceaneng.2011.05.005.

Rajesh Reguram, B., Surendran, S., Lee, S.K., 2016. Application of fin system to reduce pitch motion. Int. J. Nav. Archit. Ocean Eng. 8, 409–421. https://doi.org/10.1016/j.ijnaoe.2016.05.004.

Ramos, V., López, M., Taveira-Pinto, F., Rosa-Santos, P., 2018. Performance assessment of the CECO wave energy converter: water depth influence. Renew. Energy 117, 341–356. https://doi.org/10.1016/j.renene.2017.10.064.

Richey, E.P., 1982. Floating Breakwater Field Experience. Coastal Engineering Research Center, Vicksburg, MS (US).

Samaei, S., Azarsina, F., Ghahferokhi, M., 2016. Numerical simulation of floating pontoon breakwater with ANSYS AQWA software and validation of the results with laboratory data. Bull. La Société R Des. Sci. Liège 85, 1487–1499.

Sinsabvarodom, C., Leira, B.J., Chai, W., Næss, A., 2021. Short-term extreme mooring loads prediction and fatigue damage evaluation for station-keeping trials in ice. Ocean Eng. 242, 109930 https://doi.org/10.1016/j.oceaneng.2021.109930.

Stanisic, D., Efthymiou, M., Kimiaei, M., Zhao, W., 2017. Evaluation of conventional methods of establishing extreme mooring design loads. Proc. Int. Conf. Offshore Mech. Arct. Eng.OMAE 3A-2017, 2–10. https://doi.org/10.1115/OMAE201761243.

Stanisic, D., Efthymiou, M., Kimiaei, M., Zhao, W., 2018. Design loads and long term distribution of mooring line response of a large weathervaning vessel in a tropical cyclone environment. Mar. Struct. 61, 361–380. https://doi.org/10.1016/j.marstruc.2018.06.004.

Williams, A.N., Lee, H.S., Huang, Z., 2000. Floating pontoon breakwaters. Ocean Eng. 27, 221–240. https://doi.org/10.1016/S0029-8018(98)00056-0.

Xu, S., Guedes Soares, C., 2021. Bayesian analysis of short term extreme mooring tension for a point absorber with mixture of gamma and generalised pareto distributions. Appl. Ocean Res. 110, 102556 https://doi.org/10.1016/j.apor.2021.102556.

Xu, S., yan, Ji C., Guedes Soares, C., 2019. Estimation of short-term extreme responses of a semi-submersible moored by two hybrid mooring systems. Ocean Eng. 190, 106388 https://doi.org/10.1016/j.oceaneng.2019.106388.

Xu, S., Wang, S., Guedes Soares, C., 2020. Experimental investigation on hybrid mooring systems for wave energy converters. Renew. Energy 158, 130–153. https://doi.org/10.1016/j.renene.2020.05.070.

Zhao, Y., Liao, Z., Dong, S., 2021. Estimation of characteristic extreme response for mooring system in a complex ocean environment. Ocean Eng. 225, 108809 https://doi.org/10.1016/j.oceaneng.2021.108809.

4. Evaluación del riesgo de daños por fatiga en las conexiones de los pontones flotantes

4.1. Resumen

El tercer artículo científico publicado se titula *Fatigue damage risk assessment on connections of floating pontoon arrays*. Esta publicación profundiza en el daño por fatiga que soportan los cables de acero trenzado que componen las conexiones del dique flotante. Aquí, se realizaron múltiples simulaciones hidrodinámicas para obtener las series temporales de tensión en cada conexión. Para determinar el daño por fatiga de referencia se empleó el algoritmo Rainflow y la regla de Palmgren-Miner. Este proceso requirió un tiempo de ejecución de 135 días, lo que motivó la introducción de una metodología alternativa para mitigar los costes computacionales. Se calcularon las funciones de transferencia de tensión para cada conexión y dirección de incidencia, derivadas de simular la estructura bajo un espectro de oleaje de ruido blanco. Posteriormente, se implementó el método espectral de fatiga desarrollado por Wirsching-Light que, además, fue validado contra el daño por fatiga de referencia. Los resultados revelan que el daño por fatiga está principalmente influenciado por la dirección de incidencia del oleaje y la posición de las conexiones en el dique flotante. Las conexiones intermedias soportan niveles de daño más altos que las extremas, especialmente bajo un oleaje oblicuo de 60 grados. La metodología alternativa propuesta, muestra precisión en la estimación del daño por fatiga en comparación con las técnicas tradicionales. Su potencial aplicación puede extenderse a otras estructuras flotantes modulares análogas.

4.2. Contribución

En esta investigación el autor ha trabajado en todos los ámbitos. Ha realizado las simulaciones hidrodinámicas y ha analizado los resultados aplicando diferentes enfoques de cálculo del daño por fatiga. Así mismo, también ha participado en la escritura del borrador inicial, de su edición y su revisión. Adicionalmente, el autor ha ejercido como autor de correspondencia, demostrando así su capacidad para la producción y divulgación científica.

4.3. Informe de factor de impacto

A.J. Cebada-Relea, M. Aenlle, M. López. "*Fatigue damage risk assessment on connections of floating pontoon arrays*". Ocean Engineering 299 (2024): 117317. Elsevier ISSN: 0029-8018. DOI: 10.1016/j.oceaneng.2024.117317.

Tipo de producción: Artículo científico
Posición de firma: 1

Nº total de autores: 3
Fuente de impacto: WOS (JCR)
Índice de impacto: 5.0

Tipo de soporte: Revista
Grado de contribución: Autor/a o coautor/a de artículo en revista con comité evaluador de admisión externo
Autor de correspondencia: Si
Categoría: *Journal*
Revista dentro del 25%: Si

Ocean Engineering 299 (2024) 117317

Contents lists available at ScienceDirect

Ocean Engineering

journal homepage: www.elsevier.com/locate/oceaneng

Fatigue damage risk assessment on connections of floating pontoon arrays

A.J. Cebada-Relea *, M. Aenlle, M. López

DyMAST Research Group and Department of Construction and Manufacturing Engineering, University of Oviedo, Polytechnic School of Mieres, 33600, Mieres, Asturias, Spain

ARTICLE INFO

Keywords:
Floating breakwater
Floating structures
Fatigue damage
Rainflow
Spectral fatigue analysis

ABSTRACT

The integrity of floating breakwaters is compromised if their connections are inadequately designed. This article delves into fatigue damage within prestressed stranded ropes of connections in an array of floating pontoons subjected to irregular waves, addressing a gap in research of modular floating structure connections. Hydrodynamic simulations were conducted to capture stress histories on each connection. 20 random-phase repetitions of 27 sea states were analysed, for a total of 540 simulations. The Rainflow algorithm and the Palmgren-Miner's rule were employed to determine the reference fatigue damage. The computational process took a running time of 135 days, prompting the introduction of an alternative methodology to mitigate computational costs. Stress transfer functions, derived from simulating the structure under a white noise wave spectrum, were established for each connection and wave heading direction. Subsequently, the Wirsching-Light method, which was validated against the time domain approach, was implemented. Results reveal significant fatigue damage influenced by wave heading and connection placement. Intermediate connections experienced higher damage levels than extreme ones, particularly under a 60-degree wave alignment. The proposed methodology showcases accuracy in estimating fatigue damage compared to conventional techniques. Its potential application extends to analogous modular floating structures, thereby enhancing the assessment of their reliability.

1. Introduction

In recent years, floating breakwaters have emerged as versatile, mobile, and cost-effective solutions for maritime infrastructure. Among the different types, pontoon-based designs are notable for their adaptability to different water depths, modular construction, and lower environmental impact (McCartney, 1985). Although they are mainly deployed for protecting port waters in mild wave conditions (Fig. 1), such as inner harbour basins or sheltered marinas (Dai et al., 2018), they also have found applications in offshore engineering (Hong et al., 2002), wave energy generation (Zhao et al., 2019), and Very Large Geometry (VLG) Floating Photovoltaic (FPV) arrays (Zhang et al., 2024) Therefore, a methodology for assessing durability becomes essential not only for floating breakwaters but also for other modular floating structures.

Floating pontoons generally perform appropriately, but reported failures particularly in connections highlight vulnerabilities (Richey, 1982). Critical failures are unequivocally associated with the so-called Achilles heel or their weakest elements: the connections between modules (Fig. 2). The technology chosen to link the breakwater modules plays a crucial role as the overall functionality of the entire structure is directly influenced by the stiffness of connections (Ćatipović et al., 2019). In addressing this challenge, its noteworthy that semi-rigid connections – composed of stranded steel wire ropes and neoprene fenders – have emerged as one of the most effective solutions. As a result, designing a modular floating structure requires a comprehensive analysis of the forces acting on connections during its lifetime. One key is ensuring their breaking load is not exceeded under extreme events (Cebada-Relea et al., 2023). Fatigue damage also have a significant role ensuring long-term structural integrity and performance; however, there is a lack of proper investigation into this aspect.

Fatigue analysis starts with the determination of the stress cycles the structure or its elements are subjected to. Determining stress cycles and damage accumulation involves physical tests or numerical modelling of wave-induced forces (Chen et al., 2017; Martinelli et al., 2008). Numerical methods, such as the boundary element method (BEM), offer cost-effective solutions for analysing hydrodynamic responses (Williams et al., 2000).

Once the stress cycles are achieved, the typical fatigue procedure employs the Rainflow counting method combined with a damage model, commonly the Palmgren-Miner's rule (Miner, 2021; Palmgren, 1924).

* Corresponding author.
E-mail address: cebadaalejandro@uniovi.es (A.J. Cebada-Relea).

https://doi.org/10.1016/j.oceaneng.2024.117317
Received 4 January 2024; Received in revised form 16 February 2024; Accepted 26 February 2024

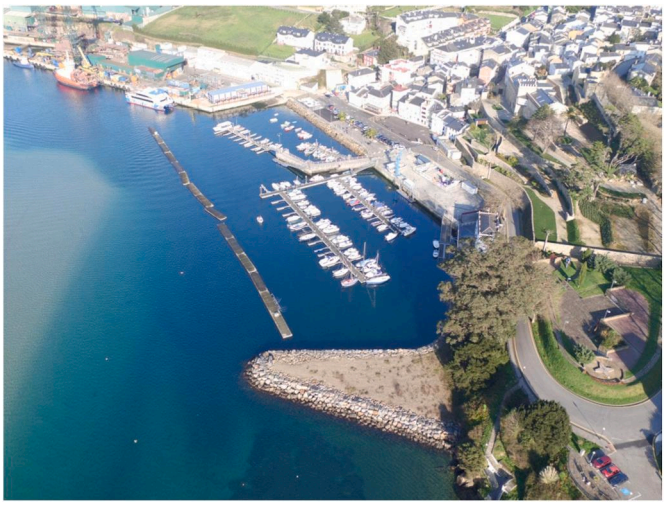

Fig. 1. Aerial photography of the flotating pontoon breakwater in Figueras marine (Asturias, Spain).

The Rainflow algorithm (Matsuichi and Endo, 1968) identifies and counts the number of hysteresis loops in a stress-time history, allowing the estimation of the fatigue damage. Although this approach is able to capture irregular load histories, it may oversimplify material behaviour and becomes highly time-consuming as the length of the stress history increases (Muñiz-Calvente et al., 2022). On these grounds, other alternative fatigue approach based on the frequency domain have emerged. In contrast to the time domain approach, here the stress response is decomposed into its spectral components. Depending on the nature of the process, various spectral fatigue methods have been developed (Zorman et al., 2023). This approach, apart from being faster, allows for a more detailed understanding of the dynamic behaviour and can be used to identify resonant frequencies and modes of vibration that may lead to fatigue failure (Larsen and Irvine, 2015).

Several studies delve into fatigue analysis for floating structures. Some of them are focused on the fatigue damage endured by structural welded unions. (Mourão et al., 2020) developed a methodology for the fatigue assessment in welded components of an offshore jacket-type platform using the notch strain damage parameter. Other studies deal with the fatigue damage on mooring lines. Xu and Soares (2021) explore mooring configurations for a point absorber, evaluating fatigue damage through spectral methods using regular and irregular wave tests. Similarly, Sheng Xu et al. (2022) conducted model tests on a 1:50 scale dual-chamber floating oscillating water column (OWC) device, highlighting the impact of power take-off damping on mooring fatigue damage. Their findings underscore the efficacy of spectral methods in predicting fatigue damage.

This article analyses the fatigue damage in connections of modular floating pontoon arrays. Hydrodynamic simulations were conducted for 27 different sea states, and fatigue damage was assessed using both time-domain and frequency-domain approaches. To diminish computational costs inherent to hydrodynamic simulations, stress transfer functions were derived from white noise wave spectrum simulations. The stress transfer functions combined with an appropriate spectral fatigue method provides accuracy estimations of fatigue damage, reducing the computational time to a great extent, and offers potential applicability to interconnected floating structures.

The reminder of this article is sorted as follows. Section 2 describes the numerical model scheme and the formulation of the fatigue damage by both time-domain and frequency-domain. Section 3 present and discusses the results and the reached conclusions are drawn in section 4.

2. Materials and methods

2.1. Floating pontoon breakwater

The studied structure is the array of five floating pontoons shown in Fig. 3. This structure was initially tested in a wave basin by Peña et al. (2011). In subsequent studies, numerical modelling techniques were applied to analyse its hydrodynamic and the structural performance (e.g., Cebada-Relea et al., 2022; Cebada-Relea et al., 2022; Cebada-Relea et al., 2023). The array configuration, geometry, and general mechanical properties were preserved from these studies, in which the modules are moored to the seabed at depth of 6.8 m through 4 elastic lines each.

The weakness of this type of breakwater lies in the interconnection of

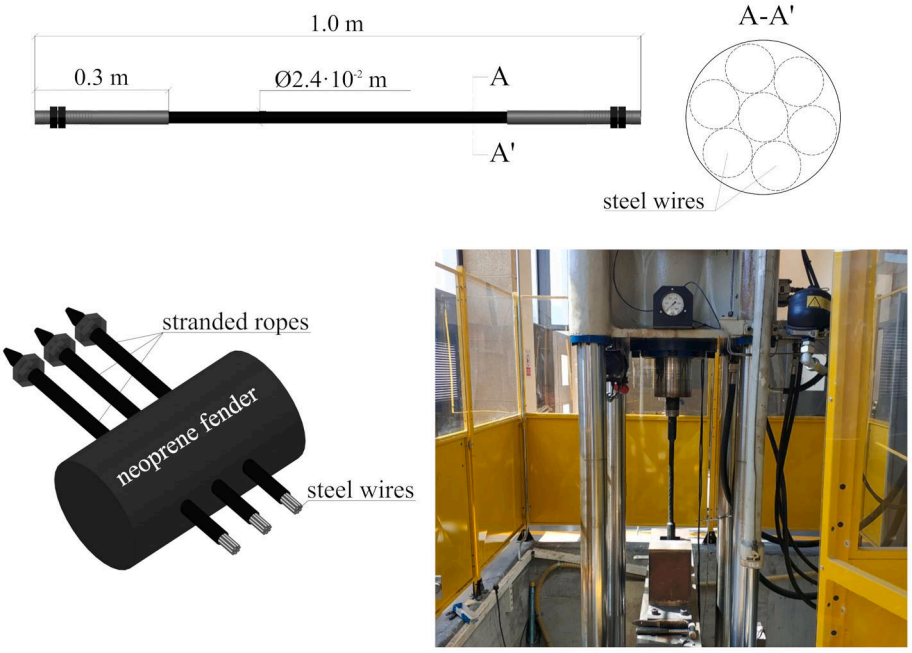

Fig. 2. Detail of semi-rigid connections for the studied floating breakwater and conceptual scheme of the stranded rope (upper and left panels). Breaking load test (right panel).

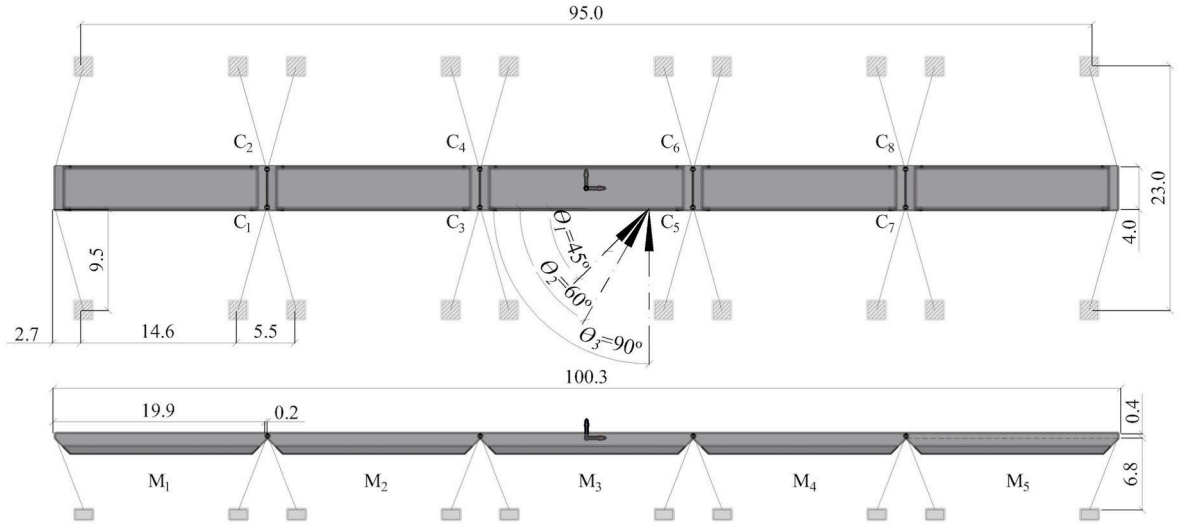

Property	Axis	Value
Displacement (t)	—	40.0
Centre of gravity (m)	X	0
	Y	0
	Z	-0.2
Centre of buoyancy (m)	X	0
	Y	0
	Z	-0.4
Inertia (t·m^2)	X	60.9
	Y	1253.8
	Z	1304.0
Radius of gyration (m)	X	1.2
	Y	5.6
	Z	5.7

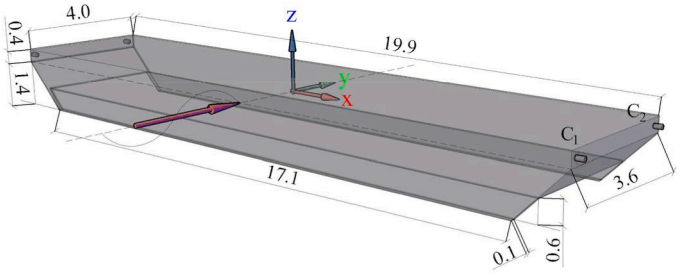

Fig. 3. Main floating breakwater elements, dimensions in [m] and wave headings θ in deg. M_m (with $m = 1,2, \ldots,5$) is the pontoon module reference, and C_n (with $n = 1,2, \ldots,8$) is the connection reference. Based on (Peña et al., 2011).

the pontoon modules. Among the various connection systems used, a typical commercial connection composed of pre-stressed stranded steel ropes and neoprene fenders was considered. This system is frequently referred to as a semi-rigid connection since it allows relative pitching motions between modules. The wire ropes resist tensions, while the fenders resist compressions. Two connections are assumed between each pair of modules, and each includes three ropes and a single neoprene element, as shown in Fig. 2.

2.2. Hydrodynamic simulation and stress analysis

The hydrodynamic interaction of the floating breakwater with waves was simulated with the Line and Naut modules of Ansys Aqwa (ANSYS, 2016). These codes were applied with success to analyse this type of marine structures and to obtain the force system in the connections (e.g., Cebada-Relea et al., 2022; Chen et al., 2017; Samaei et al., 2016). The calibration and validation of the numerical model were presented in the work of (Cebada-Relea et al., 2022).

Initially, Aqwa Line was used to obtain the hydrodynamic coefficients of the pontoon modules in the frequency domain, assuming a free-floating rigid body motion approach. Subsequently, the displacements, velocities, and accelerations of each module were obtained in the time domain with Aqwa Naut, which applies a 2-stage predictor-corrector scheme. A time step of $\Delta t = 0.025$ s was considered and around 3,200 quadrilateral panels of 0.50 ± 0.1 m were used to mesh each module (Fig. 4), resulting in a total of 16,000 elements across the entire geometry.

The motion equation in the time domain is

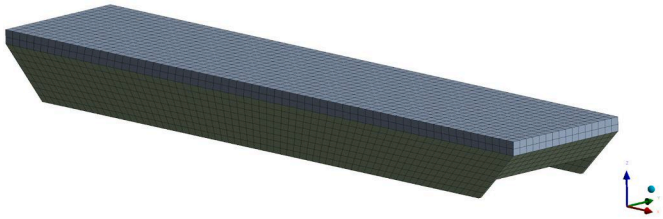

Fig. 4. Meshed geometry of a floating pontoon module. Green and grey panels are below and above the mean wetted surface, respectively.

$$\mathbf{M} \cdot \ddot{\mathbf{x}}(t) = \mathbf{f}_h(t) + \mathbf{f}_I(t) + \mathbf{f}_d(t) + \mathbf{f}_r(t) + \mathbf{f}_c(t) + \mathbf{f}_m(t), \quad (1)$$

where $\mathbf{x}(t)$ is the displacement from the hydrostatic equilibrium position; $\mathbf{M}$ tis he mass matrix of a pontoon module; $\mathbf{f}_h(t)$ accounts for the nonlinear hydrostatic force, calculated as the balance between gravitational forces and upward buoyant forces; $\mathbf{f}_I(t)$ accounts for the Froude-Krylov wave forces; $\mathbf{f}_d(t)$ includes the diffraction forces; $\mathbf{f}_r(t)$ accounts for the radiation forces term and is obtained by means of the convolution impulse-response function; $\mathbf{f}_m(t)$ accounts for the axial forces supported by the linear elastic mooring lines; and $\mathbf{f}_c(t)$ includes the forces and moments transmitted between consecutive modules (more details can be found in references (Cebada-Relea et al., 2022; Cebada-Relea et al., 2023). The stress time history on each wire rope is directly obtained from the force history in the connection. With the longitudinal force acting on a given connection denoted as $F_x(t)$, the stress time history on a

wire rope results,

$$\sigma(t) = \frac{F_x(t)}{A \cdot n_{ropes}}, \tag{2}$$

with $A = 0.25 \cdot \pi \cdot \varphi^2$ the cross-sectional area of the stranded wire rope, where $\varphi = 2.4 \cdot 10^{-2}$ m is the diameter, and $n_{ropes} = 3$, the number of stranded ropes in the connection. The stress power spectral density $S_\sigma(f)$ can be obtained from the stress time history with the Welch method (Welch, 1967).

The excitation forces were defined based on long-crested irregular sea states. Each sea state was characterized by a heading direction and a scalar wave spectrum. The heading direction, denoted as θ, represents the relative angle between the wave propagation direction and the breakwater alignment (Fig. 3). The Pierson-Moskowitz power density spectrum was assumed to represent realistic sea states (Pierson Jr and Moskowitz, 1964),

$$S_w(f) = \frac{5}{16 \cdot T_p^4} \frac{H_s^2}{f^5} e^{\frac{-5}{4} f \cdot T_p^{-4}}, \tag{3}$$

with f the frequency, H_s the significant wave height, and T_p the peak wave period, the period corresponding to the peak wave frequency in the wave spectrum. The significant wave height is defined as

$$H_s = 4\sqrt{m_0} \tag{4}$$

where m_0 is the zeroth spectral moment, obtained from a given spectrum $S(f)$ as

$$m_n = \int_0^\infty f^n \cdot S(f) df \tag{5}$$

for $n = 0$. The 27 sea states simulated were selected based on the typical operational conditions of these structures (Table 1). The wave spectra, corresponding to a significant wave height of $H_s = 0.25$ m are also illustrated in Fig. 5. In addition to the Pierson-Moskowitz spectrum, a white noise wave spectrum was employed to stimulate a broad range of frequencies. White noise is characterized by a uniform distribution of wave power across all frequencies in a specified frequency range. In other words, the power spectral density $S_w(f)$ is constant.

For a given sea state, the relationship between the wave spectrum and the stress spectrum obtained on a particular stranded wire rope can be expressed through the stress transfer functions $H_\sigma^2(f)$ (Xu et al., 2022):

$$H_\sigma^2(f) = \frac{S_\sigma(f)}{S_w(f)}, \tag{6}$$

where $S_\sigma(f)$ and $S_w(f)$ are the stress spectrum and the incident wave spectrum for a given sea state.

For each analysed sea state, a total of 20 realizations were conducted to account for the inherent randomness of the wave behaviour. In each realization, wave phases were pseudo-randomly assigned using a pre-defined seed.

When determining the duration of each sea state, it is typically considered within the range from 20 min to 3 h (DNV GL, 2017). The latter option is computationally expensive, while the former may be too short to ensure the stationarity of the process. In this study, both short- and long-duration sea states were considered, with durations of 30 minutes and 3 hours, respectively.

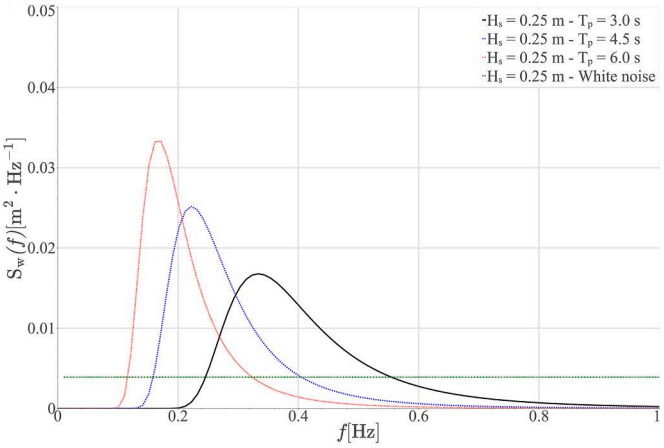

Fig. 5. Pierson-Moskowitz and white noise wave power density spectra.

2.3. Fatigue damage analysis

2.3.1. Fatigue characterization of stranded ropes

The elements to be analysed for fatigue damage are the stranded wire ropes of the various connections in the array, since the connection failure occurs if any one stranded rope breaks. The most common approach to characterize the fatigue behaviour of any material under cyclic loading conditions is through the use of Stress-Number of cycles (S-N) curves, also known as Wöhler curves (Muñiz-Calvente et al., 2022). The relationship between stress ranges ($\Delta\sigma$) or stress amplitudes ($\sigma_{amp} = 0.5 \cdot \Delta\sigma$) and the value of N leading to fatigue failure was defined according to the Basquin model as

$$N = C\left(G_f \cdot \Delta\sigma\right)^{-k}, \tag{7}$$

where $C = 3.4 \cdot 10^{14}$ is the intercept parameter, G_f is the Goodman factor, and $k = 4$ is the slope of the curve, both empirical parameters defined for a stranded wire rope according to DNV standards (GL, 2018) (Fig. 6). In specific applications and materials, an endurance limit is considered (σ_{end}). However, stranded ropes are generally not considered to have a well-defined endurance limit due to their complex structure and the presence of multiple wires.

The effect of the mean stress on fatigue damage was accounted for by means of the Goodman factor G_f in Eq. (7) (Goodman, 1899). Assuming an endurance limit $\sigma_{end} = 0$, it is given by

$$G_f = 1 - \left(\sigma_m \cdot \sigma_u^{-1}\right), \tag{8}$$

where $\sigma_u = F_u \cdot A^{-1}$ is the ultimate stress calculated from the axial

Table 1
Pirson-Moskowitz sea state parameters simulated for different wave conditions.

Sea state no	H_s [m]	T_p [s]	θ [deg]	Sea state no	H_s [m]	T_p [s]	θ [deg]	Sea state no	H_s [m]	T_p [s]	θ [deg]
1	0.05	3.00	45	10	0.15	3.00	45	19	0.25	3.00	45
2	0.05	3.00	60	11	0.15	3.00	60	20	0.25	3.00	60
3	0.05	3.00	90	12	0.15	3.00	90	21	0.25	3.00	90
4	0.05	4.50	45	13	0.15	4.50	45	22	0.25	4.50	45
5	0.05	4.50	60	14	0.15	4.50	60	23	0.25	4.50	60
6	0.05	4.50	90	15	0.15	4.50	90	24	0.25	4.50	90
7	0.05	6.00	45	16	0.15	6.00	45	25	0.25	6.00	45
8	0.05	6.00	60	17	0.15	6.00	60	26	0.25	6.00	60
9	0.05	6.00	90	18	0.15	6.00	90	27	0.25	6.00	90

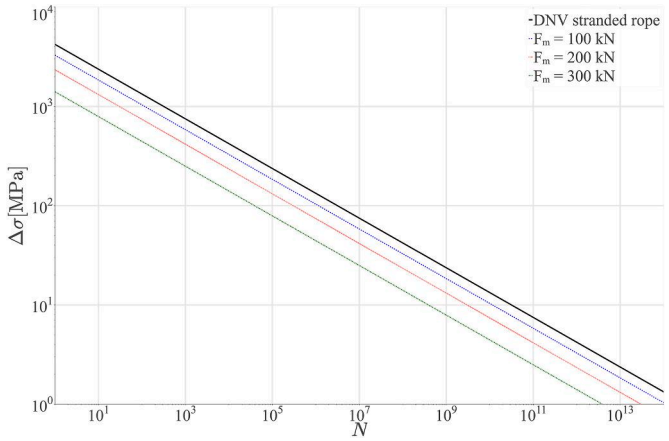

Fig. 6. Effect of mean stress axial pretension force F_m over stranded rope S-N curve (GL, 2018).

breaking load of the wire rope $F_u = 450$ kN (Cebada-Relea et al., 2022) and $\sigma_m = F_m \cdot A^{-1}$ is the mean stress in the wire rope for a given level of pre-stress axial force. Three different levels of mean stress corresponding to $F_m = [100, 200, 300]$ kN were considered for analysis, resulting in the three S-N curves shown in Fig. 6.

2.3.2. Time domain approach

Once the stress time history $\sigma(t)$ on the stranded ropes of the different connections in the array was obtained for a given simulation, a counting algorithm was required to define the stress cycles needed to assess fatigue damage. In this study, the Rainflow counting algorithm (RFC) (Matsuichi and Endo, 1968) was applied. Accordingly, stress cycles were counted in terms of the stress range ($\Delta\sigma$) and the mean stress (σ_m). Subsequently, fatigue damage (D) was calculated using the rule proposed by Palmgren and Miner (Miner, 2021; Palmgren, 1924). For a given simulation, the damage was calculated as

$$D = \sum_{i=1}^{n_t} n_i \cdot N_i^{-1}, \tag{9}$$

where n_i and N_i are the count of cycles and the number of cycles leading to fatigue failure for each stress cycle i, respectively, and n_t is the total number of stress cycles.

For each sea state, characterized by its significant wave height (H_s), peak period (T_p), and heading direction (θ), a total of 20 random phase simulations were performed. Fatigue damage was calculated for each repetition to obtain an average damage value representative of the sea state, $\overline{D}$. While the RFC algorithm, coupled with the Palmgren-Miner rule, is generally considered the most accurate approach for estimating fatigue damage (Dowling, 1971), simulating multiple repetitions of each sea state of interest in the time domain can be computationally demanding in terms of simulation times. Alternatively, spectral methods may offer a cost-effective alternative for assessing fatigue damage in engineering applications.

2.3.3. Spectral approach

There are numerous spectral fatigue models, and the choice of a particular model depends on the application. Commonly, this selection is made by assessing the relative width of the stress spectrum, which can be defined in terms of different parameters. For example, the family of bandwidth parameters α_i are defined by (Lutes and Sarkani, 1997)

$$\alpha_i = \frac{m_i}{\sqrt{m_0 \cdot m_{2i}}}, \tag{10}$$

where m_i, m_0 and m_{2i} are spectral i-th, zeroth and $2i$-th spectral moments, respectively, given by Eq. (5). For broadband processes, their value tends toward zero, whereas for narrowband processes, it approaches unity. Among them, the irregularity factor α_2 is the most frequently employed.

Other alternatives include the spectral width parameter ε and the Vanmarcke bandwidth parameter ε_V, which are defined as (Vanmarcke, 1972)

$$\varepsilon = \sqrt{1 - \alpha_2^2}, \tag{11}$$

and

$$\varepsilon_V = \sqrt{1 - \alpha_1^2}, \tag{12}$$

respectively. In contrast to α_i, both exhibit values close to zero for narrowband processes and close to unit for broadband processes. In addition to the signal bandwidth parameters, it is also interesting to check the Gaussianity of the process since this aspect might limit the applicability of spectral damage models. Normality testing was used to discriminate whether the distribution of loads in the stranded steel wire ropes matches a normal distribution. The well-known test developed by Shapiro-Wilk (Shapiro and Wilk, 1965) was implemented to found the statistical p-values of the time histories, assuming a significance level of 5%.

- Spectral method for a narrowband random process.

For a stationary Gaussian process, the damage in the frequency domain is expressed by means of combining Eqs. (7) and (9). The damage is defined in terms of damage rate or damage per unit time (Slavič et al., 2020):

$$\widehat{D} = V_p \cdot C^{-1} \int_0^{\infty} \sigma_{amp}^{-1} \cdot p_a(\sigma_{amp}) d\sigma_{amp}, \tag{13}$$

where $p_a(\sigma_{amp})$ denotes the probability density function of the peak stress amplitudes, which for a broadband general case follow a Rice distribution (Rice, 1945), and V_p is the peak frequency,

$$V_p = \sqrt{\frac{m_4}{m_2}}. \tag{14}$$

The solution of Eq. (13) for a narrowband process is exact due to the Rice distribution simplifies to the Rayleigh distribution and the peak distribution matches the cycle distribution. In such cases the spectral damage formulated by Bendat (Bendat and Piersol, 2000) can be obtained as

$$\widehat{D}_{NB} = V_0^+ \cdot C^{-1} \left(\sqrt{2m_0}\right)^k \Gamma\left(1 + \frac{k}{2}\right), \tag{15}$$

where $\Gamma(\cdot)$ is the Euler gamma function and V_0^+ is the positive slope zero crossing (Newland, 2012):

$$V_0^+ = \sqrt{\frac{m_2}{m_0}}. \tag{16}$$

- Spectral methods for a broadband random process.

For broadband processes the solution of Eq. (13) can only be achieved in an approximate form (Zorman et al., 2023). The methods used in this work include Wirching-Light (Wirsching and Light, 1980), Tovo-Benasciutti (Tovo, 2002) and Dirlik (1985). The first two methods apply a correction factor (ρ) to the narrowband damage:

$$\widehat{D}_{method} = \rho_{method} \cdot \widehat{D}_{NB} \tag{17}$$

where $\rho_{method} = \rho_{WL}$ or ρ_{TB} depends on the spectral method. In the

former, Wirsching and Light developed an empirically correction factor based on Monte Carlo simulations:

$$\rho_{WL} = a(k) + (1 - a(k)) \cdot (1 - \varepsilon)^{b(k)}, \tag{18}$$

with:

$$a(k) = 0.926 - 0.033k, \tag{19}$$

and

$$b(k) = 1.587k - 2.323. \tag{20}$$

The correction factor ρ_{WL} depends on the parameters of the Whöler material curve C and k, and the spectral width parameter ε. The best fit to the results obtained with the RFC algorithm is achieved with values of the fatigue-strength exponent (k) between 3 and 6.

The method proposed by Tovo-Benasciutti assumes the damage of the RFC algorithm D_{RFC} is always limited between the range counting method D_{RC} and the narrowband method D_{NB} (Larsen and Irvine, 2015), i.e. $D_{RC} \leq D_{RFC} \leq D_{NB}$. The correction factor takes the following form:

$$\rho_{TB} = b + (1 - b)\alpha_2^{k-1}, \tag{21}$$

where the coefficient b can be estimated in three different manners (Benasciutti and Tovo, 2005, 2006; Tovo, 2002).

Rather than using a correction factor for the narrowband process, the Dirlik method assumes a predefined probability density function of the stress-cycle amplitudes obtained with the RFC algorithm. Dirlik introduced a practical closed-form formula that combines one exponential and two Rayleigh probability density functions,

$$p_{a-DK}(\sigma_{amp}) = \frac{1}{\sqrt{m_0}} \left(\frac{G_1}{Q} e^{\frac{-Z}{Q}} + \frac{G_2 \cdot Z}{R^2} e^{\frac{-Z^2}{2R^2}} + G_3 \cdot Z \cdot e^{\frac{-Z^2}{2}} \right), \tag{22}$$

where:

$$Z = \sigma_{amp} \cdot m_0^{-\frac{1}{2}} \tag{23}$$

denotes the normalized amplitude, and parameters G_1, G_2, G_3, R and Q are defined in (Dirlik and Benasciutti, 2021). An alternative definition of the spectral damage rate $\widehat{D}_{DK}$ is:

$$\widehat{D}_{Dk} = V_p \cdot C^{-1} \cdot m_0^{k/2} \left[G_1 \cdot Q^k \cdot \Gamma(1+k) + \left(\sqrt{2}\right)^k \Gamma(1+k) \left(G_2 |R|^k + G_3 \right) \right]. \tag{24}$$

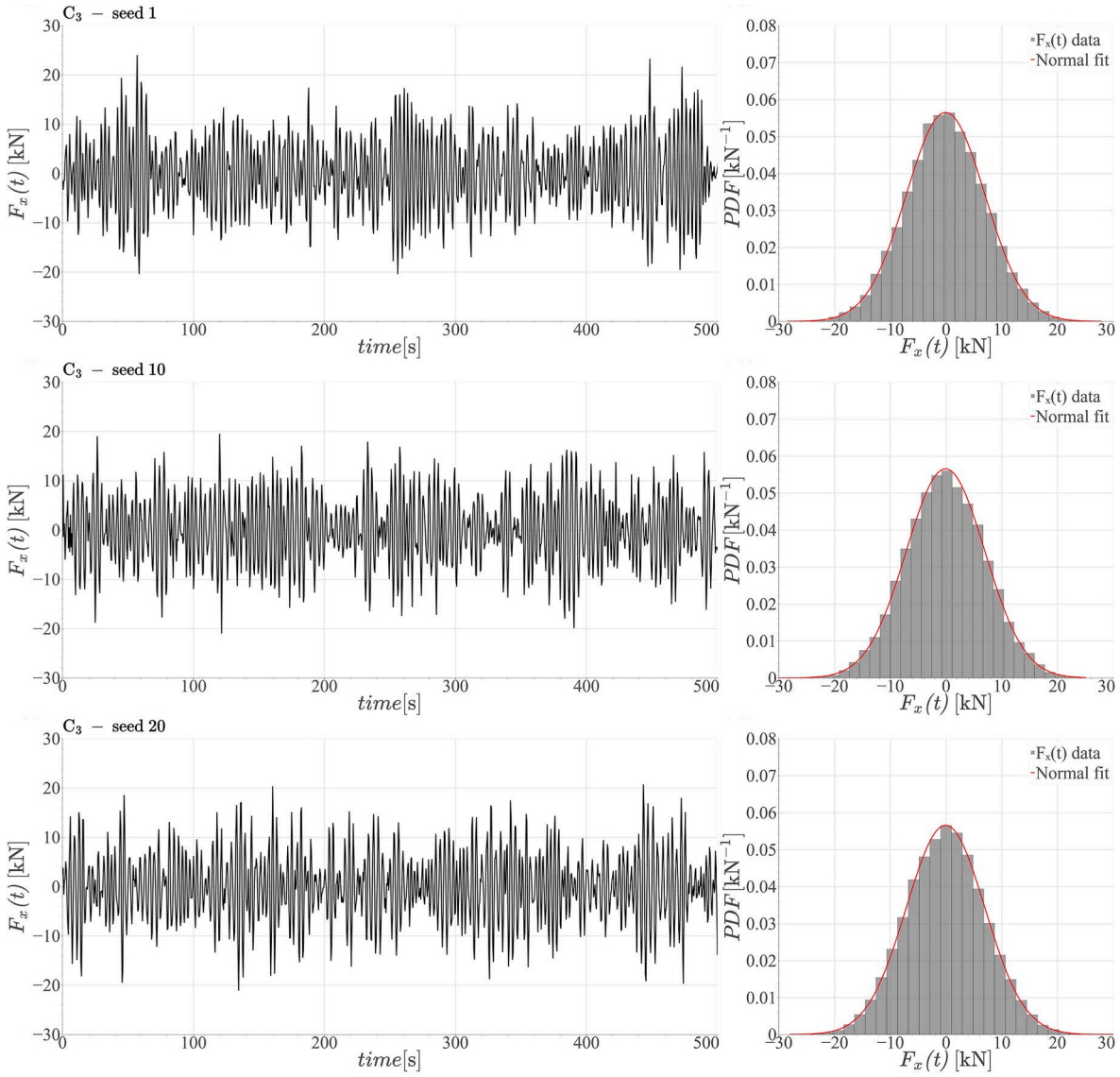

Fig. 7. Extract from the first 500 s of axial force time histories $F_x(t)$ obtained with different seeds for connection no 3 (C_3) and their corresponding histograms with a Gaussian distribution fitted.

3. Results and discussion

3.1. Time domain approach

Initially, the array of floating pontoons was simulated under a 3-h sea state with a significant wave height of $H_s = 0.25$ m, a peak wave period of $T_p = 3$ s and a wave heading of $\theta = 60$ deg (sea state 20 in Table 1). A total of 20 random phase realizations were conducted. The raw data obtained from simulations consists of time histories of axial force, denoted as $F_x(t)$. An illustrative set of connection C_3 series is depicted in Fig. 7, together with their respective load distribution histograms. After obtaining the axial force on each connection, the stress time histories $\sigma(t)$ on the stranded wire ropes were achieved according to (2) and the RFC algorithm and the Palmgren-Miner model were applied to assess the fatigue damage (as detailed in section 2.3.2) and obtain the average damage for all random-phase realizations. Note that this fatigue analysis was conducted using generic sea states from a short-term perspective. To assess the fatigue damage of the structure under local environmental conditions, a long-term analysis considering the probability of occurrence of sea states would be required.

An example of RFC histograms is depicted in Fig. 8, illustrating the mean stress (σ_m) and the stress ranges ($\Delta\sigma$) plotted against the number of cycles. The histogram patterns exhibit similarity across all connections in the array. Stress cycles are concentrated within the range $\Delta\sigma = 20$ and 60 MPa for a mean stress (σ_m) close to zero. Additionally, a high number of cycles with low stress range (below $\Delta\sigma = 10$ MPa) are observed for a broader range of mean stresses.

After completing the stress cycle count, the fatigue damage assessment was carried out by combining the Palmgren-Miner's rule and the S-N curves shown in Fig. 6. Table 2 presents the results for three levels of pre-stress force applied to the wire ropes, F_m = [100, 200 and 300] kN. The averaged damage for the 20 pseudo-random phase realizations ($\overline{D}_{RFC}$) is presented along with the standard deviation.

For all the pre-stress levels considered, the fatigue damage significantly influenced by the position of the connection in the array. The damage in the intermediate connections (C_3 to C_6 in in Fig. 3) is much higher than in the extreme connections (C_1, C_2, C_7 and C_8). For instance, at a pre-stress level of 300 kN, the damage is more than double for C_1 than for C_3, with $\overline{D}_{RFC} = 7.7{\cdot}10^{-5}$ and $18.9{\cdot}10^{-5}$, respectively.

Concerning the influence of the relative position of the connections with the incoming wave direction, the connections to the right of the array (C_5 to C_8 in Fig. 3) experience higher damage compared to their opposing connections (C_1 to C_4). This difference is more pronounced for extreme connections. For instance, the damage under 300 kN of pre-stress is $\overline{D}_{RFC} = 7.7{\cdot}10^{-5}$ in C_1, while it doubles to $\overline{D}_{RFC} = 15.7\ 10^{-5}$ in C_8.

There are no substantial differences in the damage level between seaward connections and their leeward counterparts, except for the pair C_1 and C_2. In this case, the wire ropes in the leeward connection C_2 experience significantly higher damage, with $\overline{D}_{RFC} = 4.3{\cdot}10^{-5}$,

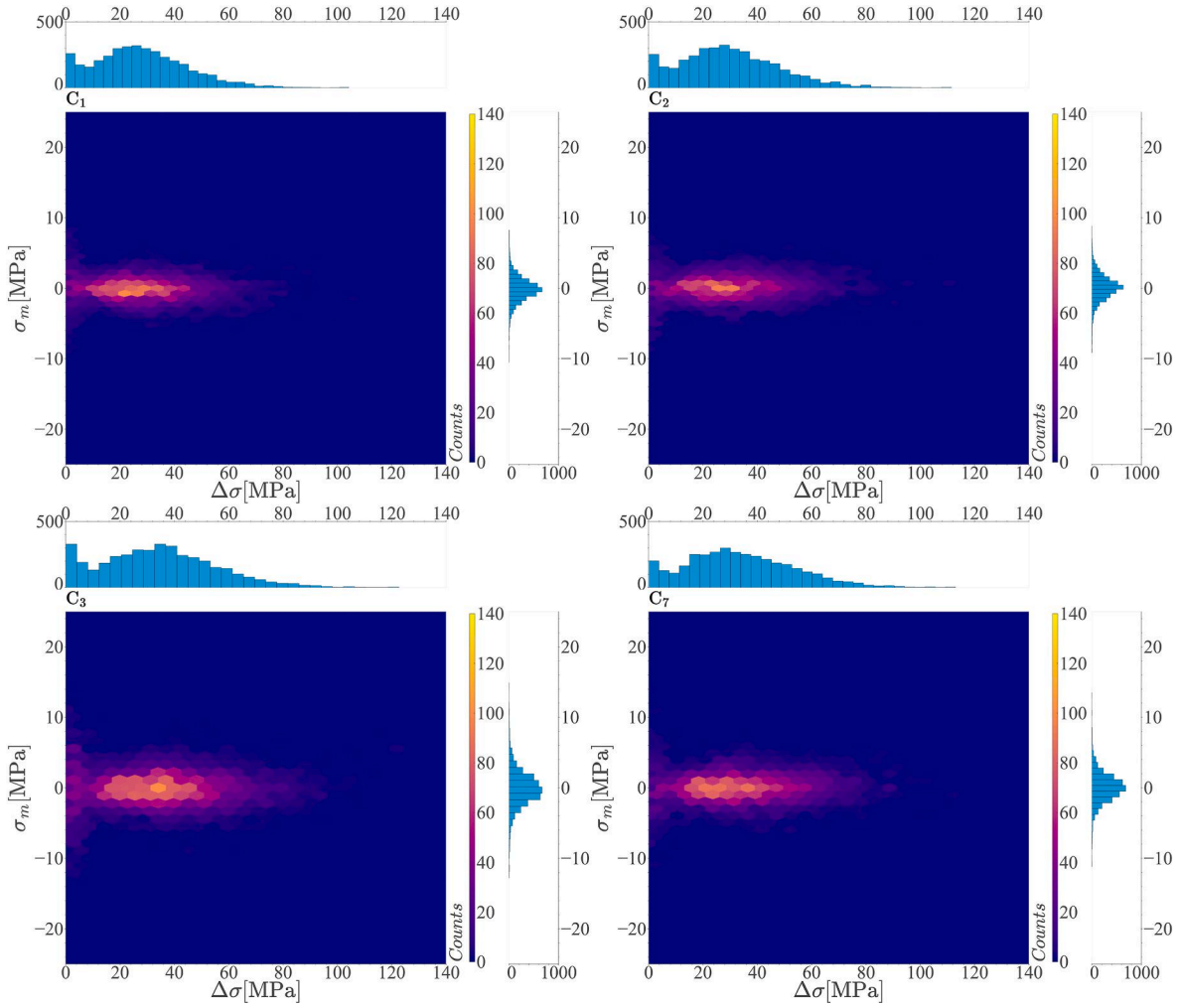

Fig. 8. Stress cycle histograms obtained with RFC for connections C_1 (upper left panel), C_2 (upper rigth panel), C_3 (lower left panel) and C_7 (lower rigth panel). Simulation parameters: $H_s = 0.25$ m, $T_p = 3$ s and $\theta = 60$ deg, seed no. 7.

Table 2
Fatigue damage $\overline{D}_{RFC}$ on the stranded wire ropes for all the connections in the array and three different levels of pre-stress force F_m. Results obtained with the RFC algorithm and the Palmgren-Miner method for 20 random phase realizations. Average values and standard deviation (*std*) are presented.

Connection	$F_m = 100$ [kN]		$F_m = 200$ [kN]		$F_m = 300$ [kN]	
	$\overline{D}_{RFC}\cdot10^{-5}$	$std\cdot10^{-7}$	$\overline{D}_{RFC}\cdot10^{-5}$	$std\cdot10^{-7}$	$\overline{D}_{RFC}\cdot10^{-5}$	$std\cdot10^{-7}$
C_1	3.3	5.1	4.7	7.1	7.7	11.9
C_2	4.3	6.4	6.0	8.9	10.0	14.8
C_3	8.1	18.1	11.4	25.4	18.9	42.3
C_4	8.0	17.7	11.2	24.7	18.7	41.2
C_5	10.6	25.5	14.9	35.7	27.7	59.5
C_6	10.6	24.5	14.9	34.3	27.7	57.2
C_7	6.7	13.4	9.4	18.8	15.6	31.4
C_8	6.7	14.1	9.4	19.7	15.7	32.9

compared to the $3.3\cdot10^{-5}$ obtained for the leeward connection C_1.

Overall, the wire ropes most affected by fatigue are those in the connections C_5 and C_6, which correspond to the intermediate seaward and leeward connections on the right side of the array (Fig. 3). In both cases, the damage level reaches an average value of $27.7\cdot10^{-5}$ when a pre-stress force of 300 kN is applied. On the contrary, the ropes experiencing lower fatigue damage are in the extreme connections to the left of the array C_1 and C_2. Unexpectedly, these connections link the first and second modules in the array to encounter waves.

As for the influence of the pre-stress force applied to the wire ropes, there is a clear impact on the fatigue damage of these elements. As expected, increasing the pre-stress force results in higher damage. For all connections in the array, when the stranded ropes are pre-stressed with 300 kN, the damage doubles compared to a pre-stress level of 100 kN.

3.2. Frequency domain approach

The fatigue damage estimates obtained through the time domain approach were compared to those obtained using the spectral methods described in section 2.3.3. The frequency domain approach was applied to the same stress time histories as in previous section corresponding to the 20 random wave phase realizations of a sea state 20 in Table 1.

3.2.1. Stress power spectral density

As an example of the results, the stress power spectral density $S_\sigma(f)$ for the four seaward connections and a given random phase realization are presented in Fig. 9. The stress spectra reveal two well-differentiated peaks around 0.26 and 0.34 Hz. While the second peak corresponds to the peak wave period of the incoming waves ($T_p = 3$ s), the first may be related to one of the natural frequencies of the floating pontoon array. The same applies to the rest of the connections and simulation realizations. However, the peaks are more apparent for the intermediate connections C_3 and C_5. For these, the zeroth spectral moment, which is related to the total energy contained in the spectrum, reaches values above $m_0 = 240$ MPa^2 (see values for C_3 to C_5 in Table 3). In contrast, the values decrease below $m_0 = 222$ MPa^2 for the extreme connections (C_1, C_2, C_7 and C_8). These higher stress levels agree with the results obtained in the time domain approach for intermediate connections, which are subjected to a higher fatigue damage.

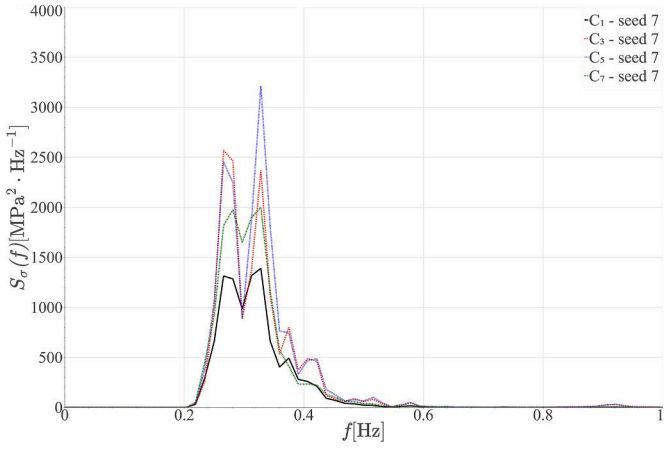

Fig. 9. Stress power sprectral density for connections C_1, C_3, C_5 and C_7. Simulation parameters: $H_s = 0.25$ m, $T_p = 3$ s and $\theta = 60$ deg.

The average spectral parameters obtained for the stress spectra of the 20 realizations are summarized in Table 3, which also includes the equivalent parameters for the incident wave spectrum. The results reveal that the stress spectra obtained for all connections in the array are narrower than the Pierson-Moskowitz wave spectrum used for the simulations. In both spectra, the bandwidth parameters α_i approach unity. This finding suggest that those methods based on the narrow band correction factor may be valid for the spectral damage calculations.

Similar to the precedent table, Table 4 shows the results related to the Gaussianity test of Shapiro-Wilk. The p-values found are consistently above the significance level (5%) on all connections, varying between 19.9% and 58.7%. These results confirm the Gaussian character of the input signals used for the subsequent fatigue analysis. The next section deals with the application of the spectral methods for the calculation of the fatigue damage.

3.2.2. Spectral damage

Three spectral methods were implemented to obtain the fatigue damage: Dirlik, Tovo-Benasciutti and Wirsching Light methods (detailed in section 2.3.3). The results are summarized in Table 5. In general, these methods yielded fatigue damages higher than those obtained through the RFC algorithm, indicating their more conservative nature.

Among the three methods, the Wirsching-Light method exhibited the best fit to the RFC results, with relative errors ranging from 0.2 to 1.8% depending on the connection. The Dirlik and Tovo-Benasciutti methods presented much higher relative errors, with values above 16% for all connections in the array. Based on these results, the Wirsching-Light

Table 3
Average values of bandwidth spectral parameters for floating breakwater connections and for the incident Pierson-Moskowitz wave spectrum, $S_w(f)$ ($H_s = 0.25$ m, $T_p = 3$ s, $\theta = 60$ deg and duration of 3 h).

Connection/wave spectrum	Spectral Parameter				
	m_0	α_1	α_2	ε	ε_v
C_1	155.29 [MPa^2]	0.98	0.89	0.46	0.19
C_2	177.15 [MPa^2]	0.98	0.89	0.45	0.19
C_3	242.95 [MPa^2]	0.97	0.81	0.59	0.25
C_4	241.22 [MPa^2]	0.97	0.80	0.59	0.25
C_5	277.23 [MPa^2]	0.97	0.82	0.57	0.24
C_6	277.83 [MPa^2]	0.97	0.82	0.57	0.24
C_7	221.73 [MPa^2]	0.98	0.90	0.44	0.19
C_8	221.96 [MPa^2]	0.98	0.90	0.43	0.18
$S_w(f)$	$3.85\cdot10^{-3}$ [m^2]	0.95	0.81	0.58	0.30

Table 4
Average p-value between 20 seeds obtained with the Saphiro-Wilk test.

Connection	*Saphiro-Wilk p-value* [%]
C_1	54.8
C_2	58.7
C_3	26.5
C_4	27.3
C_5	23.2
C_6	19.9
C_7	34.7
C_8	25.4

method is identified as the most suitable spectral method for determining fatigue damage in the stranded ropes of the connections.

Fig. 10 shows the damage in the stranded ropes of the connections within the array for three different pre-stress levels: 100, 200 and 300 kN. The average values for the 20 pseudo-random phase realizations are presented. The trends observed in section 3.1 on how the position of the connection and the pre-stress level influence the fatigue damage to the stranded rope are reaffirmed. The fatigue damage grows in the intermediate connections with respect to extreme ones, and in connections to the right side of the array with respect to left side connections. The differences between seaward and leeward connections are negligible. The stress level is confirmed to largely influence the fatigue damage. These observations remain consistent regardless of the spectral method applied.

3.3. Influence of the sea state on the fatigue damage

The fatigue damage to the wire ropes across array connections was assessed for different sea states to analyse the impact of sea state duration and wave parameters on the results.

3.3.1. Duration of the sea state

The impacts of simulating short-duration sea-states (30 min) were compared with those of typical long-duration (3 h) sea states. Table 5 presents the averaged damage for 20 random phase realizations of sea state 20 (see Table 1) and considering a pre-stress level on the stranded ropes of $F_m = 100$ kN. The damage assessment was conducted using the time domain approach based on the RFC algorithm and the Palmgren-Miner rule, and the frequency domain approach that applied the Wirsching Light method (it was demonstrated as the most accurate spectral method in previous section 3.2.2). The values of damage are presented for a 3-h sea state to allow comparison. Accordingly, the damage results for the short-duration sea states were extrapolated by simply multiplying the damage obtained for 30 min by six (the ratio of 30 min to 3 h).

The maximum differences obtained in the predicted fatigue damage using short- and long-duration sea states were 1.5% and 0.2% for the time domain and frequency domain approaches, respectively. Fig. 11 shows the stress spectra obtained from stress time histories with both durations. As observed, the differences are negligible and confirm the stationarity of the stress time history. The same pattern was observed for the rest of connections and other realizations of the same sea state. This result underscores that short-duration simulations (30 min) combined with spectral method stands out as a robust choice for estimating the fatigue damage on the stranded wire ropes.

3.3.2. Wave parameters

The fatigue damage was analysed for 27 sea states defined by combining H_s = [0.05, 0.15 and 0.25] m, T_p = [3, 4.5, and 6] s and θ = [45, 60 and 90] deg (Table 1). Considering the 20 random phase repetitions per sea state, this resulted in a total of 540 simulations. To reduce the computational times, 30-min sea states were simulated.

Fig. 12 presents the average fatigue damage for each sea state at four connections of the array. The fatigue damage tends to rise with increasing significant wave height H_S and to a lesser extent, with the peak period T_p. The highest values were observed for $H_s = 0.25$ m and $T_p = 6$ s. Notably, the wave heading direction θ exerts a substantial influence on fatigue damage. The damage increases for oblique wave directions, peaking at $\theta = 60$ deg. Conversely, for transverse wave heading with $\theta = 90$ deg, the damage is minimal, as the axial forces F_x on connections tend to be reduced.

The influence of position in the array on fatigue damage, as discussed in previous sections for a single sea state, holds for all the sea states. Regardless of wave conditions, intermediate connections experience higher fatigue damage than outer connections (compare C_1 and C_3 in Fig. 12). Furthermore, the position in the array relative to the direction of incoming waves is evident, the stranded ropes to the left side (i.e., those linking the first modules in the direction of incoming waves, Fig. 3) of the array are subjected to lower fatigue damage (compare C_1 and C_7).

Table 5
Fatigue damage on pontoon connections estimated through the RFC (long and short simulations), Dirlik, Tovo-Bensasciutti, Wirschling-Light (long and short simulations) and stress transfer functions $\boldsymbol{H_\sigma^2(f)}$ methods. The results accounts for a pre-stress of 100 kN.

Connection	Sea State Duration	Fatigue method						$H_\sigma^2(f)$
		RFC	RFC	Dirlik	Tovo-Benasciutti	Wirsching Light	Wirsching Light	
		3 h	30 min	3 h	3 h	3 h	30 min	30 min
C_1	$\overline{D}\cdot10^{-5}$	3.3	3.3	4.0	4.0	3.3	3.3	3.3
	error [%]	0.0	1.1	16.8	16.3	0.2	0.1	0.0
C_2	$\overline{D}\cdot10^{-5}$	4.3	4.2	5.1	5.1	4.3	4.3	4.5
	error [%]	0.0	1.1	16.5	16.1	0.5	0.3	4.4
C_3	$\overline{D}\cdot10^{-5}$	8.1	8.0	10.0	9.9	8.3	8.3	8.7
	error [%]	0.0	0.6	18.9	17.9	1.7	1.8	6.9
C_4	$\overline{D}\cdot10^{-5}$	8.0	8.0	9.9	9.8	8.2	8.2	8.7
	error [%]	0.0	0.7	19.0	18.0	1.8	1.9	8.0
C_5	$\overline{D}\cdot10^{-5}$	10.6	10.5	13.1	13.0	10.8	10.8	11.3
	error [%]	0.0	0.9	19.0	18.2	1.8	2.0	6.2
C_6	$\overline{D}\cdot10^{-5}$	10.6	10.5	13.1	13.0	10.8	10.8	11.4
	error [%]	0.0	0.9	19.1	18.2	1.8	2.0	7.0
C_7	$\overline{D}\cdot10^{-5}$	6.7	6.6	8.0	8.0	6.7	6.7	6.8
	error [%]	0.0	1.3	16.6	16.3	0.2	0.2	1.5
C_8	$\overline{D}\cdot10^{-5}$	6.7	6.6	8.1	8.0	6.7	6.7	7.0
	error [%]	0.0	1.5	16.5	16.2	0.3	0.3	4.3

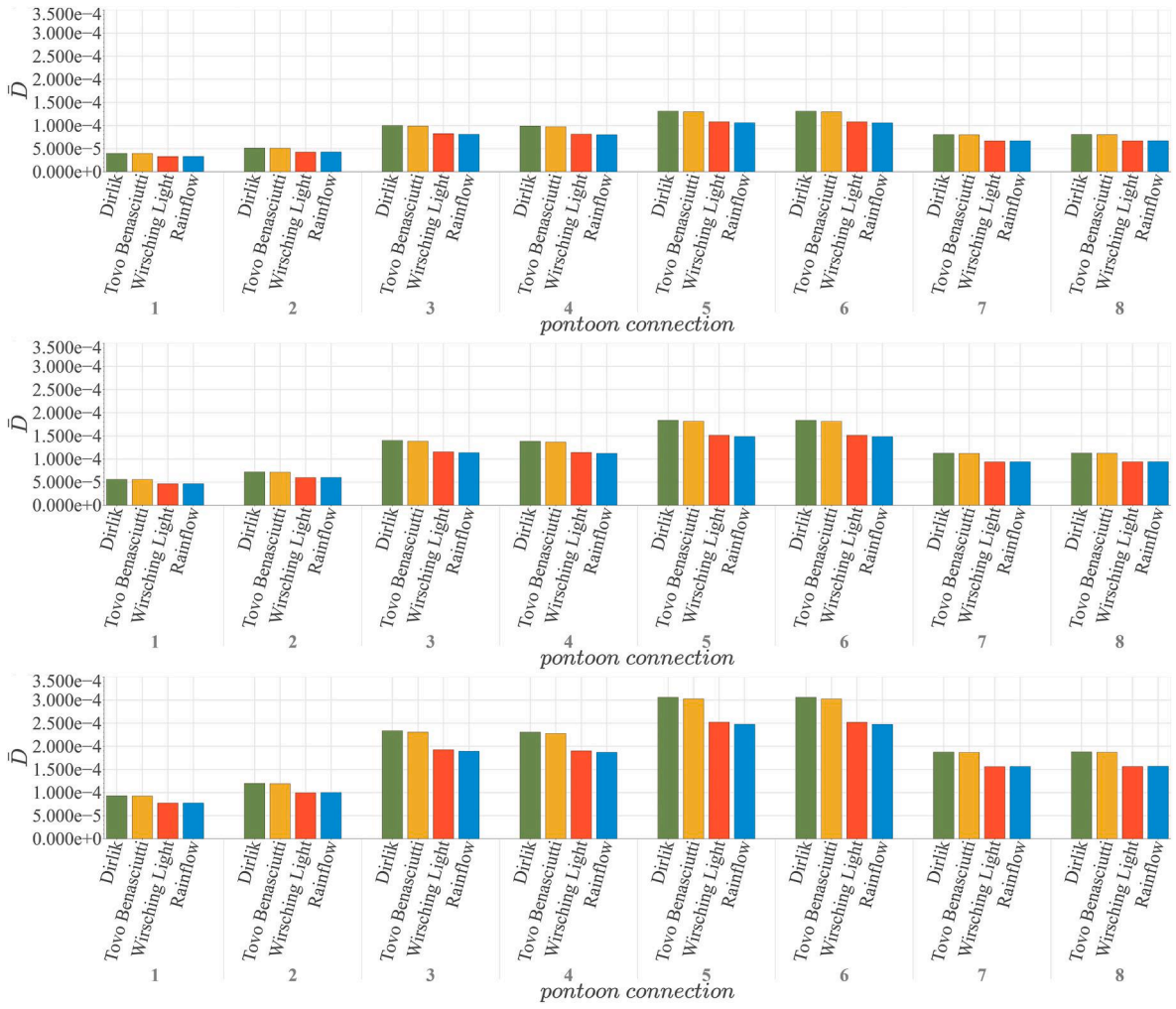

Fig. 10. Fatigue damage $\overline{D}$ estimated for all connections with different pre-stress force F_m levels. Upper panel, mid panel and lower panel accounts for $F_m = 100$, 200 and 300 kN, respectively.

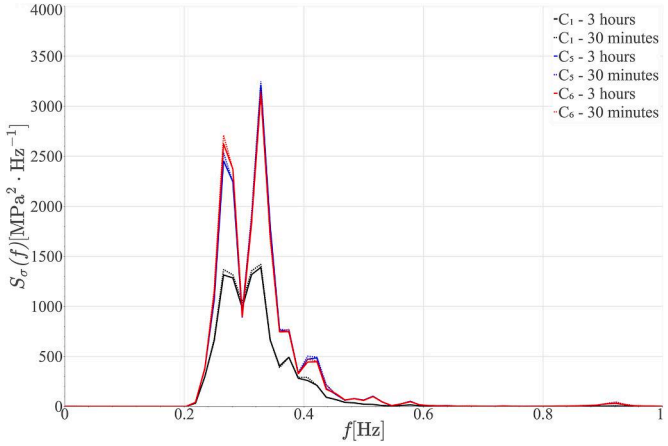

Fig. 11. Stress spectra for long-duration sea-states (3 h) and for short-duration sea states (30 min). The results correspond to the seed number 7 and connections C_1, C_5 and C_6 Wave parameters: $H_s = 0.25$ m, $T_p = 3$ s and $\theta = 60$ deg.

3.4. Influence of the wave parameters on the stress transfer functions $H_\sigma^2(f)$

The stress spectra on the ropes were obtained for different sea states using the Pierson-Moskowitz spectrum, and the corresponding stress transfer function, $H_\sigma^2(f)$, was derived with Eq. (6). As observed in Fig. 13, the stress response strongly depends on the wave heading direction θ and the specific connection considered, whereas the influence of significant wave height and the peak wave period on the results is not significant. This suggests that each connection within the array has a characteristic transfer function per wave heading direction.

However, due to the narrow power distribution of the Pierson-Moskowitz spectral model around the peak period, the results are not well defined towards the sides of the spectrum. To establish a characteristic stress transfer function across the entire wave frequency range, it would be necessary to combine the results obtained from simulating several peak periods.

On these grounds, the stress transfer functions were obtained with a white noise spectrum with equivalent spectral power to a Pierson-Moskowitz one. For example, for $H_s = 0.25$ m, a constant value of $S_w(f) = 3.9{\cdot}10^{-3}$ MPa^2 Hz^{-1} was applied to the white spectrum according to Eq. (6). In this case, the stress response is well-defined across the wave frequency with only the results of a unique simulation (Fig. 13).

Once the characteristic $H_\sigma^2(f)$ for a given connection and wave heading is defined, the stress spectrum for any wave spectrum can be determined by simply applying Eq. (6), eliminating the need to simulate the sea state and obtain the stress history. As an example, Fig. 14 shows the stress spectrum at C_5 for sea state 20 (see Table 1). It is evident that

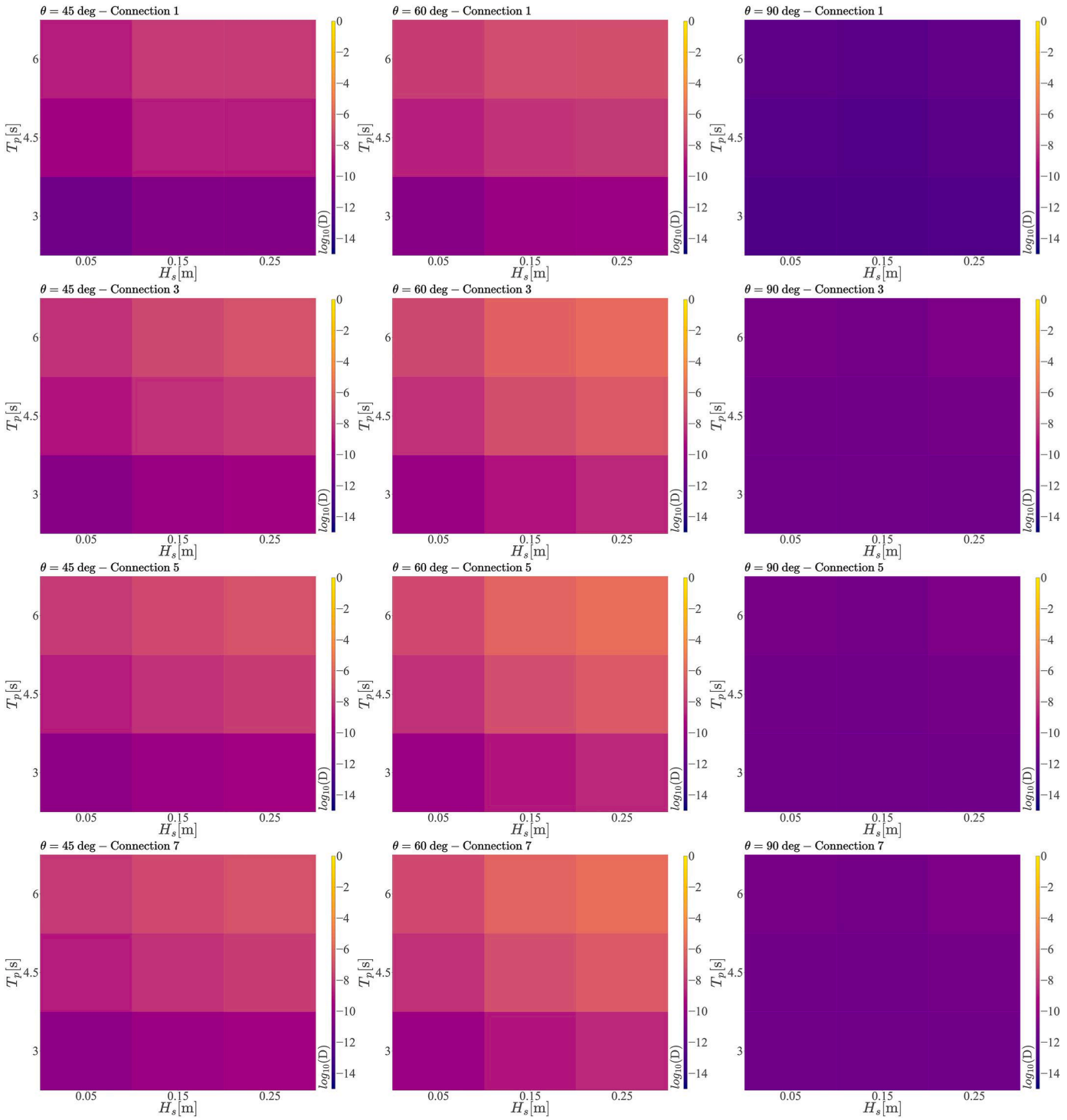

Fig. 12. Average fatigue damage obtained with the Rainflow counting method for different sea states and connections. The damage is plotted using the base 10 logarithm for a better visualization of the results.

the results obtained directly from the simulation of the sea state differ little from the results obtained with the characteristic $H_\sigma^2(f)$ and, therefore, comparable results on fatigue damage estimation are anticipated.

Fig. 15 shows the stress transfer functions $H_\sigma^2(f)$ obtained with a white noise spectrum for various combinations of wave headings and floating breakwater connections. The results confirm that the wave heading is a crucial parameter influencing the stress response at each connection. As expected from previous results, the response is highest for oblique waves with $\theta = 60$ deg, followed by $\theta = 45$ and 90 deg. For the latter, the response is almost negligible.

The role of the position of the connection in the array is confirmed. On a first note, a substantial difference between intermediate and extreme connections is found around 0.1–0.5 Hz. The peak values for intermediate connections reach around $9{\cdot}10^5$ MPa^2 m^{-2} at 0.2 Hz, while extreme connections only reach nearly half of that value. Therefore, higher amplitudes on stress spectra are expected on intermediate connections. On another note, similar patterns are also observed between opposite extreme connections (e.g., C_1 vs. C_7) or intermediate

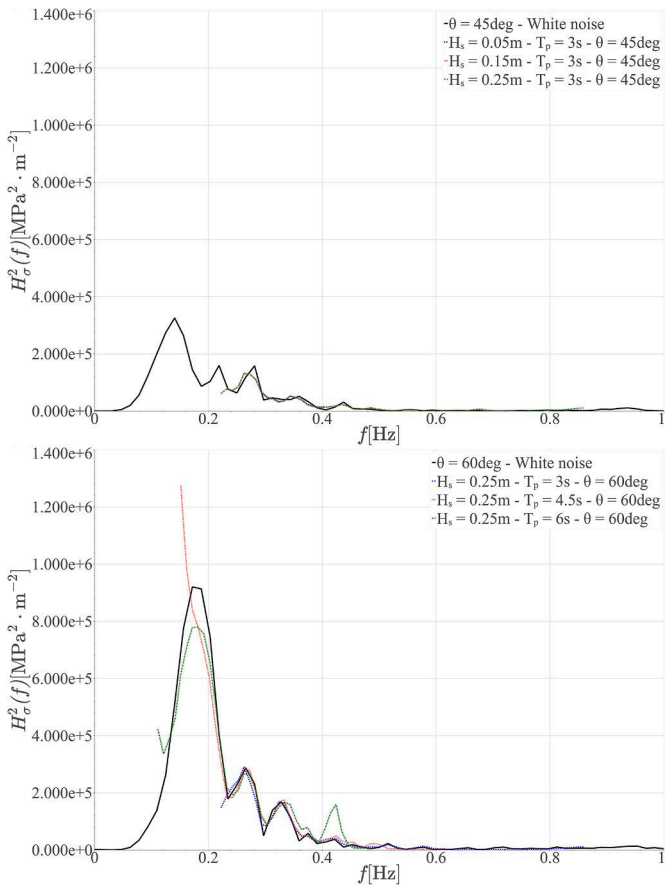

Fig. 13. Comparison between $\boldsymbol{H_\sigma^2(f)}$ on connection C_5 estimated with Pierson-Moskowitz and white noise wave spectra for a wave heading of $\theta = 45$ deg (left panel) and $\theta = 60$ deg (right panel).

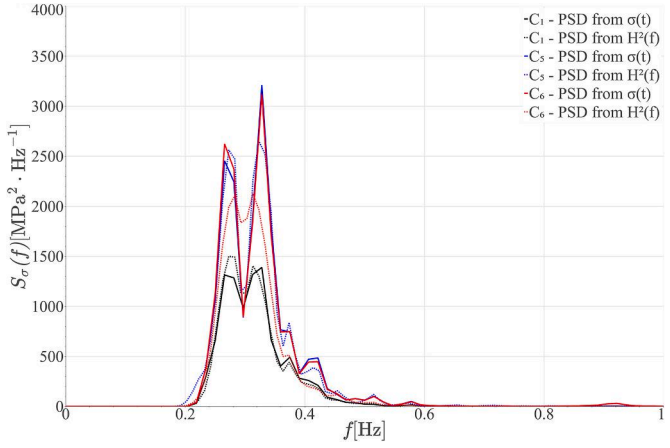

Fig. 14. Stress power spectral density $S_\sigma(f)$ at connections C_1, C_5 and C_6 estimated with stress time histories $\sigma(t)$ and stress transfer functions $\boldsymbol{H_\sigma^2(f)}$. Parameters of the wave spectrum: $H_s = 0.25$ m, $T_p = 3$ s, $\theta = 60$ deg. Sea state duration of 30 min.

connections (e.g., C_3 vs. C_5). Moreover, nearly identical function shapes are exhibited by connections seaward and leeward (e.g., C_1 and C_2).

3.5. Fatigue damage from stress transfer functions

Finally, a proposed procedure to assess the fatigue damage on the stranded wire ropes that aims to save computational costs was analysed (Fig. 16). First, a white noise wave spectrum was simulated for three different wave headings $\theta = [45, 60 \text{ and } 90]$ deg and considering a 30-min sea state. The total power of the spectrum was set to a constant value of $S_w(f) = 3.9{\cdot}10^{-3}$ MPa^2 Hz^{-1} equivalent to $H_s = 0.25$ m according to Eq. (4). Subsequently, a characteristic function $H_\sigma^2(f)$ per wave heading direction θ was obtained for each connection in the array, as presented in previous section.

The stress spectrum $S_\sigma(f)$ on a stranded rope of a connection under a given sea state characterized with a Pierson-Moskowitz spectrum (defined in terms of H_s and T_p) and the corresponding wave heading direction θ, was obtained by applying a specific $H_\sigma^2(f)$ depending on the heading direction. The Wirsching-Light method was then applied to assess fatigue damage.

The estimated damage derived was compared to the damage obtained applying the RFC algorithm to the results of simulating each 3-h sea state. Table 5 compares both approaches. The results demonstrate an effective performance of the proposed methodology, since the relative error recorded are consistently below 10% across all connections. Major deviations in relative error are observed within intermediate connections, with errors between 6 and 8%. Nevertheless, the error in extreme connections decrease below 4%. In fact, the fatigue damage prediction for connection C_1 matches the RFC values with a relative error close to 0%.

3.6. Computational cost analysis

Finally, a comparison was made among different fatigue assessment approaches in terms of simulation times. All simulations were performed on a computer equipped with the AMD Ryzen™ 9 3950X processor (32 logic CPU cores). The results are summarized in Table 6.

On average, 22 h were required to simulate each 3-h sea state defined with the Pierson-Moskowitz spectrum. Therefore, to complete 20 random phase repetitions of a given sea state, a total of 440 h were consumed. Shortening the sea state duration to 30 min resulted in a reduction in computational time from 22 to 6 h per realization. Therefore, estimating the fatigue damage for 27 short-duration sea states with different H_s, T_p and θ in section 3.3 required a total of 3240 h.

On another note, the simulation of a 3-h sea state characterized with a white noise spectrum required an average of 7 hours each. With the proposed methodology based on the utilization of characteristic $H_\sigma^2(f)$ per connection and wave heading direction, only three simulations were required to characterize the fatigue damage for the 27 sea states mentioned earlier. This results in a reduction in computational time from 3240 to just 21 h.

It is evident that the advantage of the proposed methodology for fatigue damage assessment is that the number of simulations only rely on the number of wave headings of interest (the functions are independent of significant wave height and peak period). In engineering practice, the computational savings for fatigue life assessment are much higher. For example, considering a site-specific wave scatter diagram with a discretization in 16 ranges of H_s, 12 ranges of T_p and 6 ranges of θ, results in 1152 different sea states. A complete fatigue life assessment of the wire ropes in the connections with the RFC method and 3-h sea states would result in about half a million hour of computation time (with the referred computer). However, with the proposed approach, this would be reduced to 42 h (Table 6).

4. Conclusions

In this study, a fatigue damage assessment for stranded wire ropes in a floating pontoon array was conducted employing both time and frequency domain approaches. Additionally, a methodology based on stress transfer functions obtained with a white noise wave spectrum is introduced and compared to the traditional approach. The key findings and conclusions are summarized hereinafter.

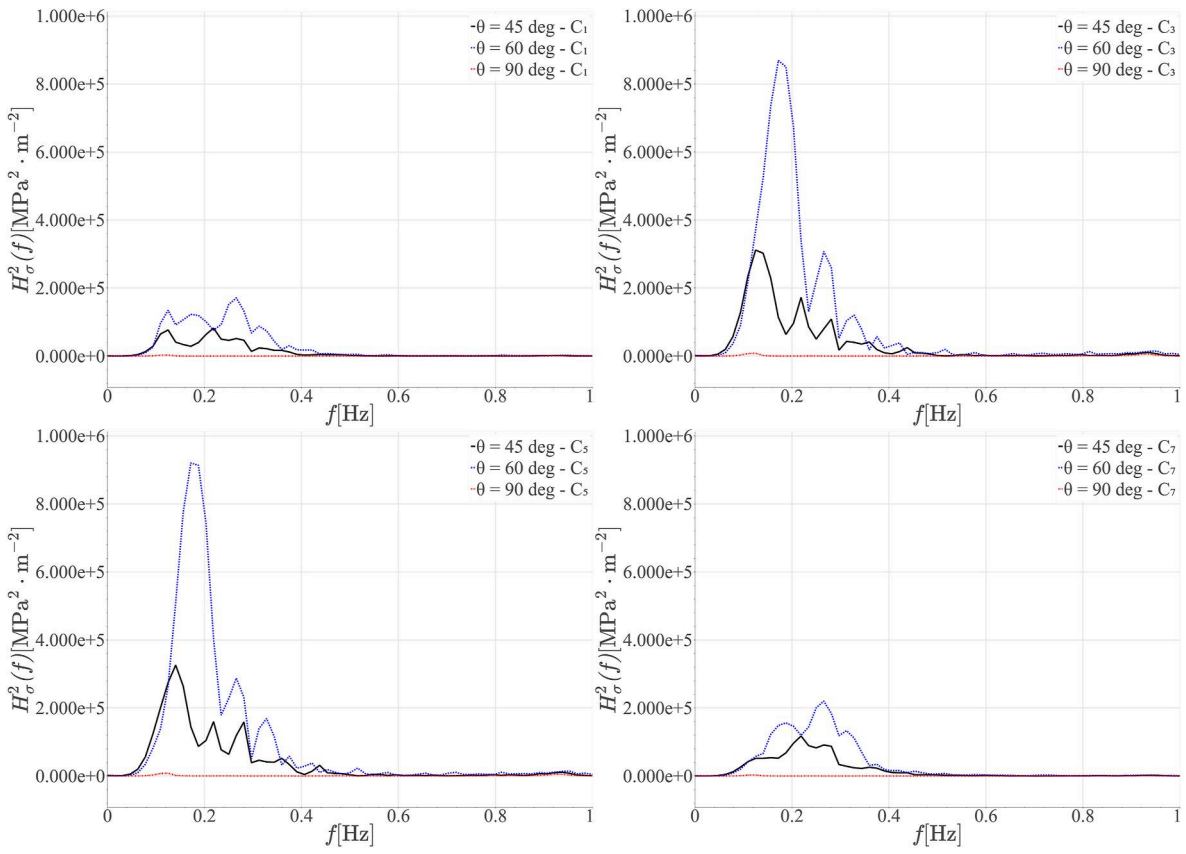

Fig. 15. Stress transfer functions for different wave headings and floating breakwater connections obtained through the white noise spectrum with $S_w(f) = 3.9{\cdot}10^{-3}$ $\mathrm{MPa}^2\ \mathrm{Hz}^{-1}$.

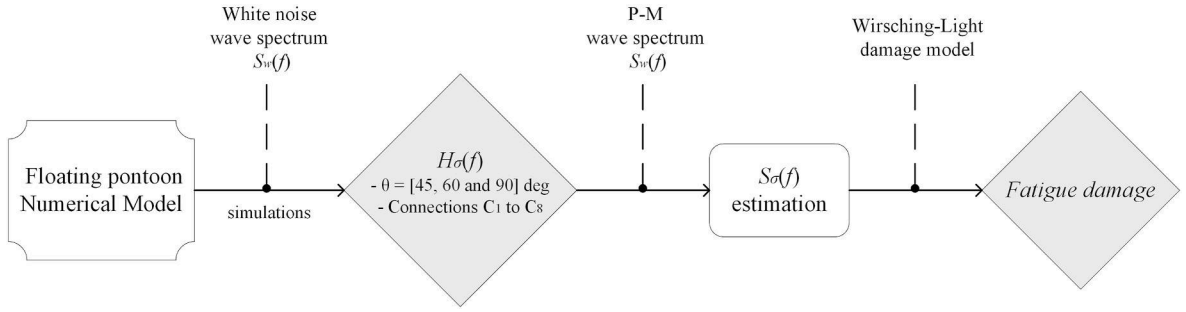

Fig. 16. Scheme procedure to achieve the stress transfer functions and apply them.

Table 6
Estimated computational cost of different approaches for assessing the fatigue damage considering a typical wave scatter diagram with a discretization of 16 × 12 × 6 = 1,152 sea states (H_s, T_p and θ).

Approach	Sea state duration [h]	no. of sea states	Computational time per repetition [h]	no. of repetitions	Total computational time [h]
Long sea states + RFC	3.0	1152	22	20	506,880 h
Short sea states + RFC	0.5	1152	6	20	138,240 h
Short sea state + stress $H_\sigma^2(f)$	0.5	6	7	1	42 h

A time domain approach utilizing the RFC algorithm and Palmgren-Miner model was initially employed to assess the fatigue damage. The results showed that the position of connections in the array strongly influences the fatigue damage, with intermediate connections experiencing significantly higher damage than extreme connections. The relative position of connections to the incoming wave direction also plays a crucial role. However, minimal damage differences were found between seaward and leeward connection pairs (*e.g.* C_1 and C_2). The results pre-stress force on the stranded ropes is also paramount and, as expected, an increased pre-stress force leads to higher damage across all connections. On another note, short-duration sea state simulations (30 min) proved to be a robust choice for estimating fatigue damage, with negligible differences compared to long-duration sea states (3 h).

Spectral methods, including Dirlik, Tovo-Benasciutti, and Wirsching-Light, were also employed for fatigue damage estimation, and their results were compared with the RFC algorithm. All spectral methods

generally yielded higher fatigue damage estimates, indicating a conservative nature. Among them, the Wirsching-Light method demonstrated the best fit to RFC results with an error around 1%. In contrast, Tovo-Benasciutti and Dirlik methods performed relative errors exceeding 20%.

Fatigue damage was analysed for 27 sea states characterized by their significant wave heights (Hs), peak periods (T_p), and wave heading directions (θ). To achieve this, 20 random phase simulations were conducted for each sea state, totalling 3240 hours of actual computational time. The findings underscore the substantial impact of wave parameters on fatigue damage, revealing high damage levels associated with increased wave height and peak period. Importantly, the pronounced effect on fatigue damage for sea states featuring oblique wave directions is highlighted. The maximum fatigue damage was found for $\theta = 60$ deg, while minimum fatigue damage corresponded to transverse sea states with $\theta = 90$ deg, as expected.

As a novelty, characteristic stress transfer functions $H_\sigma^2(f)$ for each connection and wave heading direction were introduced, offering a simplified approach for fatigue damage assessment. This innovative methodology significantly reduces the number of simulations required and therefore the computational times. It was shown that for assessing the fatigue damage of the 27 sea states considered in this study, the computational time reduced from 3240 h to 21 h with respect to the traditional method. The efficiency and accuracy of the proposed approach is clear, emphasizing its practical applicability and substantial computational savings for fatigue life assessment not only of floating breakwaters, but also other marine structures.

In conclusion, the proposed methodology, leveraging stress transfer functions and spectral methods, offers an efficient and accurate alternative for fatigue damage assessment in floating pontoon arrays, with substantial computational savings in engineering applications. The findings contribute to advancing the understanding of fatigue behaviour in marine structures and offer practical insights for optimizing computational resources in similar analyses.

Future research lines on this topic include the long-term fatigue analysis of the structure for site-specific environmental conditions. Furthermore, it is also recommended to carry out comparison with bench mark studies or experimental tests.

CRediT authorship contribution statement

A.J. Cebada-Relea: Writing – review & editing, Writing – original draft, Visualization, Software, Methodology, Conceptualization. **M. Aenlle:** Writing – review & editing, Writing – original draft, Supervision, Methodology, Funding acquisition, Conceptualization. **M. López:** Writing – review & editing, Visualization, Supervision, Methodology, Conceptualization.

Declaration of competing interest

The authors declare that they have no known competing financial interests or personal relationships that could have appeared to influence the work reported in this paper.

Data availability

Data will be made available on request.

Acknowledgments

A. Cebada was supported by the “Ayudas para realización de Tesis Doctorales. Modalidad A: Contratos de Investigación en régimen de concurrencia competitiva”, a research fellowship programme financed by the University of Oviedo (Spain) [grant number PAPI-22-PF-9]. The authors also would like to express their gratitude to the Spanish Ministry of Science and Innovation for the financial support through the project MCI-20-PID2019-105593 GB-00/AEI/10.13039/501100011033.

Appendix A. Supplementary data

Supplementary data to this article can be found online at https://doi.org/10.1016/j.oceaneng.2024.117317.

References

ANSYS, 2016. ANSYS Aqwa. ANSYS Ltd., Canonsburg, PA, USA.
Benasciutti, D., Tovo, R., 2006. Comparison of Spectral Methods for Fatigue Analysis of Broad-Band Gaussian Random Processes, vol. 21, pp. 287–299. https://doi.org/10.1016/j.probengmech.2005.10.003.
Benasciutti, D., Tovo, R., 2005. Spectral methods for lifetime prediction under wide-band stationary random processes. Int. J. Fatig. 27, 867–877.
Bendat, J.S., Piersol, A.G., 2000. Random data analysis and measurement procedures. Meas. Sci. Technol. 11, 1825–1826.
Ćatipović, I., Ćorak, M., Alujević, N., Parunov, J., 2019. Dynamic analysis of an array of connected floating breakwaters. J. Mar. Sci. Eng. 7 https://doi.org/10.3390/jmse7090298.
Cebada-Relea, A., Menéndez, C., Fernández, P., Soto-Pérez, F., Claus, R., Aenlle, M., López, M., 2022. Revista española de la Fractura. In: Sociedad Española de Integridad Estructural. Diques Flotantes Portuarios: Análisis de Las Conexiones y Sinergias Con La Energía Undimotriz. Coimbra, pp. 199–204.
Cebada-Relea, A.J., López, M., Aenlle, M., 2022. Time-domain numerical modelling of the connector forces in a modular pontoon floating breakwater under regular and irregular oblique waves. Ocean Eng. 243, 110263 https://doi.org/10.1016/j.oceaneng.2021.110263.
Cebada-Relea, A.J., López, M., Claus, R., Aenlle, M., 2023. Short-term analysis of extreme wave-induced forces on the connections of a floating breakwater. Ocean Eng. 280, 114579 https://doi.org/10.1016/j.oceaneng.2023.114579.
Chen, X., Miao, Y., Tang, X., Liu, J., 2017. Numerical and experimental analysis of a moored pontoon under regular wave in water of finite depth. Ships Offshore Struct. 12, 412–423. https://doi.org/10.1080/17445302.2016.1172831.
Dai, J., Wang, C.M., Utsunomiya, T., Duan, W., 2018. Review of recent research and developments on floating breakwaters. Ocean Eng. 158, 132–151. https://doi.org/10.1016/j.oceaneng.2018.03.083.
Dirlik, T., 1985. Application of Computers in Fatigue Analysis. University of Warwick.
Dirlik, T., Benasciutti, D., 2021. Dirlik and Tovo-Benasciutti Spectral Methods in Vibration Fatigue : A Review with a Historical Perspective.
DNV, G.L., 2017. DNVGL-RP-C205: environmental conditions and environmental loads. DNV GL Recomm. Pract. 1–259.
Dowling, N.E., 1971. Fatigue Failure Predictions for Complicated Stress Strain Histories, vol. 337. TAM R.
Gl, D., 2018. DNVGL-OS-E301-Position Mooring.
Goodman, J.E., 1899. Mechanics Applied to Engineering. Longman, Green & Company, London, 1899.
Hong, S.Y., Choi, Y.R., Hong, S.W., 2002. Analysis of hydro-elastic response of pontoon-type VLFS coupled with floating breakwaters using a higher-order boundary element method. In: International Ocean and Polar Engineering Conference. ISOPE-I-02-047.
Larsen, C.E., Irvine, T., 2015. A review of spectral methods for variable amplitude fatigue prediction and new results. Procedia Eng. 101, 243–250. https://doi.org/10.1016/j.proeng.2015.02.034.
Lutes, L.D., Sarkani, S., 1997. Stochastic Analysis of Structural and Mechanical Vibrations. No Title.
Martinelli, L., Ruol, P., Zanuttigh, B., 2008. Wave basin experiments on floating breakwaters with different layouts. Appl. Ocean Res. 30, 199–207. https://doi.org/10.1016/j.apor.2008.09.002.
Matsuichi, M., Endo, T., 1968. Fatigue of Metals Subjected to Varying Stress.
McCartney, B.L., 1985. Floating breakwater design. J. Waterw. Port, Coast. Ocean Eng. 111, 304–318.
Miner, M.A., 2021. Cumulative damage in fatigue. J. Appl. Mech. 12, A159–A164. https://doi.org/10.1115/1.4009458.
Mourão, A., Correia, J.A.F.O., Ávila, B.V., de Oliveira, C.C., Ferradosa, T., Carvalho, H., Castro, J.M., De Jesus, A.M.P., 2020. A fatigue damage evaluation using local damage parameters for an offshore structure. Proc. Inst. Civ. Eng. - Marit. Eng. 173, 43–57. https://doi.org/10.1680/jmaen.2019.24.
Muñiz-Calvente, M., Álvarez-Vazquez, A., Pelayo, F., Aenlle, M., García Fernández, N., 2022. A comparative review of time- and frequency-domain methods for fatigue damage assessment. Int. J. Fatig. 163, 107069 https://doi.org/10.1016/j.ijfatigue.2022.107069.
Newland, D.E., 2012. An Introduction to Random Vibrations, Spectral & Wavelet Analysis. Courier Corporation.
Palmgren, A.G., 1924. Die Lebensdauer von KugellagernZeitschrift des. Vereines Dtsch. Ingenieure 68, 339–341.
Peña, E., Ferreras, J., Sanchez-Tembleque, F., 2011. Experimental study on wave transmission coefficient, mooring lines and module connector forces with different designs of floating breakwaters. Ocean Eng. 38, 1150–1160. https://doi.org/10.1016/j.oceaneng.2011.05.005.
Pierson Jr., W.J., Moskowitz, L., 1964. A proposed spectral form for fully developed wind seas based on the similarity theory of SA Kitaigorodskii. J. Geophys. Res. 69, 5181–5190.

Rice, S.O., 1945. Mathematical analysis of random noise. Bell Syst. Tech. J. 24, 46–156. https://doi.org/10.1002/j.1538-7305.1945.tb00453.x.
Richey, E.P., 1982. Floating Bieakwater Field Experience. West Coast.
Samaei, S., Azarsina, F., Ghahferokhi, M., 2016. Numerical simulation of floating pontoon breakwater with ANSYS AQWA software and validation of the results with laboratory data. Bull. la Société R. des Sci. Liège 85, 1487–1499.
Shapiro, S.S., Wilk, M.B., 1965. An analysis of variance test for normality (complete samples). Biometrika 52, 591–611.
Slavič, J., Boltezar, M., Mrsnik, M., Cesnik, M., Javh, J., 2020. Vibration Fatigue by Spectral Methods: from Structural Dynamics to Fatigue Damage–Theory and Experiments. Elsevier.
Tovo, R., 2002. Cycle distribution and fatigue damage under broad-band random loading. Int. J. Fatig. 24, 1137–1147. https://doi.org/10.1016/S0142-1123(02)00032-4.
Vanmarcke, E.H., 1972. Properties of spectral moments with applications to random vibration. J. Eng. Mech. Div. 98, 425–446. https://doi.org/10.1061/JMCEA3.0001593.
Welch, P., 1967. The use of fast Fourier transform for the estimation of power spectra: a method based on time averaging over short, modified periodograms. IEEE Trans. Audio Electroacoust. 15, 70–73. https://doi.org/10.1109/TAU.1967.1161901.
Williams, A.N., Lee, H.S., Huang, Z., 2000. Floating pontoon breakwaters. Ocean Eng. 27, 221–240. https://doi.org/10.1016/S0029-8018(98)00056-0.
Wirsching, P.H., Light, M.C., 1980. Fatigue under wide band random stresses. J. Struct. Div. 106, 1593–1607. https://doi.org/10.1061/JSDEAG.0005477.
Xu, S., Rezanejad, K., Gadelho, J.F.M., Soares, C.G., 2022. Influence of the power take-off damping of a dual chamber floating oscillating water column on the mooring fatigue damage. Ocean Eng. 249, 110832 https://doi.org/10.1016/j.oceaneng.2022.110832.
Xu, S., Soares, C.G., 2021. Evaluation of spectral methods for long term fatigue damage analysis of synthetic fibre mooring ropes based on experimental data. Ocean Eng. 226, 108842 https://doi.org/10.1016/j.oceaneng.2021.108842.
Zhang, C., Dai, J., Keng, K., Vincent, H., 2024. Development of compliant modular floating photovoltaic farm for coastal conditions. Renew. Sustain. Energy Rev. 190, 114084 https://doi.org/10.1016/j.rser.2023.114084.
Zhao, X.L., Ning, D.Z., Zou, Q.P., Qiao, D.S., Cai, S.Q., 2019. Hybrid floating breakwater-WEC system: a review. Ocean Eng. 186, 106126 https://doi.org/10.1016/j.oceaneng.2019.106126.
Zorman, A., Slavič, J., Boltežar, M., 2023. Vibration fatigue by spectral methods — a review with open-source support. Mech. Syst. Signal Process. 190, 110149 https://doi.org/10.1016/j.ymssp.2023.110149.

5. Discusión General

La ingeniería costera enfrenta desafíos cada vez más complejos debido a la necesidad de desarrollar estructuras marinas seguras y eficientes que puedan resistir las fuerzas del oleaje y las duras y cambiantes condiciones ambientales. En este contexto, la presente tesis aborda el desarrollo de pautas para el diseño de las conexiones en diques flotantes modulares empleando herramientas de cálculo numéricas.

Los resultados de esta investigación se basan en un extenso análisis de simulaciones hidrodinámicas donde la estructura flotante se ha expuesto a múltiples estados de mar. El uso del método numérico BEM como herramienta de cálculo ha permitido obtener tiempos de simulación relativamente asumibles, manteniendo una buena precisión en la respuesta de la estructura y la estimación de las cargas inducidas por el oleaje en las conexiones. Otros trabajos como López et al. (2017) o G. Wang et al. (2020) también han aplicado este tipo de modelo hidrodinámico a estructuras flotantes similares satisfactoriamente. En este sentido, el uso de este tipo de modelos hidrodinámicos presenta una gran ventaja sobre otros métodos de cálculo, aunque no se consiga tanta precisión como los modelos CFD o SPH.

La estructura flotante modular ha sido simulada frente a condiciones de oleaje regular e irregular (ver capítulo 2. Modelización numérica en el dominio del tiempo de las fuerzas de conexión en un pontón modular flotante bajo oleaje oblicuo regular e irregular). Los oleajes regulares producen respuestas hidrodinámicas periódicas y, por consiguiente, cargas de amplitud constante sobre las conexiones del dique. Las simulaciones con este tipo de oleaje son óptimas para calibrar la respuesta de la estructura con ensayos físicos o experimentales, ya que permiten una correlación de los resultados más sencilla (Chen et al., 2017). Sin embargo, no reproducen el sistema de cargas reales a las que la estructura va a estar sometida. Por ello, se ha demostrado que el uso de oleajes irregulares en el diseño de las conexiones debe ser imperativo a la hora de analizar cualquier modo de fallo.

El parámetro que controla el comportamiento hidrodinámico de estas estructuras es la rigidez que aportan las conexiones al conjunto de pontones modulares como se observa en el capítulo 2. En otras palabras, la respuesta del dique flotante depende de la capacidad de la conexión para permitir el cabeceo relativo entre los pontones (Loukogeorgaki and Angelides, 2005). Una conexión demasiado rígida produce fuerzas axiales elevadas en las conexiones, mientras que una conexión demasiado flexible permite cabeceos relativos de gran amplitud. Una adecuada rigidez en la conexión puede obtenerse a través de la pretensión de los cables de acero trenzado, pero ha de tenerse en cuenta que la fuerza máxima inducida por el oleaje que puede soportar la conexión se reduce cuando aumenta la fuerza de pretensión. Análogamente, el daño por fatiga de la conexión también aumenta con la fuerza de pretensión (ver capítulo 4. Evaluación del riesgo de daños por fatiga en las conexiones de los pontones flotantes).

El otro parámetro estructural con más influencia sobre la fuerza axial obtenida en la conexión es su ubicación relativa en el dique. El dique flotante modular soporta la carga del oleaje de manera similar a una viga biapoyada frente a una carga distribuida. Los esfuerzos más altos aparecen en la zona central, donde se encuentran las conexiones intermedias, mientras que los más bajos aparecen en las conexiones extremas (Loukogeorgaki et al., 2014). Por tanto, la restricción al movimiento relativo entre módulos también es un factor a tener en cuenta en el análisis estructural. Se debe prestar especial atención no solo al diseño a corto y largo plazo de las conexiones intermedias, sino también a su mantenimiento.

La afección que tienen los parámetros del estado de mar sobre la estructura también han sido estudiados. A medida que aumenta la altura significante y el periodo pico, se encuentra que la fuerza axial que soporta la conexión también lo hace. Esto es especialmente notable en oleajes oblicuos, donde su combinación con alturas de ola significante moderadas y periodos de pico largos, produce fuerzas que llegan a sobrepasar la resistencia nominal de la conexión (ver capítulo 3. Análisis a corto plazo de las fuerzas inducidas por el oleaje en las conexiones de un dique flotante). Los valores máximos aparecen cuando el oleaje forma un ángulo de 60º-70º sobre la longitudinal de la estructura (Peña et al., 2011). La fuerza axial decrece a medida que el ángulo de incidencia decrece o crece, encontrándose valores mínimos cuando la dirección llega a ser completamente transversal. Por ello, el empleo de modelos tridimensionales se convierte en una necesidad. La duración del estado de mar es otro parámetro que tiene incidencia, sobre todo con el tiempo de cómputo. Se ha encontrado que las fuerzas inducidas por el oleaje en las conexiones llegan a ser un proceso estacionario con simulaciones de estados de mar de 30 minutos. Por ello, no se requieren duraciones largas del estado de mar para analizar los modos de fallo de la conexión. La consecuencia de esta estacionariedad puede estar influenciada por el ancho de banda de la señal de entrada al modelo numérico que, en este caso, se corresponden con el espectro de oleaje incidente.

Los parámetros del oleaje influyen de forma similar al daño por fatiga obtenido en la conexión. Los resultados muestran como el daño por fatiga crece con la altura significante de ola y el periodo de pico, pero esto solo es apreciable si el oleaje es oblicuo (ver capítulo 4). Asimismo, se ha podido comprobar que el análisis en el dominio de la frecuencia ofrece una precisa y eficiente alternativa para la estimación de daño, especialmente cuando se utilizan las funciones de transferencia de tensiones (Xu et al., 2020).

Las condiciones del emplazamiento juegan un papel crucial en el diseño y la estabilidad de las estructuras costeras. Factores como la morfología del lecho marino, la acción de las corrientes, la exposición a tormentas y la proximidad a la costa pueden influir significativamente en el comportamiento y la durabilidad de las instalaciones de protección costeras. Por lo tanto, es fundamental realizar un análisis detallado de las condiciones locales de emplazamiento de la estructura, para asegurar su adecuada planificación y diseño. Alternativamente, para garantizar una correcta funcionalidad también se recomienda estudiar las cargas en los fondeos. Aunque estos elementos no son tan críticos como las conexiones, también tienen bastante influencia en la respuesta de movimientos de la estructura. En especial, si la estructura es fondeada con catenarias de acero se debe verificar su capacidad resistente frente a cargas impulsivas como los tirones (Plaut et al., 2000).

La aplicación práctica de las contribuciones de esta investigación tiene impacto en la ingeniería costera moderna. Las pautas desarrolladas pueden ser utilizadas por especialistas técnicos en la planificación y construcción una estructura modular para diversas ubicaciones, costeras y *off-shore*. Al implementar las recomendaciones derivadas de esta tesis, se pueden diseñar y verificar conexiones más resistentes y duraderas, lo que resulta en una mayor seguridad y eficacia de las obras de abrigo sostenibles.

6. Conclusiones

La investigación afronta el diseño y verificación de los elementos de conexión de un pontón flotante modular mediante modelización numérica. El estudio llevado a cabo se presenta a través de tres publicaciones científicas. Estas presentan un enfoque numérico basado en la teoría del potencial, que emplea el método BEM para modelar la interacción oleaje-estructura en 3D y estimar las fuerzas inducidas por el oleaje en las conexiones entre los módulos flotantes.

La primera publicación aborda el proceso de modelización de la estructura y su calibración. En el artículo se destaca que el enfoque de modelización numérica en el dominio del tiempo permite estimar de forma precisa el comportamiento hidrodinámico de la estructura, incluidos los efectos no lineales que surgen de la interacción con el fluido. Esta metodología representa un avance significativo en la comprensión de la dinámica de las conexiones entre módulos, subrayando la importancia de la rigidez de las mismas como parámetro fundamental en su diseño. La investigación revela también la necesidad de considerar las condiciones de oleaje irregular en el diseño y la verificación de estos componentes, ya que estas condiciones pueden generar cargas hidrodinámicas significativas, que deben ser tenidas en cuenta para garantizar la seguridad del dique flotante.

El segundo artículo científico propone una metodología para definir las fuerzas extremas inducidas por el oleaje en las conexiones de la estructura durante estados de mar moderados de corta duración. Ésta publicación, representa un avance significativo en la comprensión de las cargas extremas que se generan en estos elementos singulares de conexión. Además, la investigación pone de relieve la importancia de considerar no solo las características del oleaje, como la altura significante, el periodo de pico o el ángulo de incidencia, sino también la ubicación de las conexiones en el dique flotante. Se concluye que las conexiones intermedias soportan fuerzas mucho mayores que las conexiones extremas, especialmente ante un oleaje con un ángulo de incidencia oblicuo. Esto, resalta la necesidad de un diseño detallado y una planificación cuidadosa de la disposición de los módulos flotantes, así como de las implicaciones para la seguridad en entornos marítimos adversos. Adicionalmente, la publicación ofrece una comparación detallada entre dos enfoques para la selección de picos de carga, su ajuste a siete distribuciones de probabilidad diferentes y la estimación de las fuerzas de diseño. Se evidencia que el análisis de los picos de carga obtenidos al aplicar el método POT (*Peak Over Threshold*), siguen una distribución probabilística de Pareto, que proporciona una representación más adecuada de las fuerzas extremas inducidas por el oleaje en las conexiones de los diques flotantes.

La tercera publicación se centra en la evaluación del daño por fatiga que sufren las conexiones del dique flotante, utilizando enfoques tanto en el dominio del tiempo como en el dominio de la frecuencia. Este estudio representa un avance significativo en la comprensión de los procesos de fatiga en estructuras modulares marítimas y costeras, ofreciendo nuevas perspectivas sobre la vida útil y la seguridad a largo plazo. En el artículo se investiga la aplicación de un enfoque en el dominio del tiempo, utilizando el algoritmo de conteo de ciclos de tensión Rainflow y el modelo de daño de Palmgren-Miner, para evaluar el daño por fatiga de manera precisa bajo diferentes condiciones de oleaje. Además, el estudio comparó varios métodos espectrales para la estimación del daño por fatiga, incluyendo los métodos de Dirlik, Tovo-Benasciutti y Wirsching-Light. Se concluye que, el método espectral de Wirsching-Light produce el mejor ajuste a los resultados obtenidos con el algoritmo Rainflow, con un error cercano al 1%. Se destaca también, la introducción de un enfoque basado en funciones de transferencia de tensiones, obtenidas mediante un espectro de oleaje

de ruido blanco. Este método ofrece una alternativa eficiente y precisa para la evaluación de la fatiga, en comparación con los métodos tradicionales. La aplicación de estas funciones de transferencia de tensión permite reducir significativamente el número de simulaciones necesarias, lo que se traduce en un importante ahorro computacional.

En conclusión, las contribuciones conseguidas en esta tesis doctoral contribuyen al avance del conocimiento del comportamiento hidrodinámico de las estructuras marinas modulares y ofrecen recomendaciones prácticas para optimizar los recursos computacionales en análisis hidrodinámicos estructurales. La investigación presentada ofrece una base sólida para el diseño y la verificación de los elementos de conexión en estructuras flotantes, contribuyendo al desarrollo sostenible de las zonas marítimas y costeras. Estos avances impulsan el conocimiento en ingeniería costera y *off-shore*, promoviendo soluciones innovadoras y sostenibles para desafíos futuros en la gestión del mar, la costa y la protección del litoral asociados.

7. LÍNEAS FUTURAS DE INVESTIGACIÓN

La tesis doctoral proporciona una base sólida para futuras investigaciones y práctica ingenieril. Uno de los caminos a explorar puede ser el desarrollo de técnicas de modelado más avanzadas y computacionalmente eficientes, que puedan simular con mayor precisión el comportamiento de las conexiones en condiciones extremas de oleaje sin requerir grandes tiempos de cómputo. Esto podría incluir la integración de modelos físicos y numéricos más complicados, así como la consideración de efectos adicionales como las corrientes marinas, el viento o la interacción entre las estructuras y un lecho marino más complejo.

Otro aspecto importante a considerar en investigaciones futuras es la optimización del diseño de las conexiones para minimizar el daño por fatiga sin comprometer su resistencia estructural. Esto implicaría un estudio exhaustivo sobre el impacto de la pretensión en los cables de acero trenzado en la rigidez del conjunto, la resistencia de la conexión frente a cargas extremas y el daño a fatiga. Para ello se recomienda diseñar un ensayo de laboratorio que reproduzca el sistema de fuerzas sobre la conexión. También se deberían explorar materiales innovadores o técnicas de fabricación avanzadas que mejoren la durabilidad y la vida útil de las conexiones en entornos marinos agresivos.

Se recomienda investigar líneas futuras relacionadas con el diseño de la estructura para las condiciones medioambientales específicas del lugar en el que se emplace, así como realizar estudios numéricos y experimentales más complejos y tener en cuenta la afección del cambio climático sobre las condiciones del oleaje y del nivel del mar. Particularmente, se sugiere instrumentalizar estructuras de este tipo para obtener datos reales de su comportamiento. Además, se propone explorar la interacción dinámica entre los diques flotantes y otros elementos costeros, como la influencia en la sedimentación y la protección de ecosistemas.

Dado el impacto del cambio climático en los patrones de oleaje y la frecuencia de eventos climáticos extremos, también será necesario investigar cómo estas tendencias pueden afectar la estabilidad y el rendimiento de las estructuras flotantes en el futuro. Esto podría implicar la evaluación de escenarios de cambio climático y la adaptación de las metodologías de diseño para garantizar la resiliencia de las instalaciones costeras frente a condiciones ambientales cada vez más desafiantes. En resumen, la investigación presentada en esta tesis no solo tiene implicaciones inmediatas en términos de diseño y construcción de diques flotantes modulares, sino que también abre nuevas oportunidades para la innovación y el avance en el campo de la ingeniería costera, contribuyendo así a la protección y preservación de las zonas costeras en todo el mundo.

8. REFERENCIAS

Agarwal, P., Walker, W., Bhalla, K., 2015. Estimation of Most Probable Maximum From Short-Duration or Undersampled Time-Series Data, in: International Conference on Offshore Mechanics and Arctic Engineering. p. V003T02A052. https://doi.org/10.1115/OMAE2015-41701

Aliabadi, M.H., Wen, P.H., 1984. Boundary element methods in engineering science, International Journal of Rock Mechanics and Mining Sciences & Geomechanics Abstracts. https://doi.org/10.1016/0148-9062(84)90010-x

ANSYS, 2016. ANSYS Aqwa. ANSYS Ltd., Canonsburg, PA, USA.

Candle, R.D., 1974. Goodyear scrap tire floating breakwater concepts.

Cebada-Relea, A.J., Aenlle, M., López, M., 2024. Fatigue damage risk assessment on connections of floating pontoon arrays. Ocean Eng. 299. https://doi.org/10.1016/j.oceaneng.2024.117317

Cebada-Relea, A.J., López, M., Aenlle, M., 2022. Time-domain numerical modelling of the connector forces in a modular pontoon floating breakwater under regular and irregular oblique waves. Ocean Eng. 243, 110263. https://doi.org/10.1016/j.oceaneng.2021.110263

Cebada-Relea, A.J., López, M., Claus, R., Aenlle, M., 2023. Short-term analysis of extreme wave-induced forces on the connections of a floating breakwater. Ocean Eng. 280. https://doi.org/10.1016/j.oceaneng.2023.114579

Chakrabarti, S.K., 1994. Hydrodynamics of Offshore Structures. Comput. Mech. Publ.

Chen, X., Miao, Y., Tang, X., Liu, J., 2017. Numerical and experimental analysis of a moored pontoon under regular wave in water of finite depth. Ships Offshore Struct. 12, 412–423. https://doi.org/10.1080/17445302.2016.1172831

Claus, R., Clemente, D., Soto, F., Cebada, A., Mario, L., Giannini, G., Rosa-santos, P., 2024. Experimental proof-of-concept of HelioSea : A novel marine floating photovoltaic device 299. https://doi.org/10.1016/j.oceaneng.2024.117184

Dai, J., Wang, C.M., Utsunomiya, T., Duan, W., 2018. Review of recent research and developments on floating breakwaters. Ocean Eng. 158, 132–151. https://doi.org/10.1016/j.oceaneng.2018.03.083

DNV GL, 2017. DNVGL-RP-C205: Environmental Conditions and Environmental Loads. DNV GL Recomm. Pract. 1–259.

DNVGL-OS-E301, 2018. Offshore standards - Position mooring 144.

Dong, G.H., Zheng, Y.N., Li, Y.C., Teng, B., Guan, C.T., Lin, D.F., 2008. Experiments on wave transmission coefficients of floating breakwaters. Ocean Eng. 35, 931–938. https://doi.org/https://doi.org/10.1016/j.oceaneng.2008.01.010

Elchahal, G., Younes, R., Lafon, P., 2009. Parametrical and Motion Analysis of a Moored Rectangular Floating Breakwater. J. Offshore Mech. Arct. Eng. 131, 31303. https://doi.org/10.1115/1.3124125

Ferreras, J., Peña, E., López, A., López, F., 2014. Structural Performance of a Floating Breakwater for Different Mooring Line Typologies. J. Waterw. Port, Coastal, Ocean Eng. 140, 1–11. https://doi.org/10.1061/(asce)ww.1943-5460.0000240

Fousert, M.W., 2007. Floating Breakwater. Theoretical study of a dynamic wave attenuating system. Technische Universiteit Delft.

Goda Y., 2000. Random Seas and Design in Maritime Structures, 2nd ed. Singapore.

Hales, L.Z., 1981. Floating Breakwaters: State-of-the-Art Literature Review. U.S.Army, Corps Eng. Coast. Eng. Res. Cent.

Hamburg Port Authority, n.d. Port of Hamburg [WWW Document]. URL https://www.hamburg-port-authority.de/en/hpa-360 (accessed 2.13.24).

REFERENCIAS

Hann-Ocean, n.d. RPC rigid connector [WWW Document]. URL http://www.hann-cean.com/index.php/products/rigifloat.html (accessed 2.26.24).

Ji, C., Yang, K., Cheng, Y., Yuan, Z., 2018. Numerical and Experimental Investigation of Interactions Between Free-Surface Waves and A Floating Breakwater with Cylindrical-Dual/Rectangular-Single Pontoon. China Ocean Eng. 32, 388–399. https://doi.org/10.1007/s13344-018-0041-x

Larsen, C.E., Irvine, T., 2015. A review of spectral methods for variable amplitude fatigue prediction and new results. Procedia Eng. 101, 243–250. https://doi.org/10.1016/j.proeng.2015.02.034

Liu, Z., Wang, Y., 2020. Numerical investigations and optimizations of typical submerged box-type floating breakwaters using SPH. Ocean Eng. 209, 107475. https://doi.org/https://doi.org/10.1016/j.oceaneng.2020.107475

López, M., Claus, R., Soto, F., Hernández-Garrastacho, Z.A., Cebada-Relea, A., Simancas, O., 2024. Advancing offshore solar energy generation: The HelioSea concept. Appl. Energy 359. https://doi.org/10.1016/j.apenergy.2024.122710

López, M., Taveira-Pinto, F., Rosa-Santos, P., 2017. Numerical modelling of the CECO wave energy converter. Renew. Energy 113, 202–210. https://doi.org/10.1016/j.renene.2017.05.066

Loukogeorgaki, E., Angelides, D.C., 2005. Stiffness of mooring lines and performance of floating breakwater in three dimensions. Appl. Ocean Res. 27, 187–208. https://doi.org/10.1016/j.apor.2005.12.002

Loukogeorgaki, E., Yagci, O., Sedat Kabdasli, M., 2014. 3D Experimental investigation of the structural response and the effectiveness of a moored floating breakwater with flexibly connected modules. Coast. Eng. 91, 164–180. https://doi.org/10.1016/j.coastaleng.2014.05.008

Matsuichi, M., Endo, T., 1968. Fatigue of metals subjected to varying stress.

McCartney, B.L., 1985. Floating breakwater design. J. Waterw. Port, Coast. Ocean Eng. 111, 304–318.

Miner, M.A., 2021. Cumulative Damage in Fatigue. J. Appl. Mech. 12, A159–A164. https://doi.org/10.1115/1.4009458

Morison, J.R., Johnson, J.W., Schaaf, S.A., 1950. The Force Exerted by Surface Waves on Piles. J. Pet. Technol. 2, 149–154. https://doi.org/10.2118/950149-g

Mourão, A., Correia, J.A.F.O., Ávila, B.V., de Oliveira, C.C., Ferradosa, T., Carvalho, H., Castro, J.M., De Jesus, A.M.P., 2020. A fatigue damage evaluation using local damage parameters for an offshore structure. Proc. Inst. Civ. Eng. - Marit. Eng. 173, 43–57. https://doi.org/10.1680/jmaen.2019.24

Muñiz-Calvente, M., Álvarez-Vazquez, A., Pelayo, F., Aenlle, M., García Fernández, N., 2022. A comparative review of time- and frequency-domain methods for fatigue damage assessment. Int. J. Fatigue 163, 107069. https://doi.org/10.1016/j.ijfatigue.2022.107069

Na'im, I.I., Shahrizal, A.R.M., Safari, M.D., 2018. A Short Review of Submerged Breakwaters. MATEC Web Conf. 203, 1–17. https://doi.org/10.1051/matecconf/201820301005

North Adriatic Sea Port Authority, n.d. Port of Venice (1917) [WWW Document]. URL https://www.port.venice.it/en/port-offer/the-ports/port-of-venice (accessed 2.13.24).

Ofuya, A.O., 1968. On Floating Breakwaters. Research Report No. CE-60.

OTLE, 2023. Observatorio del Transporte y la Logística en España. Informe anual 2022. Madrid.

Palmgren, A.G., 1924. Die Lebensdauer von KugellagernZeitschrift des. Vereines Dtsch. Ingenieure 68, 339–341.

Peña, E., López, A.T., Ferreras, J., Sánchez-Tembleque, F., López, F., Sopelana, J., 2011. Strain gauges measurements of mooring lines and module connector forces in a physical model of the Aguete port floating breakwater. Ocean. 2011 IEEE - Spain. https://doi.org/10.1109/Oceans-Spain.2011.6003506

Plaut, R.H., Archilla, J.C., Mays, T.W., 2000. Snap loads in mooring lines during large three-dimensional motions of a cylinder. Nonlinear Dyn. 23, 271–284. https://doi.org/10.1023/A:1008368427878

Port of Amsterdam, n.d. Port of Amsterdam [WWW Document]. URL https://www.portofamsterdam.com/en/about-port-amsterdam (accessed 2.23.24).

Puertos del Estado, 2009. ROM 1.0-09: Recommendations for the design and execution of protection structures.

Richey, E.P., others, 1982. Floating breakwater field experience, West Coast. The Center.

SF-Marina, n.d. Flexible connector [WWW Document]. URL https://sfmarina.com/solutions/technique/#_connector (accessed 2.26.24).

Stitt, R.L., Nobel, H.M., 1963. Introducing Wave-Maze Floating Breakwater. unnumbered report, Temple City, Calif.

Takahashi, S., 2002. Design of Vertical Breakwaters 1996.

Tsinker, G.P., 1995. Marine Structures Engineering. Specialized applications. https://doi.org/10.1007/978-1-4615-2081-8

Wang, C.M., Han, M.M., Lyu, J., Duan, W.H., Jung, K.H., Kang An, S., 2020. Floating Forest: A Novel Concept of Floating Breakwater-Windbreak Structure, Lecture Notes in Civil Engineering. Springer Singapore. https://doi.org/10.1007/978-981-13-8743-2_12

Wang, C.M., Nguyen, H.P., 2023. Floating Breakwaters: Sustainable Solution for Creating Sheltered Sea Space. Lect. Notes Civ. Eng. 268, 3–20. https://doi.org/10.1007/978-981-19-3303-5_1

Wang, C.M., Wang, B.T. (Eds.), 2015. Large Floating Structures. Technological advances., 1st ed. Springer Singapore. https://doi.org/https://doi.org/10.1007/978-981-287-137-4

Wang, G., Drimer, N., Goldfeld, Y., 2020. Modular floating structures (MFS) for offshore dwelling a hydrodynamic analysis in the frequency domain. Ocean Eng. 216, 107996. https://doi.org/10.1016/j.oceaneng.2020.107996

Wang, G., Goldfeld, Y., Drimer, N., 2019. Expanding coastal cities – Proof of feasibility for modular floating structures (MFS). J. Clean. Prod. 222, 520–538. https://doi.org/10.1016/j.jclepro.2019.03.007

Williams, A.N., Abul-Azm, A.G., 1997. Dual pontoon floating breakwater. Ocean Eng. 24, 465–478. https://doi.org/https://doi.org/10.1016/S0029-8018(96)00024-8

Williams, A.N., Lee, H.S., Huang, Z., 2000. Floating pontoon breakwaters. Ocean Eng. 27, 221–240. https://doi.org/10.1016/S0029-8018(98)00056-0

Wöhler, A., 1870. Über die festigkeitsversuche mit eisen und stahl. Ernst & Korn.

Xu, S., Soares, C.G., 2021. Evaluation of spectral methods for long term fatigue damage analysis of synthetic fibre mooring ropes based on experimental data. Ocean Eng. 226, 108842. https://doi.org/10.1016/j.oceaneng.2021.108842

Xu, S., Wang, S., Guedes Soares, C., 2020. Experimental investigation on hybrid mooring systems for wave energy converters. Renew. Energy 158, 130–153. https://doi.org/10.1016/j.renene.2020.05.070

Zhang, C., Ning, D., 2019a. Hydrodynamic study of a novel breakwater with parabolic openings for wave energy harvest. Ocean Eng. 182, 540–551. https://doi.org/10.1016/j.oceaneng.2019.04.056

Zhang, C., Ning, D., 2019b. Hydrodynamic study of a novel breakwater with parabolic openings for wave energy harvest. Ocean Eng. 182, 540–551. https://doi.org/10.1016/j.oceaneng.2019.04.056

Zhang, H., Xu, D., Xia, S., Shi, Q., Yang, G., Ding, R., 2020. Dynamics of Super-Scale Modularized Floating Airport, Lecture Notes in Civil Engineering. Springer Singapore. https://doi.org/10.1007/978-981-13-8743-2_6

Zhao, X.L., Ning, D.Z., Zou, Q.P., Qiao, D.S., Cai, S.Q., 2019. Hybrid floating breakwater-WEC system: A review. Ocean Eng. 186, 106126. https://doi.org/10.1016/j.oceaneng.2019.106126

Zorman, A., Slavič, J., Boltežar, M., 2023. Vibration fatigue by spectral methods — A review with open-source support. Mech. Syst. Signal Process. 190, 110149. https://doi.org/10.1016/j.ymssp.2023.110149

9. Anexo. Publicaciones complementarias

De manera complementaria a las publicaciones presentadas, aquí se recopilan estudios complementarios relacionados con la temática y desarrollados durante el periodo de esta tesis doctoral. Estos trabajos han sido expuestos presencialmente en los respectivos seminarios o congresos y publicados en sus libros de resúmenes o *proceedings*.

El estudio titulado *Dynamic analysis of floating breakwaters: a case study* fue presentado en el 2º Congreso de la Dinámica Estructural (DINEST 2021) en la ciudad de Gijón (Principado de Asturias, España). El trabajo muestra el proceso de modelización hidrodinámica del módulo de pontón flotante utilizado en el puerto de Figueras (Figura 5). En él se detallan los resultados del análisis armónico del módulo, así como las ventajas y limitaciones encontradas durante el proceso de modelización.
Referencia: Cebada-Relea, A.J., López, M., Aenlle, M., Claus, R., 2021. Dynamic analysis of floating breakwaters: a case study. Proceedings of DINEST 2021, 134–145. ISBN: 978-84-09-30799-9.

Otro trabajo similar fue presentado en las 3as Jornadas de Investigación, Desarrollo e Innovación desarrolladas en la Escuela Politécnica de Mieres. El trabajo se titula "Evaluación dinámica para el posible uso de fondeos elástico-lineales en el dique flotante de Figueras (Asturias, España)". En él se analiza la respuesta de la estructura de abrigo completa instalada en el puerto de Figueras. Particularmente, se simulan las fuerzas en las conexiones y los movimientos relativos de los módulos utilizando dos tipos diferentes de fondeo, fondeo mediante catenarias y fondeo mediante cabos elásticos.
Referencia: Cebada-Relea, A.J., López Gallego, M., 2020. Evaluación dinámica para el posible uso de fondeos elástico-lineales en el dique flotante de Figueras (Asturias, España). 3as Jornadas Investigación Desarrollo e Innovación en Ing. Civil. Libro de Resúmenes, 68–71. ISBN: 978-84-18482-12-0.

Además, se estudió de forma exhaustiva la respuesta del pontón de Figueras aplicando las condiciones locales de oleaje sobre el modelo hidrodinámico. Se estimaron las fuerzas en las conexiones mediante modelización numérica y se realizó un ensayo de laboratorio sobre los cables de acero trenzado que componen la conexión inter-modular. Los resultados de este trabajo fueron publicados y presentados en el 39th IAHR *World Congress* celebrado en Granada (Andalucía, España), con el título de *Numerical Investigation of Floating Breakwaters Using Time Domain Boundary Element Method*.
Referencia: Cebada-Relea, A.J., Lopez, M., Claus, R., Soto, F., 2022. Numerical Investigation of Floating Breakwaters Using Time Domain Boundary Element Method. Proceedings of IAHR World Congress. 4383–4393. https://doi.org/10.3850/IAHR-39WC2521716X2022379.

En el *5th Iberian Conference on Structural Integrity* (IBCSI) celebrado en Coimbra se presentó y publicó el trabajo titulado "Diques flotantes portuarios: análisis de las conexiones y sinergias con la energía undimotriz". En este trabajo se propone, modela y estudia una disposición geométrica en planta parabólica para un pontón flotante modular. Se analiza el posible aprovechamiento energético al crear un foco de reflexión con la disposición parabólica, a la vez que se estudia si las fuerzas inducidas por el oleaje en las conexiones aumentan o disminuyen con esta disposición.

ANEXO

Referencia: Cebada-Relea, A., Menéndez, C., Fernández, P., Soto-Pérez, F., Claus, R., Aenlle, M., López, M., 2022. Diques flotantes portuarios: análisis de las conexiones y sinergias con la energía undimotriz. Revista Española de Mecánica de la Fractura 3, 199–204. ISSN: 2792-4246.

El último trabajo derivado de esta tesis fue presentado y publicado en el congreso del Grupo Español de la Fractura (GEF 2023) llevado a cabo en Gijón (Asturias, España). Éste lleva el título de "Análisis a fatiga de las conexiones de un dique flotante mediante simulación numérica" y realiza un análisis del daño por fatiga en las conexiones del dique flotante de forma simplificada. Se aplica el método de conteo de ciclos *Rainflow* y se estima el daño y la vida por fatiga de la conexión utilizando la regla de Palmgren-Miner.
Referencia: Cebada, A.J., Aenlle, M., López, M., 2023. Análisis a fatiga de las conexiones de un dique flotante mediante simulación numérica. Revista Española de Mecánica la Fractura. 5, 205–211. ISSN: 2792-4246.